The Synthesis and Structural Characterisation of a Series of Iodides and Dipyridyl Ketone based Metal Complexes with relevance to the Grätzel Photovoltaic cell and Single Molecule Magnets.

2014

Farhad Haghjoo

SCHOOL OF CHEMISTRY

UNIVERSTY OF MANCHESTER

To My Parents

Content

Declaration

No portion of the work referred to in the thesis has been submitted in support of an application for another degree or qualification of this or any other university or other institute of learning.

Signed:

Farhad Haghjoo

Copyright Statement

Acknowledgements

First of all, my heartfelt thanks go to my excellent supervisor, and friend, Dr. Robin Pritchard, whose continued help, support and encouragement, (not to mention patience!) have made it possible for me to survive the last, very difficult four years and complete this thesis.

My thanks also to my good friend Dr. Nick Barnes, whose help has been invaluable with certain aspects of synthesis, and with the supply of materials necessary to carry out some of the experiments.

Also I would like to thank Dr. Floriana Tuna of the Physics Department, for carrying out some essential magnetic property measurements of my new compound, and for presenting the compound at a conference in Dublin.

And last, but not least, my dear sister and brother, Nadia and Arash, and my friend Liz for her proofreading and many cups of tea!

Abstract

The Grätzel photovoltaic cell is described in the introductory chapter and the main experimental method used in this study, X-ray crystallography, in the second chapter.

The work described in chapter 3 and 4 was inspired by the Grätzel cell namely, the synthesis and characterisation of iodide and poly-iodides in chapter 3 and transition metal complexes synthesised using 2,2′-dipyridyl ketone in chapter 4.

Chapter five looks in detail at a series of tri-angular lanthanide complexes, a chance discovery made while synthesising the 2,2′-dipyridyl ketone complexes described in chapter 4. These tri-angular clusters have interesting magnetic properties that are also described.

1- Grätzel Cell

1-1. Introduction

The greatest effort in the new era is to find methods to replace and slowly eliminate fossil fuel energy resources. Burning fossil fuels leads to an enhanced greenhouse effect which leads to global warming, and as a consequence will affect other aspects of the earth's climate. In 1985 Grätzel opened a new door to using light energy to generate electricity by constructing a cell that enabled a photoelectron to be transferred from a ruthenium complex (dye) around an electric circuit via a series of interlinked steps, before returning to the dye having completed its work. On leaving the ruthenium complex, the electron is injected into TiO_2 as a semiconductor and conducted through a SnO_2 layer before returning through a graphite layer and I^-/I_3^- electrolyte back to the dye (Grätzel 2009) . Although this technology is not as efficient as a more conventional silicon photo cell it does not require a sophisticated factory for its construction; a big advantage in a developing country.

The disadvantage of the photovoltaic cell is that it uses an electrolyte, which has stability problems at low and high temperature. If the electrolyte freezes at low temperature, that

ends the function of production of power which potentially leads to physical damage. High temperatures cause the liquid to expand and the cell to crack. It is hoped that the intense research being carried out at present will lead to the elimination of these problems.

1-2. Photovoltaic cell

To understand the chemistry of light harvesting in relation to organic photovoltaic cells (OPVs), this is the subject of major intensive research; also the Grätzel cell or dye sensitized solar cells (DSCs) are now an integral member of the large group of OPVs.

Molecules are employed to absorb photons and convert them to electric charge directly by OPVs. The sensitizer, semiconductor and electrolyte are interfaced between two electrodes, which are individually playing an important role in OPVs. In the sensitizer, electrons are excited via photons from the ground state to the highest energy level. The sensitizer is attached to a large band gap semiconductor from which the electron is injected into the conducting band. The donation of electrons by an electrolyte regenerates the sensitizer. The electrolyte contains the most frequently used couple as a reduction and oxidation (redox) shuttle.

Figure 1-2-1 shows a typical diagram energy band for the DSCs. When electrons(***S′***) in the dye sensitizer are excited by the sunlight, the excited electrons (***S****) need a reduction conducted band to be injected into metal oxide TiO_2. As the dye sensitizer passed their electrons the dye cation is generated. The electron (***S***$^+$) returns by donation of the electrolyte and the dye is restored. The electrolyte consists of iodide/tri-iodide redox couple, $dye^+ + I^- \text{—} dye + I_3^-$. The tri-iodide is restored to iodide by taking the electron from the electrode $I_3^- + electron \text{—} I^-$. The electrolyte is dissolved in organic solvent. This is the simplest description for the energy diagram. Furthermore there is a need to consider the properties and situations of the compounds involved Jun-Ho et al (2011).

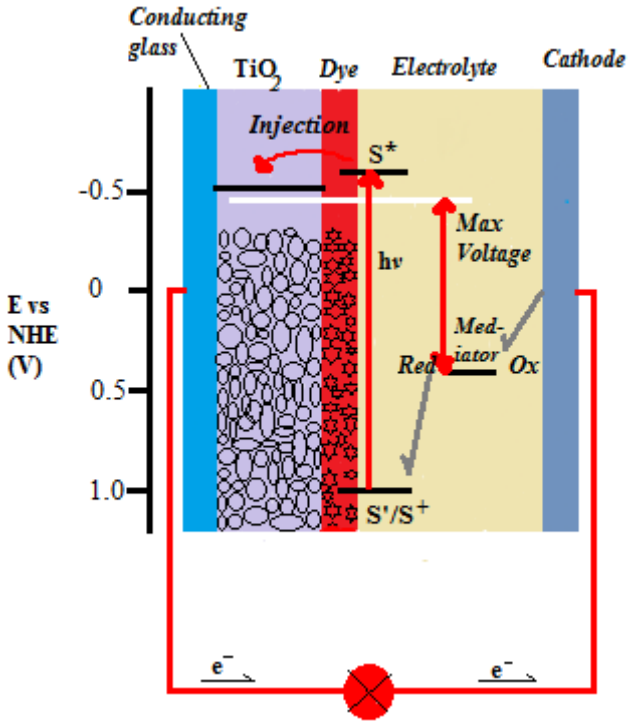

Figure 1-2-1. The energy bond diagram shows the DSC, which is using electrolyte, dye as a sensitizer and TiO_2 semiconductor. Electron **s'** excited by sunlight form **s*** and through TiO_2 moves to the conducting layer and finally after using energy returns to first position by electrolyte

1-2-1. Dye sensitizer in DSCs

In nature the processes of photosynthesis via chlorophyll (pigment), use sunlight energy to convert CO_2 and water to sugar. From this concept the dye sensitizer is formed to convert the light to electric charge. The dye sensitizer in the DSCs, within certain chemical properties, acts as chlorophyll in plants. The dye sensitizer must be a dark coloured compound to absorb all the wave lengths of visible electromagnetic spectrum energy to excite the electrons at the highest energy level *(electrons in the system can absorb the photon of light, on the right wavelength*). To synthesise a dye compound, therefore the conjugated systems

double bonds vitalize to give a strong colour. With more conjugated double bonds in the system, the absorption is in the longer wavelength and the colour of the compounds, form yellow to red. Another choice can be transition metals to provide colour in the compound. The colour of transition metal compounds is related to the electronic transition, ligand-to-metal, metal-to-ligand charge transfer and *d-d* transitions. Also a dye sensitizer should be able to bond to semiconductors as well as having higher energy levels so that the excited electrons can effortlessly be injected to the semiconductor.

The ground and excited states of electrons in dye is important. The ground state is a place to regenerate the dye sensitizer when the electrons are injected to the semiconductor from an excited state. The excited state is a place for electrons to jump to the semiconductor; if the state is lower or equal to the semiconductor band energy gap then the electron can't jump. (*Figure 1-2-1)*

Many different dye sensitizers have been synthesised and the numbers are growing. One of the base structures which is used a lot in DSCs is N719 by Nazeeruddin et al (1993), which is an example of dye sensitizer shown in *Figure 1-2-2.* The question marks are places where different functional groups can be placed such as -NCS, -COOH etc. Using a variety of substances can change the properties of the compound dramatically which aims

to synthesise a compound suitable as a dye sensitizer in DSCs to obtain more electrical current.

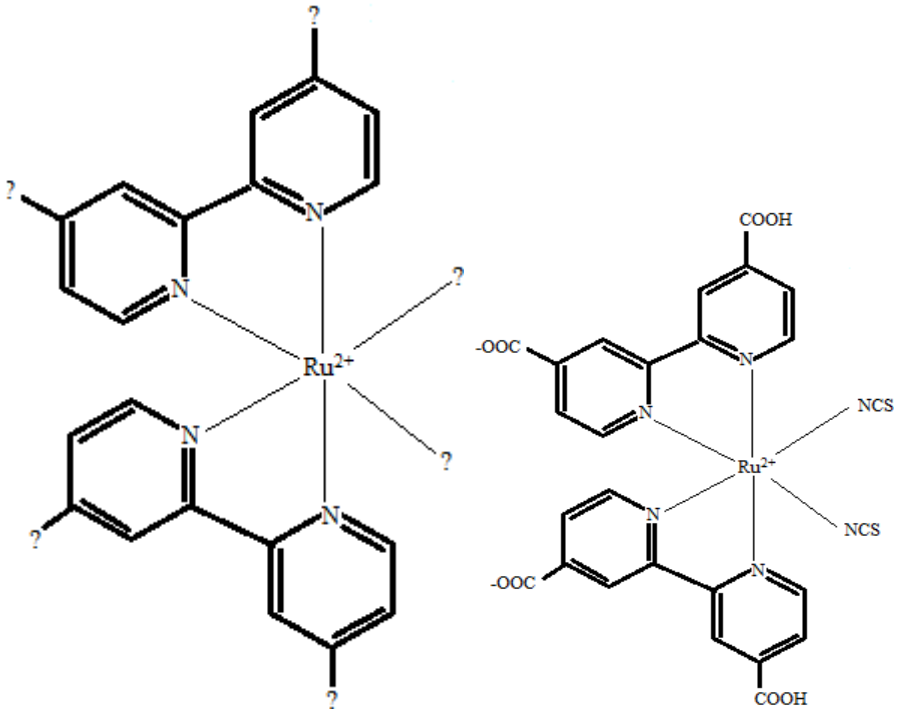

Figure 1-2-2. On the left, a base structure to make different dye sensitizers, ?-bis(2,2′-bipyridyl-4,4′-? ruthenium(II). On the right N719 dye sensitizer (question marks can be different substituents)

Also many organic dye sensitizers have been applied and the numbers of syntheses are growing. One of the base structures is shown in *Figure 1-2-3*. The question marks can be different functional groups, which change their properties and functions.

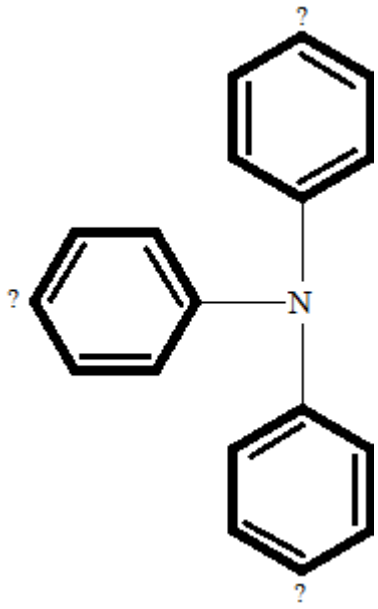

Figure 1-2-3. The ?-Tri phenyl amine is a base for many varieties of dye sensitizer (the question marks (?) can be different substances)

1-2-2. Semiconductor

A semiconductor has intermediate electrical conductivity in value between conductors and insulator. In the periodic table the Group IV pure elements are semiconductors. Semiconductor materials can change their behaviour by manipulating impurities, known as doping e.g. in crystalline silicon, adding an impurity of boron or phosphorus to make solar cells. A pure semiconductor is called an intrinsic semiconductor.

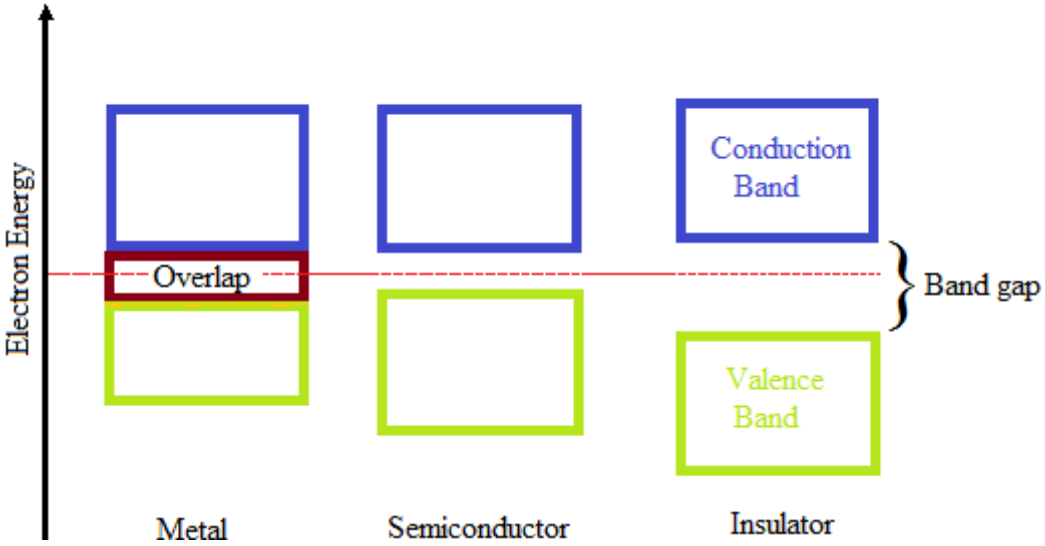

Figure 1-2-4. The diagram illustrates the energy level for the valence band and conduction band for metals which is overlapping, semiconductors with short band gap, and insulators with larger band gap

The electrons can exist in certain energy band levels. *Figure 1-2-4* shows the energy band levels for metal (**M**), semiconductor (**S**) and insulator (**I**). The ground state, where the electrons are close bonded to the atomic nuclei of the material or valence band, is the same situation for **M**, **S** and **I**. But **M**s are distinguishable from **S** and **I** by the population of the electrons in each band. The valence and conducting bands in the **M**s are filled by the electrons in normal conditions; as for **S** the conducting band has a few electrons above the valence band and in **I** there are no free electrons in the conducting band. The band gap for **I** is very high, however for **S** this band is smaller; excited electrons from the valence band can easily jump up to the conduction band. These electrons in the conduction band leave behind electron holes, in

other words unoccupied states in the valence band. The electrons in the conduction band and the electron holes in the valence band both contribute to the electrical conductivity. The holes are filled up by neighbouring electrons which leave new holes behind them. In this way it appears the holes are moving. The holes act as if they are positive charge particles.

In the semiconductor, the conduction band is a higher energy band than the valence band and the electrons travel through this band. The energy of the electrons is increased, by increasing temperature or applying an electric field to them. When the valence band is filled by electrons, it cannot carry electric current, because it requires more electron energy.

As doping is important in semiconductor properties and makes a pure semiconductor more useful, in particular in constructing electronic devices, some details are added. By adding a number of impurity atoms or different types of impurity atoms to the pure semiconductors, the electrical conductivity may vary. The semiconductor and dopant are suitable depending on the atomic properties. Dopants are controlling the product and are classified as electron acceptors or donors. The donor atoms function by creating excess negative charge carriers, with weakly bound valence electrons. The bound valence electrons can move relatively freely in the crystal lattice and facilitate conduction in

the presence of an electric field. Acceptor atoms function conversely and produce a hole. Semiconductors with donor impurity are called n-type, and with acceptor impurity are called p-type.

Increasing the doping concentration increases the conductivity due to the existence of a higher concentration of carriers for conduction.

1-3. References

Grätzel. M., (2009), *Accounts of chemical research*, **42**, No. 11, 1788-1798.

Nazeeruddin. M. K., Kay A., Rodicio. I., Humphry-Baker. R., Müller. E., Liska. P., Vlachopoulos. N., and Grätzel. M., (1993), *J. Am. Chem. Soc.*, **115**, (14), 6382

Jun-Ho Yum ***,** Etienne Baranoff **,** Sophie Wenger **,** Md. K.Nazeeruddin and Michael Grätzel (2011), *Energy Environ. Sci.*, **4**, 842-857

2- Characterisations

2-1. Introduction

In chemistry it is always a big challenge to identify and understand the physical and chemical properties of new structures, molecules or non-molecular materials. Spectroscopy is one of the most widely used methods for probing compounds and is based on the absorption or emission of radiation.

Another structure characterisation method used by chemist is X-ray crystallography, which does not rely on absorption of electromagnetic radiation but instead uses its wave properties to construct a diffraction pattern from the crystalline sample. With this method more detailed structural information is provided than by spectroscopic techniques.

X-ray crystallography started in 1912 when Laue recorded the first diffraction photograph of a crystal only a few years after the discovery of X-rays by Röntgen in 1894. From that time until now many changes have taken place to make the determination of crystal structures easier and quicker. X-ray crystallography has important roles in chemistry, biochemistry and geology where determination of crystal structures is vital.

To perform the technique many sophisticated mathematical calculations are necessary, however, it is not necessary to master the details of the calculations in order to understand the principles and application of the subject; almost all the calculations are usually performed by computers.

Crystallography provides the most direct way of forming images of crystals and molecules. These give detailed information that can be related to their activity, reaction mechanisms and the conformational changes which they may undergo for recognizing binding sites for substrates.

For the remainder of this Chapter the methods of crystal structure determination using X-ray diffraction will be examined in detail. Areas covered will include X-ray generation, X-ray measurement, X-ray crystallographic theory and practical aspects of crystallography including an outline of the approach used in this work.

2-2. X-rays

2-2-1. X-rays and Generation of X-rays

X-rays are electromagnetic waves like radio and light waves. X-rays have a wavelength in the range 0.01 to 10 nm, and frequencies range from 3 x 10^{16} to 3 x 10^{19} Hz *(Figure 2-2-1)*.

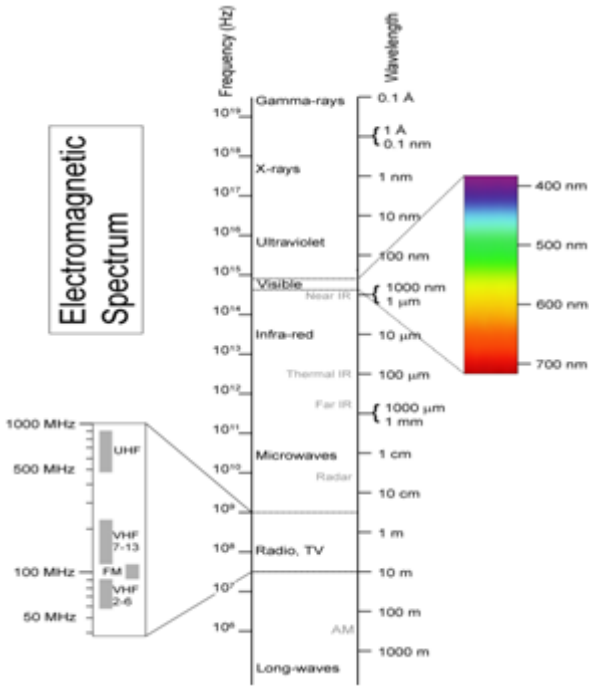

Figure 2-2-1. Illustration of the Electromagnetic Spectrum which is shows the frequencies and wavelengths for different radiations. http: Wikipedia.org/electromagnetic spectrum (14.12.2011)

Electromagnetic waves exist in packets known as photons. It may be helpful to think of a photon as a little bunch of waves, travelling at the velocity of light.

The energy carried in one photon is related to its wavelength by Planck's formula,

$$E = h\upsilon$$

where E= energy of the photon, υ= vibration frequency of the wave and *h*=Planck's constant.

Photons in the 0.5 Å to 2.0 Å range have energies from 25000 to 6000eV: equivalent to that of an electron which has been accelerated through several thousand volts and are described as X-rays. These energies are more than sufficient to ionize atoms, and for this reason X-rays are classified as 'ionizing radiation.

In order to create an intense X-ray source, an electron beam from a heated wire at a potential of 30kV or so is focused on a very small area of metal, which acts as a cathode, on to a metal anode. The cathode's potential is tens of kilovolts below that of the metal anode so that each electron possesses enough energy to produce an X-ray photon. A large amount of heat is generated in a small volume of the anode, which has to be conducted away efficiently and is a limiting factor when attempting to produce high intensity X-ray beams *(Figure 2-2-2)*.

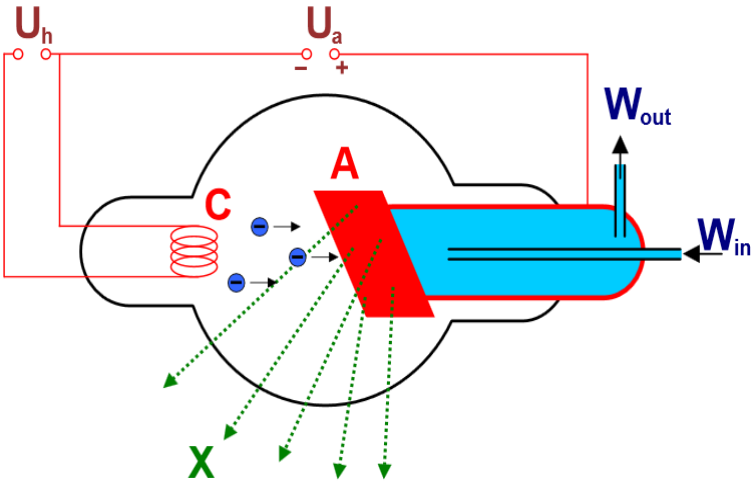

Figure 2-2-2. Illustration of a simple X-ray generator tube with the cooling systems. Where C: wire/cathode (-) and A: anode (+), also W_{in} and W_{out}: water inlet and outlet of cooling system. http: Wikipedia.org/X-ray_tube (14.12.2011)

The electrons cause transitions in the metal atoms of the anode, which release photons of particular energies known as 'characteristic' radiation as well as a general spectrum of white radiation. In practice, laboratory X-ray generators usually produce characteristic radiation from a molybdenum anode, MoKα, with a wavelength, λ, of 0.71073 Å. If longer wavelengths are required, copper may be used as the anode to produce CuKα X-rays, λ =1.5418 Å (this wavelength is used more for proteins).

A more powerful source of X-ray is that generated from a synchrotron source in which electrons are accelerated around a very large ring to nearly the speed of light. As the electrons are constantly accelerating, (a result of travelling at a constant angular rotation) very high intensity radiation is emitted at a tangent to

the curve of the ring. The radiation emitted is polychromatic but can be tuned to produce very high intensity monochromatic X-rays *(Figure 2-2-3).*

Figure 2-2-3. View of a synchrotron source which generates a high intensity of X-ray. Electrons are accelerated around a very large ring to nearly the speed of light. As the electrons are constantly accelerating, very high intensity radiation is emitted at a tangent to the curve of the ring. http: Wikipedia.org/synchrotoron_light (14.12.2011)

2-2-2. X – Ray Measurements (Detectors)

An X-ray detector's response to the energy of the diffracted beam is proportional to the number of photons it delivers. From around the 1960s, computer-controlled detectors became the standard means of collecting diffraction data, replacing photographic film. Initially, the most commonly used detector, a scintillation counter, contained a material such as thallium doped sodium iodide, which produced light in the visible region when X-rays fell on it. A

photomultiplier amplified the signal so that the overall effect was an electrical pulse for each X-ray photon incident on the face of the detector, which was typically a few millimetres in diameter. More recently, Charge Coupled Device (CCD) detectors have become the norm. These are position-sensitive and allow X-rays to be recorded over a considerably larger area. A number of incident beams can be recorded at the same time, and their positions as well as intensities are known *(Figure 2-2-4).*

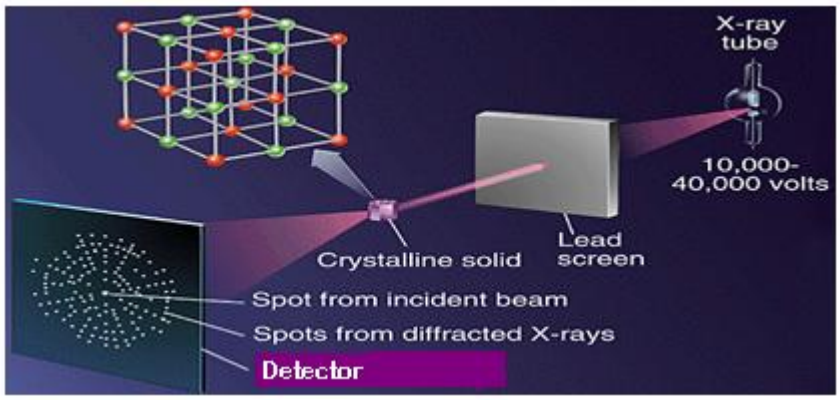

Figure 2-2-4. This is a simple picture of an X-ray diffractometer. The X-ray is generated in an x-ray tube and is diffracted after hitting a single crystal. A detector collects all scatters as spots. http: district87.org/x-ray (14.12.2011)

2-3. Crystallography

2-3-1. Unit cells and Crystal lattices

Crystal's present matter in its most highly ordered form. This high degree of order provides the possibility of imaging the molecules, since all the units that build up the crystal are completely identical, and have an identical environment.

Crystals are characterized by periodicities in three dimensions. Every crystal has a *lattice* as its geometrical basis. The lattice shows the repeating nature of the crystal structure. A lattice may be described as a regular, infinite arrangement of points in which every point has the same environment as any other point. This description is applicable, equally, in one, two and three dimensional space. To define the repeat geometry of the structure in a two dimensional space, a parallelogram of four lattice points is chosen, and is called the *unit cell* of the structure; it has two different sides (a, b) and one included angle(α). Obviously, many different choices of unit cell are possible for any one lattice. There are conventions to guide this choice. In the absence of any rotation or reflection symmetry in the structure, the conventional unit cell has sides as short as possible, $a \leq b$, and an angle as close as possible to 90°. Then each unit cell contains parts of several molecules, and the total contents are just one molecule. Each unit cell contains the equivalent of one lattice point.

These conventional choices of crystal axes and sides classify the possible crystal symmetries into *crystal systems (Table 2-3-1)*.

In three dimensions, a unit cell has three sides and three angles. Conventionally the three lengths are called a, b, c, and three angles α, β, γ, such that α lies between the b and c axes *(Figure 2-3-1).* (Clegg 2008).

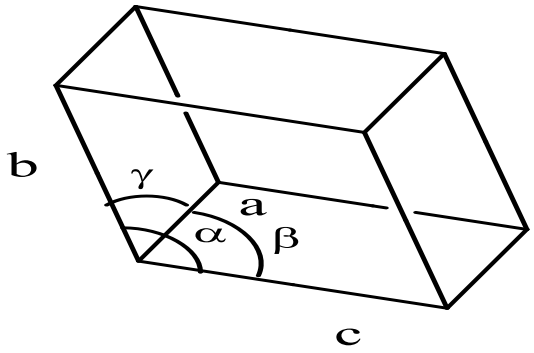

Figure 2-3-1. Illustration of a three dimensional unit cell, a b, and c must be between β and γ, α and γ, and α and β. All the angles must be near 90°

Table 2-3-1. The crystal systems

Crystal system	Essential symmetry	Restrictions on unit cell	Diagram
Triclinic	None	None	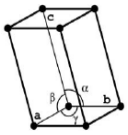
Monoclinic	One two-fold rotation and/or mirror	α=γ=90°	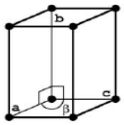
Orthorhombic	three two-fold rotations and/or mirrors	α=β=γ=90°	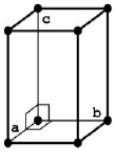
Tetragonal	one four-fold rotation	a=b; α=β=γ=90°	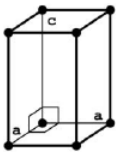
Rhombohedral	one three-fold rotation	a=b=c; α=β=γ (≠90°)	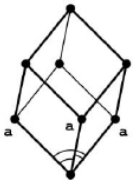
Hexagonal	one six-fold rotation	a=b; α=β=90°;γ=120°	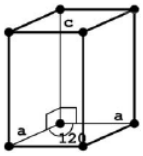
Cubic	four three-fold rotation axes	a=b=c; α=β=γ=90°	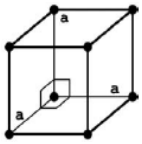

2-3-2. Symmetry and Space groups

Symmetry is perhaps the most fundamental property of the crystalline state. A crystal could be considered symmetrical if, after an operation, real or imaginary, it is indistinguishable from the way it was initially. The symmetry operation could be a rotation about a fixed axis, or a reflection in a mirror plane or a translation of the entire crystal in a given lattice direction. The geometrical entity with respect to which the symmetry operation is performed, an axis or a plane in the example cited, is called symmetry element.

Point groups are defined as having at least a point that remains un-moved by the operations of the point group. Here if the point group has a centre of inversion it will coincide with the centred point.

If the point group has a rotation axis or axes they must pass through this central point and any mirror plane(s) must do the same.

In addition to the usual mirrors (m) and rotation axes (1, 2, 3, 4, 6)**, point operations include improper axes ($\bar{1}$, $\bar{2}$, $\bar{3}$, $\bar{4}$ and $\bar{6}$), which combine a rotation with inversion. Hence $\bar{2}$ is the same as m as $\bar{1}$ signifies an inversion

**Note, 5 is missing from crystal symmetry because it does not tessellate.

In contrast space groups can contain symmetry elements that are produced by the combination of translation with rotations and mirror reflections which are respectively called screw axes and glide planes. (*Figure 2-3-2)*

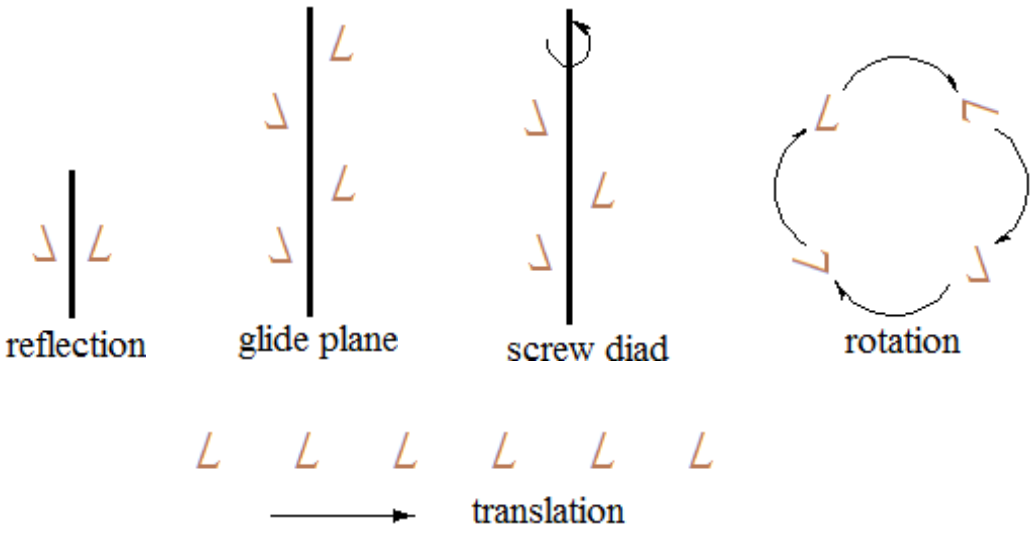

Figure 2-3-2. Illustration of some crystallographic symmetry elements. Reflection is a mirror-like image, glide plane is displacement of two mirror images, screw is a rotation by 180˚ with a translation

There are 230 space groups in three dimensions representing the distinct ways of arranging identical objects which are made from the combinations of 32 crystallographic point groups, with 14 *Bravais* lattices, each of the latter belonging to one of the 7 lattice systems.

In *Table 2-3-2* the 32 crystallography point groups are shown for the seven crystal systems.

Table 2-3-2. The 32 crystallography point groups and 14 *Bravais* lattices represented for each crystal system

Crystal systems	Bravais lattices	Point groups
Triclinic	P	1, -1
Monoclinic	P C	2, m, 2/m
Orthorhombic	P C I F	222, mm2, mmm
Tetragonal	P I	4, -4, 4/m, 422, -42m, 4mm, 4/mmm
Rhombohedral	R	3, -3, 32, 3m, -3m
Hexagonal	P	6, -6, 6/m, 622, -62m, 6mm, 6/mmm
Cubic	P I F	23, m-3, 432, -43m, m-3m,

There are some additions which will help to visualize and understand space groups. The selection of a unit cell has three options: the cell should be the smallest and simplest but with the highest symmetry. The simplest cell, P (primitive) has a node located at the unit cell corners with coordinates (0, 0, 0) in which all the translations are equivalents and the (P) cell makes a single lattice. In some situations a larger unit cell is selected with an additional node at its centre cell (I), with coordinates (1/2, 1/2, 1/2), which makes a double lattice, alternatively a node in the middle of the ab face is operated by C, with coordinates (1/2, 1/2, 0) which also makes a double lattice, if a node is placed each faces the cell is F centred, with coordinates (1/2, 1/2, 0), (1/2, 0, 1/2) and

(0, 1/2, 1/2), which makes a quadruple lattice. These unit cells are illustrated in *Figure 2-3-3*. There are 14 unique possibilities of unit cells for each crystal system known as the Bravais lattices which are demonstrated in *Table 2-3-2.* Glusker & Trueblood (1985)

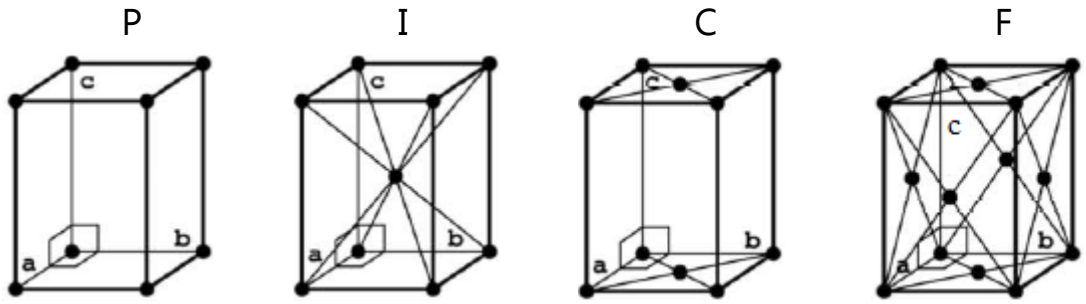

Figure 2-3-3. The illustration of lattices in unit cells for P (primitive), I (centre), C (opposite face centre) and F (face centre) cells

2-4. Interaction of X-rays with Crystal

2-4-1. X-Ray diffraction

If an X-ray photon encounters an electron, it may be absorbed, setting the electron into vibration at the X-ray frequency. The electron vibration emits an X-ray photon of the original energy and wavelength in a random direction. This is called coherent scattering and is the most likely outcome when an X-ray photon encounters an electron in an atomic orbital. This can be thought of as equivalent to diffraction by single electron. This makes the resulting image truly three-dimensional, with no special difference

in representation or accuracy for different directions. One atom cannot hide behind another.

Another possibility is incoherent scattering, which releases energy in the atom, leaving it in an excited state. Radiation damage is a consequence of incoherent scattering, while crystallographic structure determination depends upon coherent scattering. X-ray scattering experiments show electrons and the structural results represent distributions of electron density.

Although an individual electron scatters uniformly in every direction destructive interference occurs between the X-rays scattered by the electron cloud in an atoms so that scattering intensity falls off with increasing angle relative to the direct beam. Also each atom is part of a repeating array within a crystal so that the resulting diffraction pattern consists of regions of dark and light where there scattered waves participate in distractive and constructive interference respectively (*Figure 2-4-1).*

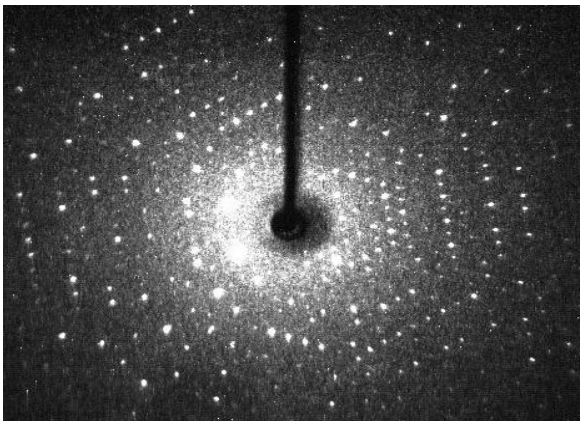

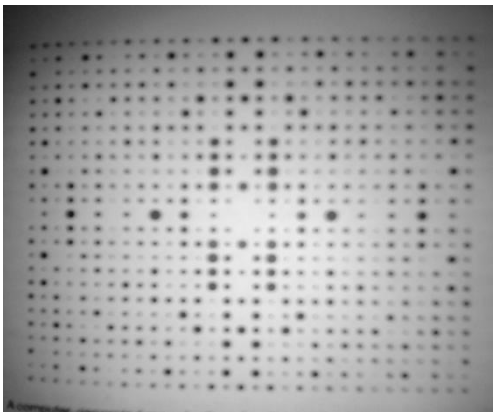

(a) **(b)**

Figure 2-4-1. The patterns formed when X-rays are scattered by a single crystal: (a) X-ray scattered by single crystal recorded by CCD detector, (b) the diffraction pattern after computer processing

The pattern of spots has three properties of interest, which correspond to three properties of the crystal structure.

Firstly the pattern has a particular geometry. The spots lie in certain positions which are clearly not random. This pattern geometry is related to the lattice and unit cell, which are, in turn, determined by the bond lengths, bond angles, and other features of the geometry of molecules and their relationship with other molecules in the unit cell.

Secondly the pattern has symmetry, in the regular arrangement of the symmetry related positions relative to the centre of the pattern. The pattern in *Figure 2-4-1* has both vertical and

horizontal reflection symmetry and an inversion point at the centre.

Thirdly each spot has an individual intensity. These intensities hold all the available information about the positions of the atoms in the unit cell of crystal structure. It is the relative atomic positions, which, through the combination of their individual interactions with the X-rays, generate different amplitudes for different directions of scattering.

In the most usual case, X-ray diffraction uses an X-ray beam having all component waves of the same wavelength. Such an X-ray beam is called monochromatic.

2-4-2. Diffraction Geometry

In diffraction by a repetitive object, rays are scattered in many directions. Each unit of the lattice scatters, but a diffracted beam arises only if the scattered rays from each unit are all in phase. Otherwise the scattering from one unit is cancelled out by another. In two dimensions, there is always a direction where the scattered rays are in phase for any order of diffraction. In three dimensions, it is only possible for all the points of a lattice to scatter in phase if the crystal is correctly oriented in the incident beam.

Consider first diffraction by a single row of regularly spaced points (one dimensional diffraction) *Figure 2-4-2*.

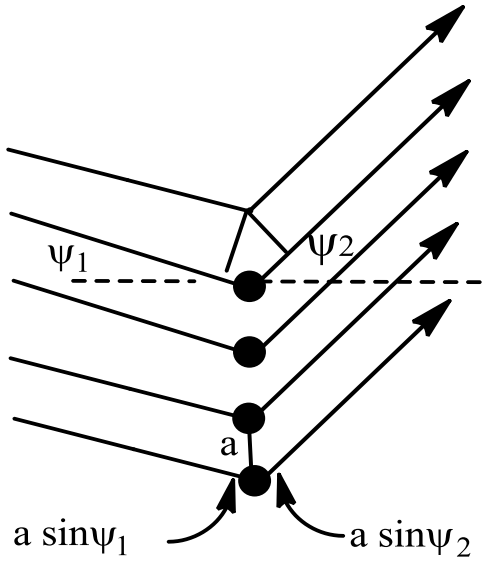

Figure 2-4-2. Diffraction by a single row of regularly spaced points

In a particular direction, the radiation scattered by the row of points, if we accept they are all in phase, the straight through direction, individual rays have different path lengths; these path differences must be equal to whole numbers of wavelengths to keep the rays in phase. For rays scattered by two adjacent points in the row:

$$h\lambda = a\sin\psi_1 + a\sin\psi_2$$

λis the wavelength, ***a*** is the one dimensional lattice spacing, ***h*** is an integer (positive, zero, or negative), ψ_i and ψ_d are the angles of the incident and diffracted beams.

For diffraction by a three dimensional lattice there are three such equations. The first equation contains the lattice ***a*** spacing, angles relative to this ***a*** axis of the unit cell, and an integer ***h***. The other two equations, correspondingly, contain the unit cell axes ***b*** and ***c***, and integers ***k*** and ***l*** respectively.

When $\psi_i = \psi_d = \Theta$ and $a=d$, for rays are behaving as they would if they were being reflected by two adjacent planes.

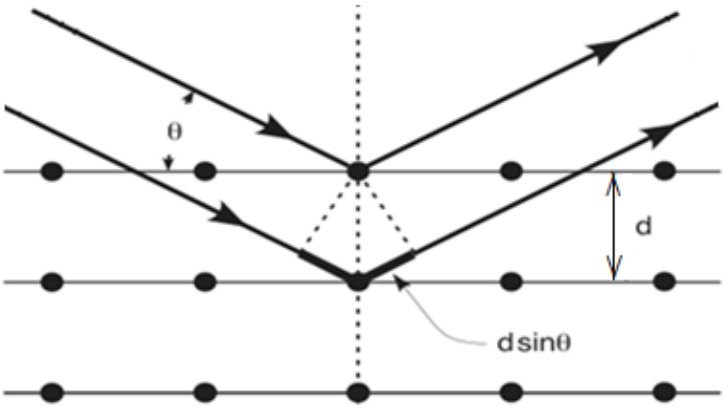

Figure 2-4-3. The Bragg construction for a three dimensional crystal structure; one set of parallel lattice planes is seen edge on.

$$n\lambda = 2d_{hkl}\sin\Theta \qquad (1)$$

This is equivalent to the *Bragg equation formula (1)*. The three integers, ***h, k*** and ***l***, specify the intercepts of the Bragg plane on the three unit cell edges, ***a, b*** and ***c*** respectively. The *Bragg equation* is universally used as the basis for X-ray diffraction geometry. Bragg showed that every diffracted beam that can be produced by an appropriate orientation of a crystal in an X-ray beam can be regarded geometrically as if it were a reflection from sets of parallel planes passing through lattice points. It is analogous to the reflection of light by a mirror, in that the angles of incidence and reflection must be equal and the incoming and outgoing beams, and it is normal that the reflecting planes must themselves all lie in one plane.

2-4-3. Intensities of diffracted X-rays, Fourier transform

Diffraction in real crystals differs from the idealized Bragg situation in two ways, first when X-rays are scattered by electrons, the scattering factor (f_j) for a real atom is equal to the atomic number (Z), but only for $\theta = 0$. It falls off with increasing

angle due to destructive interference within the atom's electron shells.

Second the atoms are distributed across the unit-cell x_1, y_1, z_1....x_j, y_j, z_j, not just at lattice points (0, 0, 0). As there is a shift in the phase of the reflected wave by 2π in traversing from one Bragg plane to the next j's phase will be shifted by $2\pi(hx_j + ky_j + lz_j)$. The scattered waves must therefore be summed taking the phase shifts into consideration.

$$F(hkl) = \sum f_j \left[\cos 2\pi(hx_j + ky_j + lz_j) + \mathbf{i}\sin 2\pi(hx_j + ky_j + lz_j)\right] \quad (2)$$

The equation *(2)* describe the summation of vectors with length f_j and phase $\phi = 2\pi(hx_j + ky_j + lz_j)$. An example has been given in *Figure 2-4-4.*

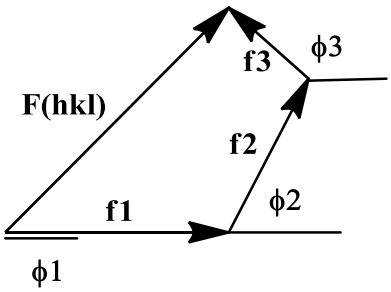

Figure 2-4-4. Waves represented as vectors (f amplitudes and ϕ phases).The summation of f1, f2 and f3 gave the structure factor F(hkl)

Where *F(hkl)* is known as the structure factor for plane *hkl* and is equivalent to:

$$F(hkl) = \sum f_j \exp 2\pi i (hx_j + ky_j + lz_j)$$

The Fourier transform equation will calculate just one single X-ray reflection, the equation itself has a fearsome appearance, the mathematical calculations for a whole crystal structure is massive, however it is fortunate that all the calculations are performed by computers.

The determination of electron density throughout the crystal is the main subject of X-ray crystallography. Electron density $\rho(xyz)$ is the Fourier transform *F(hkl)* and is calculated by the following equation:

$$\rho(xyz) = \sum_{\text{all hkl}} F(hkl) \exp [-2\pi \mathbf{i}(hx + ky + lz)]$$

The intensity of a diffraction pattern is in proportion to the square of the structure factor amplitude, $|F(hkl)|^2$. The structure factor is a complex number containing information regarding amplitude and phase of a diffraction wave *(see Figure 2-4-4)*. Also the electron

density map is provided by amplitude and phases. Although the amplitudes are measured in a diffraction experiment the phases have been lost.

In order to recover the missing phase information two main methods are used, Patterson function and direct methods.

The Patterson function is used to locate heavy atoms in a structure. It is a 3 dimensional map calculated by Fourier transforming $F^2(hkl)$ instead of F(hkl). The Patterson map is a superposition of distances, A---B, between pairs of atoms A and B, in which A is always on the origin of the map. The peak intensity is proportional to $Z_A \times Z_B$.

Once the heavy location is known its fractional coordinates can be used to calculate the approximate phases of measured structure factor amplitudes. These phases can then be applied to the measured structure factor amplitudes and an electron density map synthesised. This map will show not only the input heavy atom but also electron density peaks corresponding to the lighter atoms in structure.

In contrast to heavy atom method Direct methods do not require a heavy atom in order to phase the reflections. Direct methods is a numerical method based on simple facts such as the electron density within a unit-cell does not drop below zero at any point. This leads to probabilistic relationships such as: if F(hkl) and F(2h,

2k, 2l) are both large then their phase must be the same. By identifying phase relationships between the most intense reflections it is possible to reduce the number of unknown phases to just a handful. Once this is done a full set of phases is calculated for each permutation of the unique phases and figures of merits produced to compare the quality of the resulting Fourier maps. Only the electron density map with the best figure of merit is accepted and progressed to the next stage.

By using either heavy atom or Direct Method structure is solved and it is now possible to produce a Fourier Map of electron density $\rho(xyz)$ within the unit-cell.

The Fourier map is searched automatically to produce a list of peak heights and their locations in fractional atomic coordinates, x_j y_j z_j. Molecular graphics packages are then used to display the results in the form of molecules on the computer screen. At this stage the atoms can be named and any weak peaks removed from the atom list.

2-4-4. Least Squares

It is now possible to start refining the structure. F_c is the calculated structure factor; $|F_o|$ is the amplitude of the measured structure

factor. Observed for each structure factor, which is only amplitudes $|F_o|$ no phases ϕ_o.

If the approximate positions of most of the atoms in the structure are known, it is possible to start least squares refinement whereby the value of R in the equation below is minimised.

$$R = \frac{\sum | \, | Fo | \, - | Fc | \, |}{\sum |Fo|}$$

The equation above is used to determine R, which is known as a residual or R-factor. It allows the quality of two structure refinements to be compared.

As each reflection has its own weight, *w*. *w* R is similar to R except $|F_o|$ is weighted according to its accuracy and F^2 is generally used instead of |F|.

$$wR2 = \sqrt{\frac{\sum w(F_0^2 - F_c^2)^2}{\sum w(F_0^2)^2}}$$

The value of wR2 is reduced by Least Squares refinement. This is an iterative process whereby the correction required to improve each parameter is calculated each cycle. The corrections are applied and further cycles of Least Squares carried out.

The refinement is considered complete when it has converged and no significant residual electron density is observed in the $\Delta\rho$ map. Additionally, a check is carried out for chemical integrity and adjustments made as required, e.g. fixing missing hydrogen atoms.

For complete refinement of the structure which shows the correct positions for all the atoms, R is typically around 0.02-0.09.

2-4-5. Estimated standard deviation

Estimated standard deviation (e.s.d.), is measurement of the precision of quantities and show how much variation or dispersion from the average exists. A low standard deviation indicates that the data points tend to be very close to the expected value and a high standard deviation indicates that the data points are spread out over a large range of values.

A good refinement method must provide reliability e.s.d. of various refine parameters. These values are related to the quality of the refinement and are indications of the relevance of parameters.

Figure 2-4-5 shows a normal curve with probabilities of a parameter value falling within certain e.s.d. ranges marked.

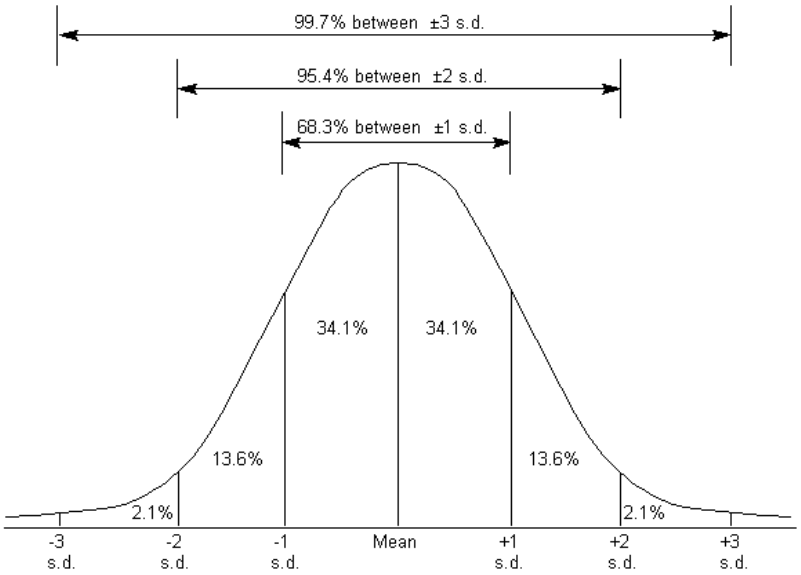

Figure 2-4-5. A normal curve predict that roughly 68% of the values will fall within one standard deviations, and almost every value (99%) within 3 standard deviations.

2-5. Experimental Actions

A series of experimental steps have to be carried out in order to gather a full crystallographic data set.

1) Crystal growth: Crystals can appear as a solution cools or through evaporation of the solvent. Sometimes this does not happen and the solid has to be re-dissolved and the above processes repeated. Slowing the process down usually helps or possibly changing the solvent.

2) A small amount of the sample is immersed in Fomblin oil for protection from the atmosphere whilst a suitable single crystal chosen using a polarizing microscope. A small size and uniform dimensions are preferable for samples containing heavy atoms,

and very small crystals can be examined with intense synchrotron radiation. Once a single crystal has been selected, it is picked up on a 0.1 mm glass fibre attached to a goniometer head. The head is mounted on the X-ray diffractometer and cooled to 100K (for most of the work) using the integral Cryostream. The Fomblin oil freezes on cooling, fixing the crystal firmly to the glass fibre, prior to alignment using the instrument's video telescope.

3) the gonimeter is gradually rotated whilst the crystal is bombarded with X-rays producing a diffraction pattern of regularly spots known as reflections.

4) Determination of the unit-cell: Use the CCD detector to record ten diffraction images at various crystal angles. Process the images to determine the reflection angles and hence determine the unit-cell dimensions and crystal class.

5) Collect a full set of reflections, appropriate for the crystal class, as indicated by the diffractometer control software e.g. SUPERGUI. All measurements are carried out using either graphite monochromated MoKα radiation, λ = 0.71073 Å or CuKα radiation, λ = 1.5418 Å. X-ray images are recorded on the CCD detector and stored for further processing.

6) Once a full set of images have been collected reflections are harvested using data processing software on the diffractometer e.g. SORTAV to produce a reflection data set (h, k, l, F^2, $\sigma(F^2)$). The

software will also scale and correct for Lorenz, polarization and absorption effects.

7) the data set is then handed over to structure solution and refinement packages *table 2-5-1*, leding eventually a CIF file containing full details of the crystal structure as well as the structure determination process.

Table 2-5-1. Programs for solving, refinement, and analysing small single crystal

Performances	Programs Name
Graphical User Interface (GUI), Microsoft windows system used for accessing programs for solving, refining and analysing single crystal X-ray diffraction data for small molecules and has interfaces to other popular programs such as Shelx-97 and SirWare programs (Sir-97, Sir-2004).	WinGX, Olex2
A set of programs for the solving of single crystal X-ray and neutron diffraction of small molecule and macromolecule structure.	Shelxs (Direct Methods and Patterson), Sir92-97 (Direct Methods), Olex2-solve (Charge-Flipping)
Least Squares refinement of the crystal structure	Shelx97
Preparation of Data for publication	WinGX, PublCIF
Molecular Graphics	Ortep, Mercury, Platon

2-6. References

http: Wikipedia.org/electromagnetic spectrum (14.12.2011)

http: Wikipedia.org/X-ray_tube (14.12.2011)

http: Wikipedia.org/synchrotoron_light (14.12.2011)

http: district87.org/x-ray (14.12.2011)

Clegg, W., Crystal Structure Determination., (2008), *Oxford University Press.*, **60**

Glusker, J. P., Trueblood. K. N., Crystal Structure Analysis a primer., (1985), *Oxford University*

3- Iodides and polyiodides

Work contain within the chapter has already been published namely Hydrogen bis[tris(4-fluorophenyl)-phosphine oxide] triiodide (Haghjoo, 2012), Bis(methyltri-o-tolylphosphonium) octaiodide (Haghjoo, 2011)

3-1. Introduction

Elemental iodine was first observed by Bernard Courtois over 200 years ago as a violet vapour that resulted from reducing the iodide in seaweed ashes using concentrated sulphuric acid (Courtois, 1813).

$$2\,I^- + H_2SO_4 \rightarrow I_2 + SO_3^- + H_2O$$

Since then its biological importance has been realised, it has become a staple of synthetic reactions and, because of its ability to catenate, has developed an extensive supramolecular chemistry (see the excellent review by Kopper et al, 2011).

Iodine and iodide supramolecular interactions generate a variety of polyiodides, ranging from the ubiquitous triiodides to chains and networks that extend throughout a crystal (Svensson & Kloo, 2003). Similar interactions are observed between iodine and metal iodides such as in the $...Hg_2I_6^{2-}...I_2...Hg_2I_6^{2-}...$ chains formed

by the reaction of the mercury hexamethylenetetramine iodide, $HgI_2(C_6N_4H_{12})$ and HI (Svensson & Kloo, 1999) and $...Cd_2I_6^{2-}...I_2...Cd_2I_6^{2-}...$ formed by the reaction of $[Me_3S][I_5]$ and CdI_2 (Svensson et al, 1998). In both these cases the I_2 bond length remains close to 2.7 Å, representing a full sigma bond and the I...I distance between the iodide and iodine approximately 3.4 Å, which represents a bond order of only 0.14, but this is still considered intramolecular (Svensson & Kloo, 2003; Pritchard & Moreland, 2006).

This contrasts with the electrically conducting products formed when benzophenone reacts with alkali metal iodides and I_2 (Coppens et al, 1983). These crystals contain iodine columns, which repeat along the crystal ***c*** axis with an average I-I separation of 3.07 Å, representing an average bond order of 1.5, although the iodine columns in the crystals actually consist of a random array of different iodine species. A similar situation can be observed in alpha-cyclodextrin metal iodide inclusion compounds, which can be loaded with additional I_2 to form long polyiodide chains within the cavities extending through the crystal structure (Rietman, 1990).

More recently, attention has focused on intramolecular interactions of iodine and iodides in Grätzel photovoltaic cells. The photo-oxidised ruthenium complex in the Grätzel cell is regenerated by accepting an electron from I^- to form I_3^- (see

Chapter 1).

Privalov (2009) and Schiffmanna (2010) looked at specific interactions of the I^-/I_3^- redox mediators with the reduced and oxidized dye, Ru(4,4′-dicarboxy-2,2′-bipyridyl)$_2$(NCS)$_2$, using density functional theory and identified interactions between iodide and the capping NCS sulphur as well as the bipyridyl groups. The interactions between iodide species and metal-free triphenylamine–cyanoacetic acid dyes have also been studied using quantum mechanical calculations (Nyhlen et al, 2010).

The work described in this chapter is designed to extend our understanding of the types of interactions that iodine participates in the solid state and will start with the synthesis and structural characterisation of methyltri-o-tolylphosphonium iodide. This will be followed by a description of the preparation and characterisation of a series of its co-crystallisation products with increasing quantities of iodine. The final crystal structure presented in this chapter will be hydrogen bis[tris(4-fluorophenyl)-phosphine oxide] triiodide, which will provide an interesting comparison with the methyltri-o-tolylphosphonium series.

3-2. Methyltri-o-tolylphosphonium iodide (I)

The asymmetric unit of structure I consists of two crystallographic ally independent methyltri-o-tolylphosphonium cations and accompanying iodide counterions, as illustrated in *Figure 3-2-1*.

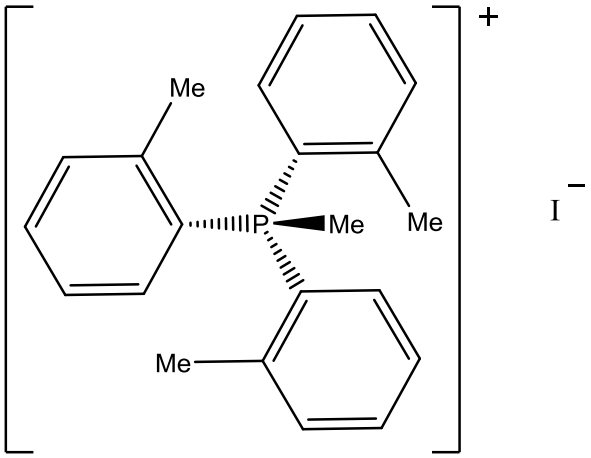

(I)

Scheme 1. Illustration of compound **(I)**

Crystallographic parameters are presented in *Table 3-2-1* and selected bond lengths and angles in *Table 3-2-2*.

Table 3-2-1 Crystal data for structure **I**

Chemical formula	$C_{22}H_{24}IP$
M_r	446.09
Crystal system, space group	Monoclinic, $P2_1/n$
Temperature (K)	100
a, b, c (Å)	10.4966 (3), 19.9937 (5), 19.2107 (5)
β (°)	90.747 (1)
V (Å^3)	4031.33 (19)
Z	8

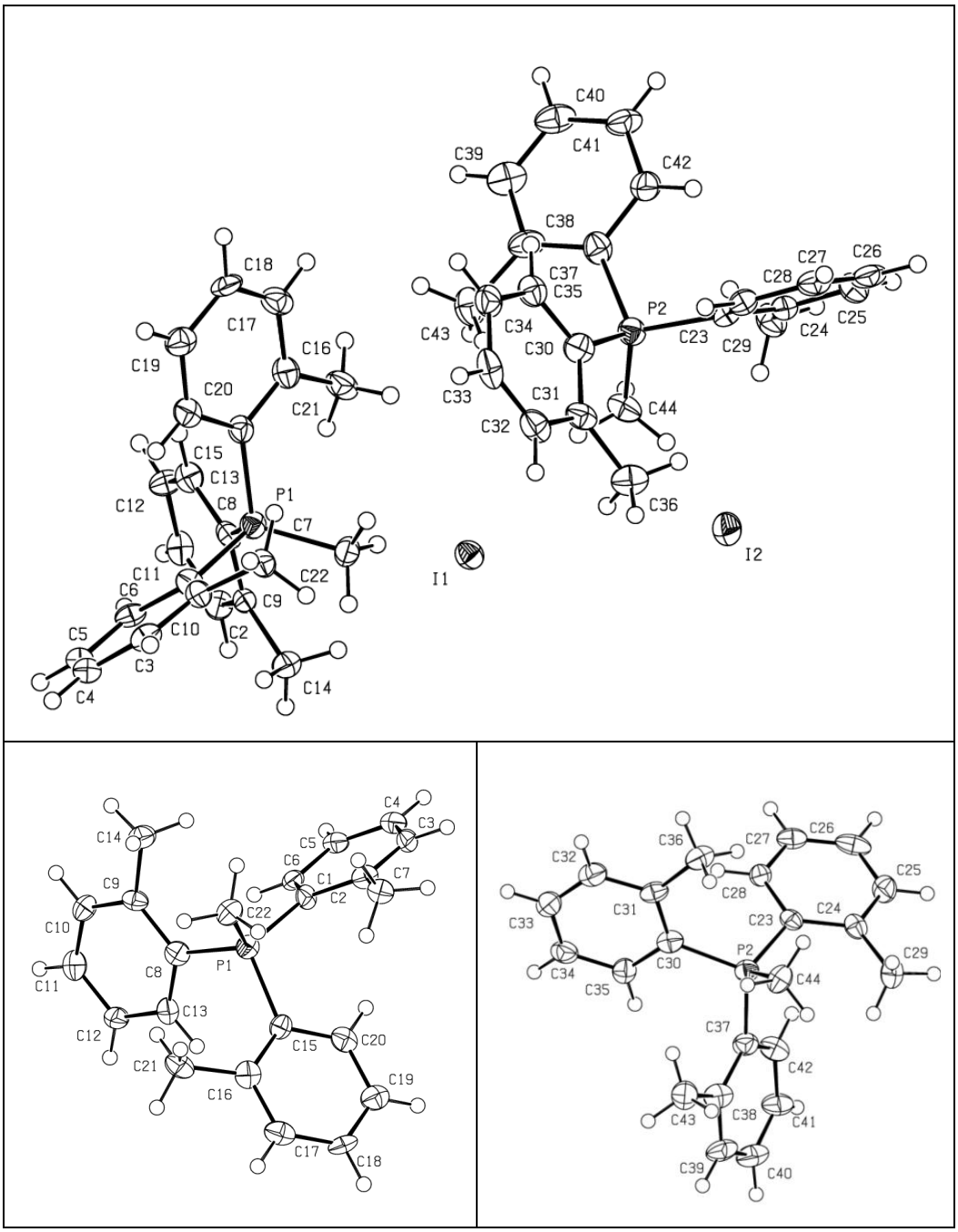

Figure 3-2-1. Top – A labelled ORTEP view of the asymmetric unit of structure **I**. Bottom – Individual views of the methyltri-o-tolylphosphine cations showing their exo_3 configurations

Table 3-2-2. Selected geometric parameters (Å, º) for structure **I**

C1—P1	1.811 (9)	C23—P2	1.810 (9)
C8—P1	1.805 (9)	C30—P2	1.801 (10)
C15—P1	1.802 (9)	C37—P2	1.812 (10)
C22—P1	1.797 (9)	C44—P2	1.790 (9)
C22—P1—C15	108.4 (4)	C44—P2—C30	111.4 (4)
C22—P1—C8	112.8 (4)	C44—P2—C23	111.1 (4)
C22—P1—C1	110.1 (4)	C44—P2—C37	109.3 (5)
C22-P1-C15-C16	55.4 (8)	C44-P2-C37-C38	54.7 (9)
C22-P1-C1-C2	50.4 (8)	C44-P2-C23-C24	50.1 (8)
C22-P1-C8-C9	48.8 (9)	C44-P2-C30-C31	45.5 (9)

The geometries of both cations are identical within experimental error, including the C_{me}-P1-C-C_{me} and C_{me}-P2-C-C_{me} torsion angles of 48.8 (9), 50.4 (8), 55.4 (8)° around P1 and 45.5 (9), 50.1 (8) and 54.7 (9)° around P2, clearly indicating that both configurations are exo_3. A previous example of the use of exo notation in tri-o-tolyl derivatives of P, As and Si is given by Howell et al. (1992). exo_3 is the expected configuration for a tri-o-tolylphosphine moiety with its small apical substituent [*cf.* $(o\text{-tolyl})_3P{=}O$, which is also exo_3 and whose corresponding torsion angles fall in the range 33.8–52.4°, with an average of 45.9°]. The larger torsion angles in the

cations in **I** reflect the slightly larger size of CH_3 relative to O and indicate that it must be close to the upper limit for the exo_3 configuration *(Table 3-2-3).* The size of the apical substituent in (o-tolyl)$_3$P=S flips the structure to an exo_2 configuration even though, according to Pauling, CH_3 has a larger van der Waals radius than S. This is because H atoms of the ortho-CH_3 groups nestle between the H atoms of the apical CH_3, effectively reducing the van der Waals radius of the methyl group. A molecular mechanics method applied by Fey et al (2006) to predict the conformation of triarylphosphines also identifies the size of the apical substituent as a key factor in determining the conformation.

Table 3-2-3. Comparison of the Me-P-C-C torsion angle in $[(C_7H_7)_3PMe]^+$ with those in the series $(C_7H_7)_3P=X$ (X = O, S, Se).

	X- P-C-C torsion angles (°) (where X=O, S, Se, Me or lone pair)			Average torsion (°)
Tri-o-tolylphosphine	46.8	40.7	45.6	43.6
	36.7	49.0	43.1	exo_3
Tri-o-tolylphosphine-methyl	50.8	50.8	50.8	50.8
				exo_3
Tri-o-tolylphosphine-oxide	52.4	44.5	43.2	45.9
	44.6	51.7	44.3	exo_3
	51.1	47.6	33.8	
Tri-o-tolylphosphine-sulphide	66.9	3.4	52.6	exo_2
	17.0	56.6	56.5	
Tri-o-tolylphosphine-selenide	56.3	58.3	13.0	exo_2

The iodide anions are housed in the channels formed by stacks of the phsophonium cations *(Figure. 3-2-2 - Top)*, however as the

closest I…I approach is 5.818 (1) Å, the iodides are non-interacting. Interestingly eight H atoms are within the Van der Waals (VDW) distances stored in Mercury (Macrae, 2008) to I1, whereas none of the I2….H contacts fall in this range and required the cut-off to be raised to VDW + 0.2 Å in order to reveal the iodine environment illustrated in *Figure. 3-2-2*.

The recently revised VDW distances compiled by Alvarez (2013), some of which are shown in *Table 3-2-4*, bring more I…H contacts within the VDW range but the radii would require further upward revision to generate all the illustrated "contacts". Indeed the older 3.35 Å I…H VDW contact distance of Harrison (1978) provides a more uniform angular distribution around I^-.

Table 3-2-4. Revised Van der Waals radii (Alvarez, 2013)

element	$\mathbf{r_{VDW}}$ (Å)
H	1.20
I	2.04
Cl	1.82
P	1.90
C	1.77

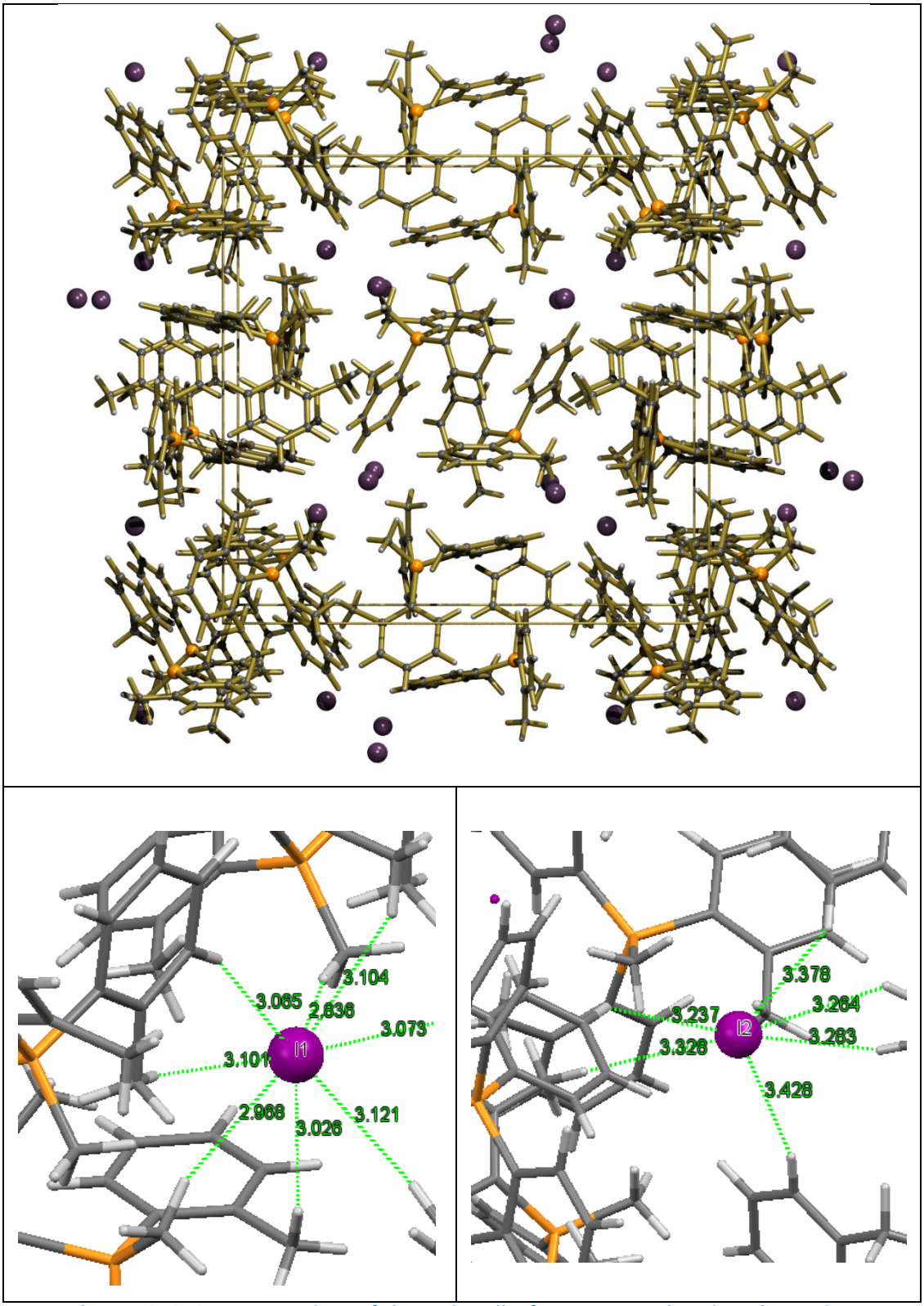

Figure 3-2-2. Top – A view of the unit cell of structure **I** showing the cations columns and the iodine chanels they encompass. Bottom – Individual views of the iodide environments, showing the closest contacts.

Although the H…I interactions are variable and generally weak in this structure, π-π overlap between the two crystallographic unique methyltri-o-tolylphosphonium cations is a significant feature of the packing in crystals of **I** *(Figure. 3-2-3)*.

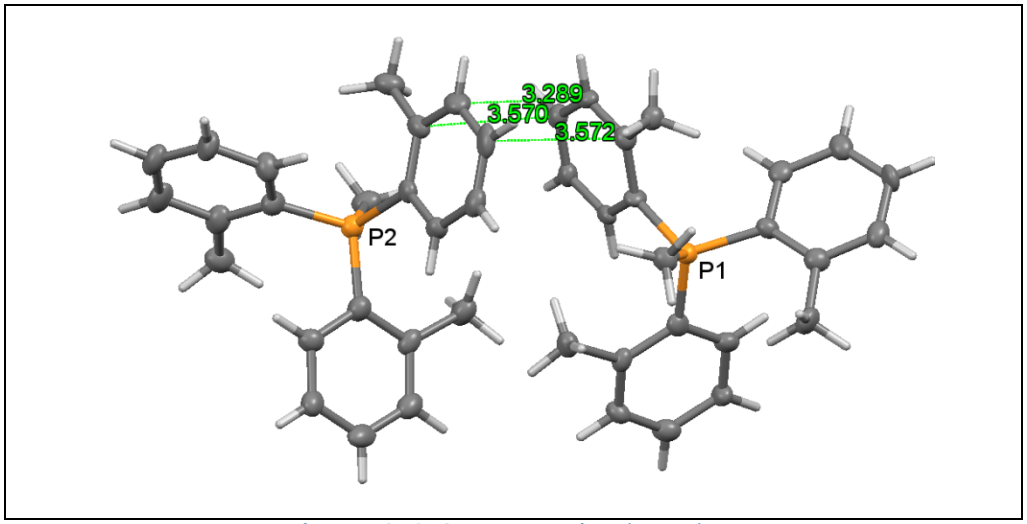

Figure 3-2-3. π-π overlap in cation **I**

3-2-1. Experimental

Details of data collection and least-squares refinement are presented in *Table 3-2-5*. All non-hydrogen atoms were refined anisotropically and hydrogen atoms constrained to chemically reasonable positions. The computer software used for the determination is listed. The same software was used for all the work in this Chapter, unless otherwise stated.

Table 3-2-5. Data collection and refinement details for **I**

Diffractometer	Bruker Nonius KappaCCD
Absorption correction	Multi-scan R.H. Blessing, Acta Cryst. (1995), A51, 33-38
T_{min}, T_{max}	0.788, 0.851
No. of measured, independent and observed [$I > 2\sigma(I)$] reflections	42573, 7488, 5173
R_{int}	0.115
$(\sin\theta/\theta)_{max}$ (Å^{-1})	0.606
Refinement	
$R[F^2 > 2\sigma(F^2)]$, $wR(F^2)$, S	0.069, 0.182, 1.02
No. of reflections	7488
No. of parameters	442
No. of restraints	0
H-atom treatment	H-atom parameters constrained
	$w = 1/[\sigma^2(F_o^2) + (0.0613P)^2 + 58.2918P]$ where $P = (F_o^2 + 2F_c^2)/3$
$\Delta\rho_{max}$, $\Delta\rho_{min}$ (e Å^{-3})	1.10, -1.22

3-2-2. Computing details

Data collection: Collect (Nonius BV, 1997-2000); cell refinement: *HKL SCALEPACK* (Otwinowski & Minor 1997); data reduction: *HKL DENZO* and *SCALEPACK* (Otwinowski & Minor 1997); program(s) used to solve structure: *SIR92* (Giacovazzo *et al.*, 1993); program(s) used to refine structure: *SHELXL97* (Sheldrick, 1997); molecular graphics: *ORTEP-3 for Windows* (Farrugia, 1997); software used to prepare material for publication: *WinGX* publication routines (Farrugia, 1999).

3-2-3. Synthesis

Equimolar quantities of methyl iodide and tri-o-tolylphosphine were reacted in dry dichloromethane at room temperature. The containers were stoppered and further precautions to protect the sample from the atmosphere were deemed unnecessary. Anhydrous dichloromethane (25 ml) was added to a dry Rotaflo tube. To this solution was added $(o\text{-}CH_3C_6H_4)_3P$ (1.005 g, 3.30 mmol) which dissolved rapidly. Iodomethane (0.60 ml, 9.91 mol) was added slowly over a period of several minutes. After 5 min, a white solid gradually formed and the reaction was left to stir for a further 24 h. The solid was then isolated using standard Schlenk techniques and dried in vacuo for 2 h to yield 1.394 g of a solid (94.6%yield). Analysis calculated for $C_{22}H_{24}I_4$ P:C 59.2, H 5.4, I 28.5%; found: C 59.1, H 5.3, I 28.1%.

3-2-4. Recrystallisation

0.1 g methyltri-o-tolylphosphonium iodide was dissolved in 3 mL dichloromethane and placed in vial, which was covered with pierced lid in order to facilitate slow evaporation. Suitable crystals formed in 4 days.

3-3. Methyltri-o-tolylphosphine iodide chloroform solvate (II)

In contrast to the unsolvated structure described in the previous section, the chloroform solvate's asymmetric unit consists of one methyltri-o-tolylphosphine cation, its iodide counterion and a chloroform molecule. Crystal details are presented in *Table 3-3-1*, a fully labelled view of the current molecule in *Figure 3-3-1* and selected bond lengths and angles in *Table 3-3-2*.

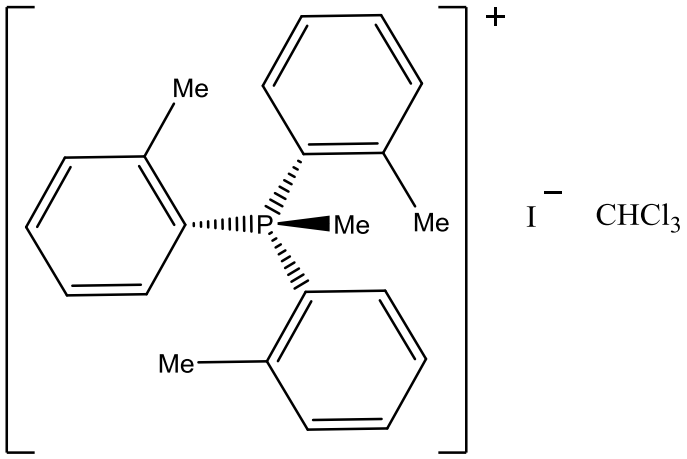

(II)

Scheme 1. Illustration of the compound **II**

Table 3-3-1. Crystal data for structure **II**

Chemical formula	$C_{23}H_{25}Cl_3IP$
M_r	565.45
Crystal system, space group	Triclinic, $P\bar{1}$
Temperature (K)	100
a, *b*, *c* (Å)	10.6838 (3), 10.8473 (4), 11.5357 (4)
α, β, γ (°)	71.930 (2), 86.173 (2), 72.791 (2)
V (Å^3)	1213.58 (7)
Z	2
Radiation type	Mo $K\alpha$
μ (mm^{-1})	1.72
Crystal size (mm)	0.2 × 0.1 × 0.1

The phosphonium cation's geometry in the present structure is identical to that of the analogous phosphonium in **I**. The C_{me}-P-C-C_{me}, torsion angles of -52.6 (4), -54.5 (4) and -49.5 (5) given in *Table 3-3-2* indicate that the configuration is exo_3, showing a good geometric match for the phosphonium cation in **I**.

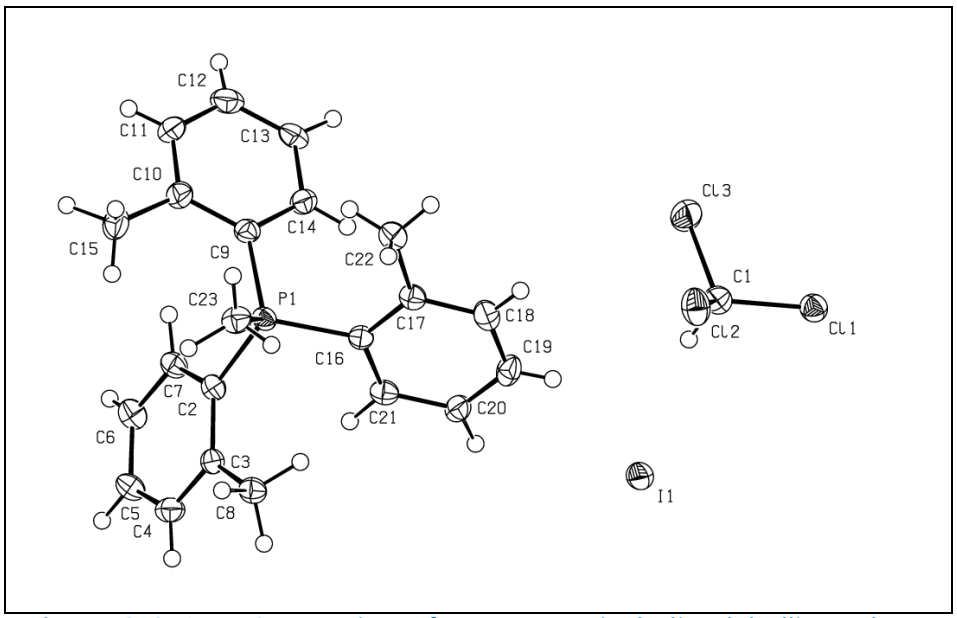

Figure 3-3-1. An ORTEP view of structure **II**, including labelling scheme

Table 3-3-2. Selected geometric parameters (Å, º) for compound **II**

C2—P1	1.806 (4)	C16—P1	1.800 (4)
C9—P1	1.808 (4)	C23—P1	1.807 (5)
C16—P1—C23	109.4 (2)	C23—P1—C9	111.8 (2)
C2—P1—C23	109.3 (2)		
C23-P1-C2-C3	-54.5(4)	C23-P1-C16-C17	-52.6(4)
C23-P1-C9-C10	-49.5(5)		

The most significant differences between **I** and **II** stem from the supramolecular interactions of the chloroform solvate in **II.** *Figure 3-3-2* show how layers of iodide anions are sandwiched between thicker layers of phosphonium cations and chloroform solvate. The relatively acidic chloroform hydrogen atom forms a relatively short non-conventional hydrogen bond to the iodide and one of the chloroform's chlorine atoms also interacts with the iodide.

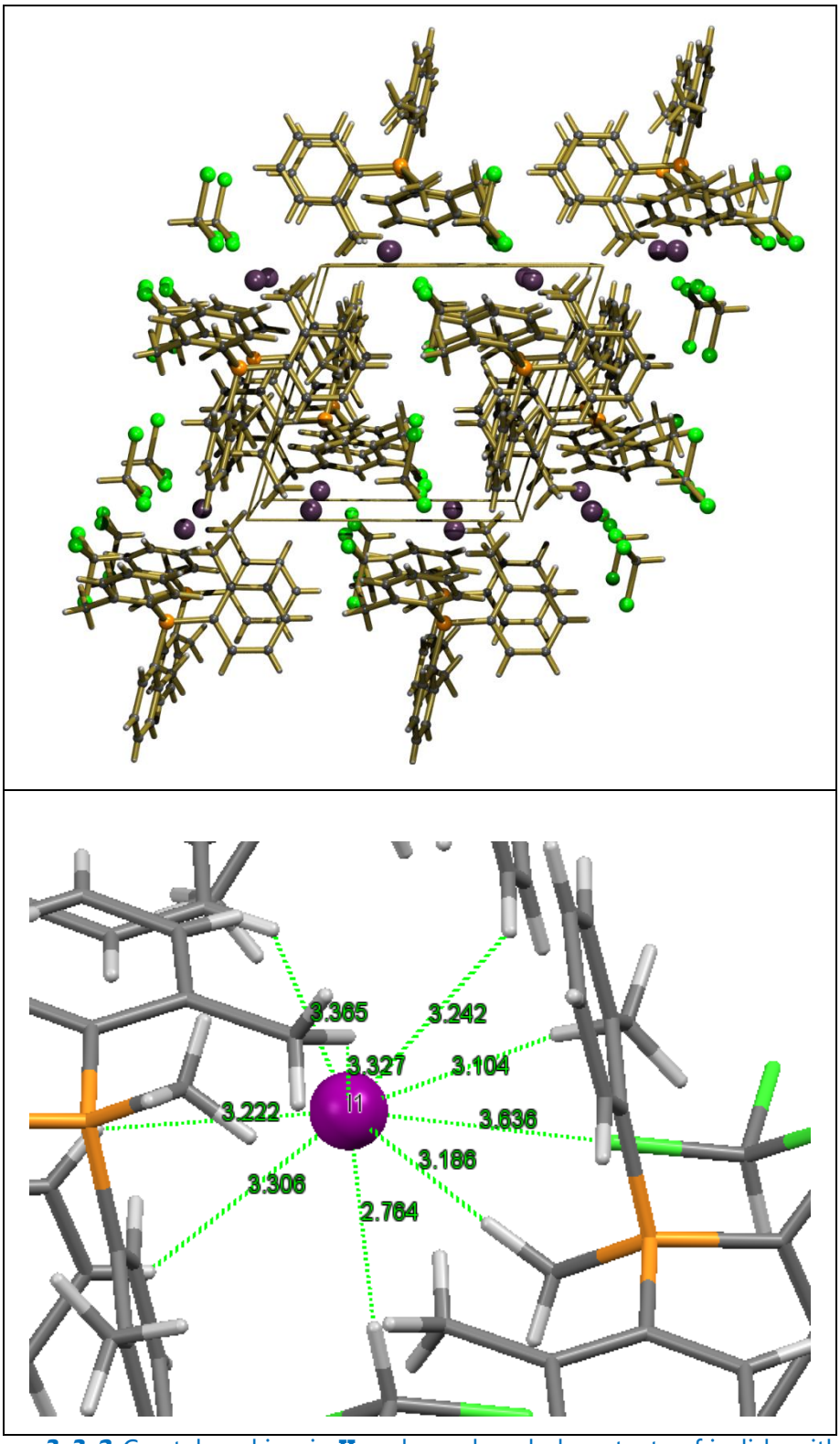

Figure 3-3-2. Crystal packing in **II** and non-bonded contacts of iodide with the chloroform solvate and phosphonium cation.

3-3-1. Experimental

Details of data collection and refinement information are presented in *Table 3-3-3*. All non-hydrogen atoms were refined anisotropically and all hydrogen atoms were constrained to chemically significant locations. The software used in structure I was also used for this structure.

Table 3-3-3. Data collection and refinement information for compound **II**

Data collection	
Diffractometer	KappaCCD diffractometer
Absorption correction	Multi-scan R.H. Blessing, Acta Cryst. (1995), A51, 33-38
T_{min}, T_{max}	0.983, 1.000
No. of measured, independent and observed [$I > 2\sigma(I)$] reflections	9596, 5019, 4129
R_{int}	0.041
$(\sin \theta/\lambda)_{max}$ (Å^{-1})	0.628
Refinement	
$R[F^2 > 2\sigma(F^2)]$, $wR(F^2)$, S	0.042, 0.103, 1.09
No. of reflections	5019
No. of parameters	353
No. of restraints	0
H-atom treatment	All H-atom parameters refined
$\Delta\rho_{max}$, $\Delta\rho_{min}$ (e Å^{-3})	1.27, -1.00

3-3-2. Synthesis

The synthesis of methyltri-o-tolylphosphonium iodide has been described in section 3-2-3.

3-3-3. Crystallisation

0.1g methyltri-o-tolylphosphonium iodide was dissolved in 3 mL chloroform and allowed to stand in a vial covered with a pierced lid to permit slow evaporation. Pale brown crystals appeared in a week.

3-4. Methyltri-o-tolylphosphonium triiodide (III)

The asymmetric unit of **III** is composed of two crystallographically unique methyltri-o-tolylphosphonium cations and two triiodide counterions.

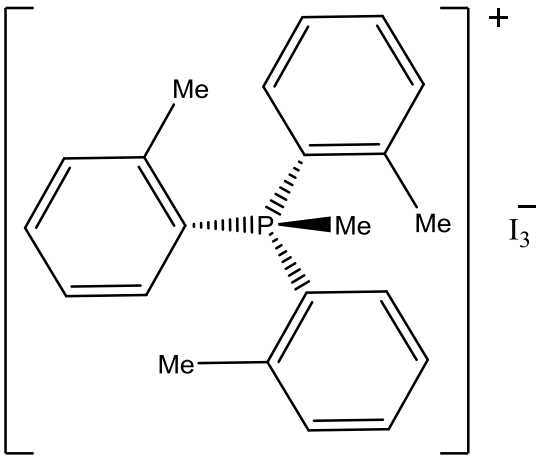

(III)

Scheme 3-1. Illustration of compound **III**

Crystal details are presented in *Table 3-4-1* and the structure is displayed in *Figure 3-4-1* with selected bond lengths and angles in *Table 3-4-2*. The C_{me}-P1-C-C_{me} and C_{me}-P2-C-C_{me} torsion angles of 50.5 (6), 49.3 (6), 51.1 (6) and 50.6 (7), 53.8 (6), 52.6 (6) ° respectively, indicate that the configurations are both exo_3 and that the cation's geometry shows negligible change with changing environment.

Table 3-4-1. Crystal data for structure **III**

Chemical formula	$C_{22}H_{24}P{\cdot}I_3$
M_r	700.08
Crystal system, space group	Triclinic, $P\bar{1}$
Temperature (K)	100
a, *b*, *c* (Å)	10.3943 (2), 13.6346 (2), 18.2615 (4)
α, β, γ (°)	74.8655 (8), 80.6944 (9), 71.8478 (9)
V (Å^3)	2364.83 (8)
Z	4
Radiation type	Mo $K\alpha$
μ (mm^{-1})	4.04
Crystal size (mm)	0.18 × 0.1 × 0.07

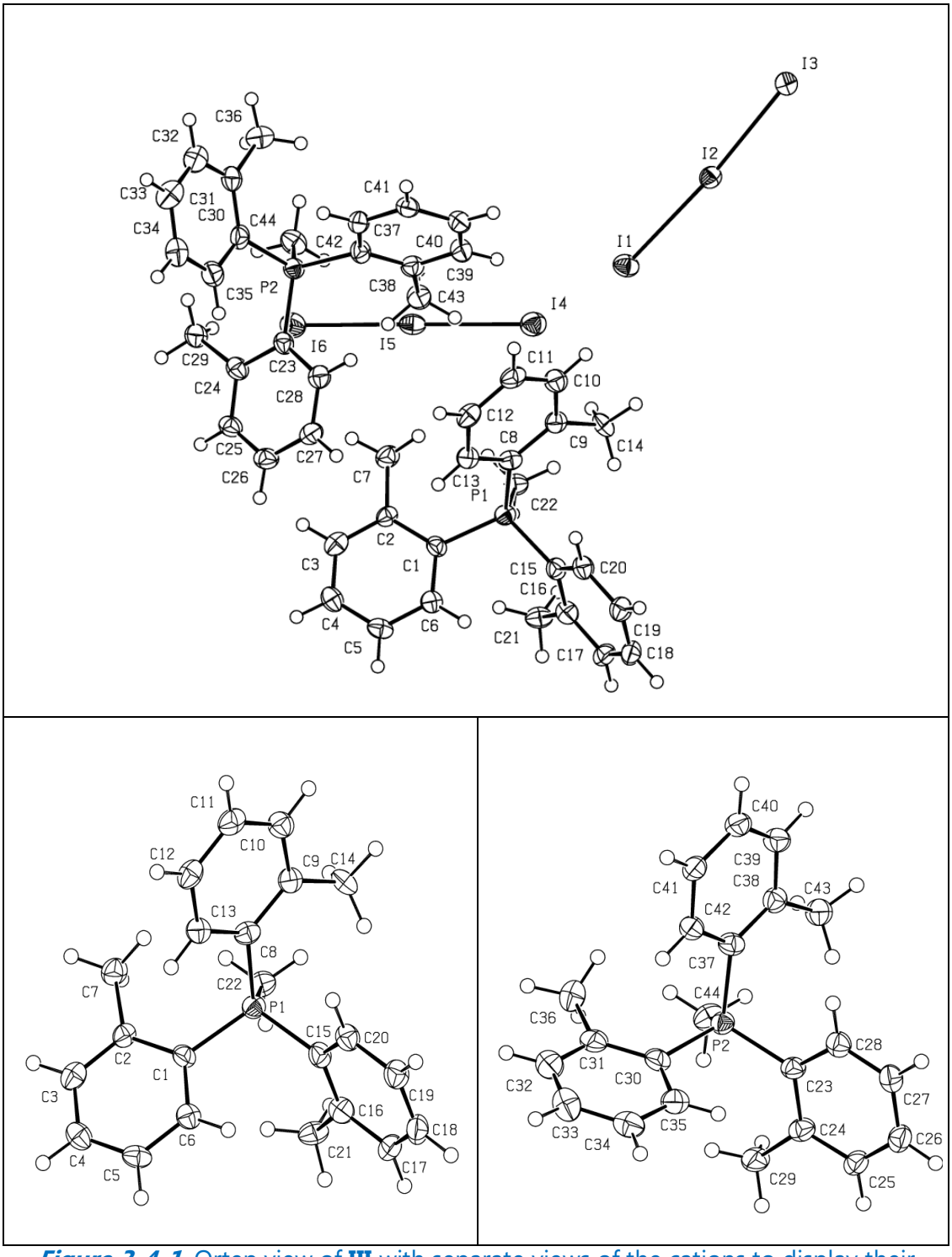

Figure 3-4-1. Ortep view of **III** with separate views of the cations to display their exo$_3$ configurations.

Table 3-4-2. Selected geometric parameters (Å, º) for structure **III**

C1—P1	1.797 (6)	C37—P2	1.813 (6)
C8—P1	1.804 (6)	C44—P2	1.807 (7)
C15—P1	1.800 (6)	I1—I2	2.9222 (6)
C22—P1	1.801 (6)	I2—I3	2.9179 (6)
C23—P2	1.795 (6)	I4—I5	2.9389 (6)
C30—P2	1.812 (7)	I5—I6	2.9018 (6)
I3—I2—I1	172.711 (19)	C22—P1—C8	109.0 (3)
I6—I5—I4	178.98 (2)	C23—P2—C44	110.0 (3)
C1—P1—C22	109.8 (3)	C44—P2—C30	113.3 (3)
C15—P1—C22	111.2 (3)	C44—P2—C37	109.3 (3)
C2—C1—P1—C22	-50.9 (6)	C24—C23—P2—C44	-52.8 (6)
C16—C15—P1—C22	-50.8 (6)	C31—C30—P2—C44	-50.5 (6)
C9—C8—P1—C22	-49.3 (6)	C38—C37—P2—C44	-53.7 (6)

The triiodide anions show small but significant asymmetry of their I-I bonds (I1-I2 2.9013 (7), I2-I3 2.9391 (7) and I4-I5 2.9223 (5) and I5-I6 2.9180 (5) Å). This is typical of triiodide anions, as is the deviation from linearity, I3-I2-I1=172.711 (19) and I6-I5-I4=178.98 (2) °. Some deformation would be anticipated from Jahn Teller effects but, as the triiodide is known to be susceptible to crystal packing forces and many examples of the anion showing significantly higher asymmetry than observed here can be found

in the literature, this is likely to be the explanation. The crystal packing of **III** along with the crystal environment of each triiodide are displayed in *Figure* 3-4-2. Although the packing diagram hints at contact between the triiodide anions in channels running through the crystal, only hydrogen atoms interact with iodine atoms at VDW distances or less. In fact the closest approach of two triiodide anions is a side-on approach, which brings terminal I6 within 4.373(8) Å of central I2. It is noteworthy that a consequence of I2 being repelled by I6 would be the bend seen in triiodide I1-I2-I3.

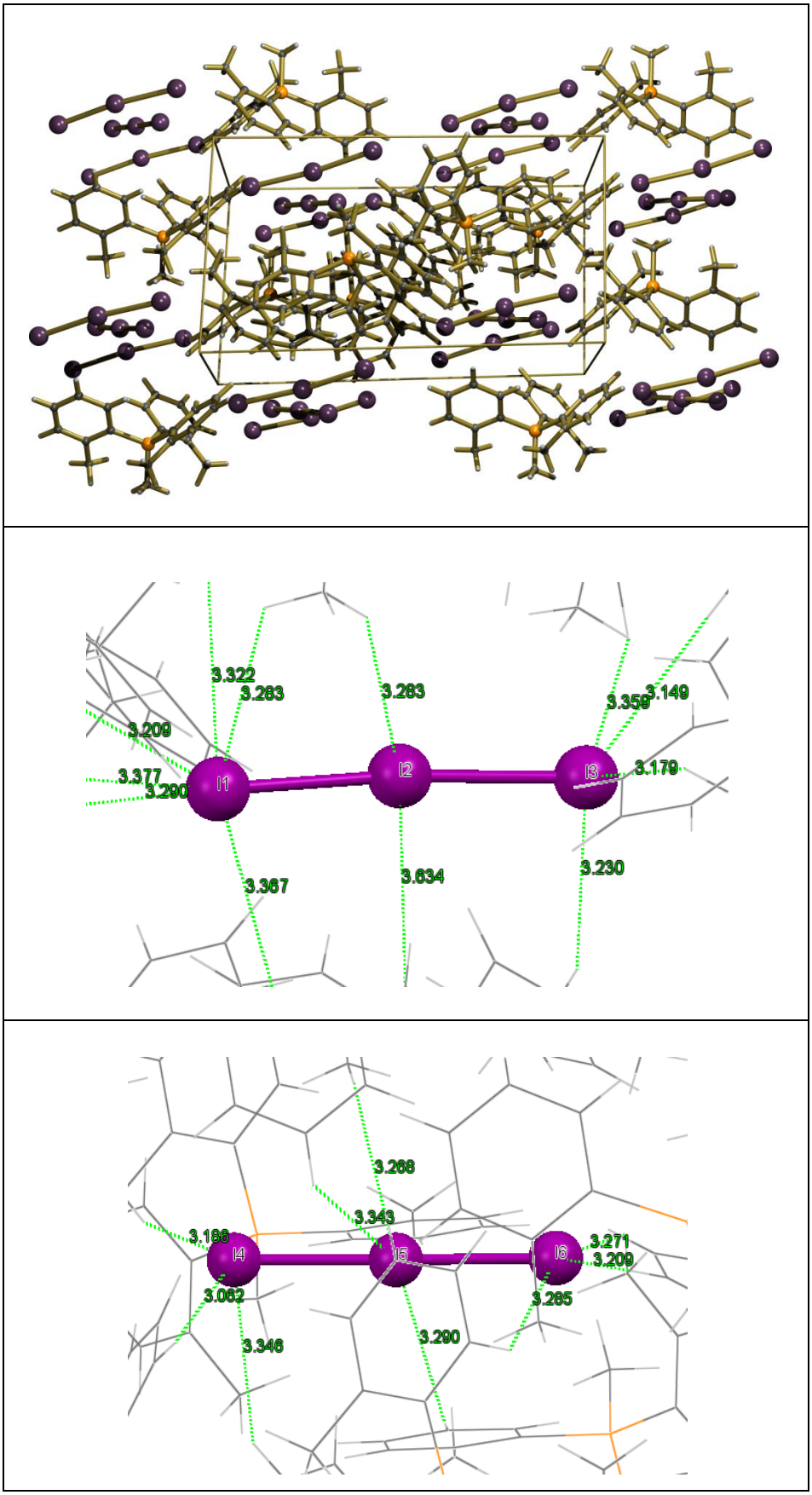

Figure 3-4-2. Crystal packing and I_3^- environments in **III**

Despite the H…I and I…I being weak or absent a significant π-π interaction is again seen in adjacent cations *(Fig. 3-4-3).*

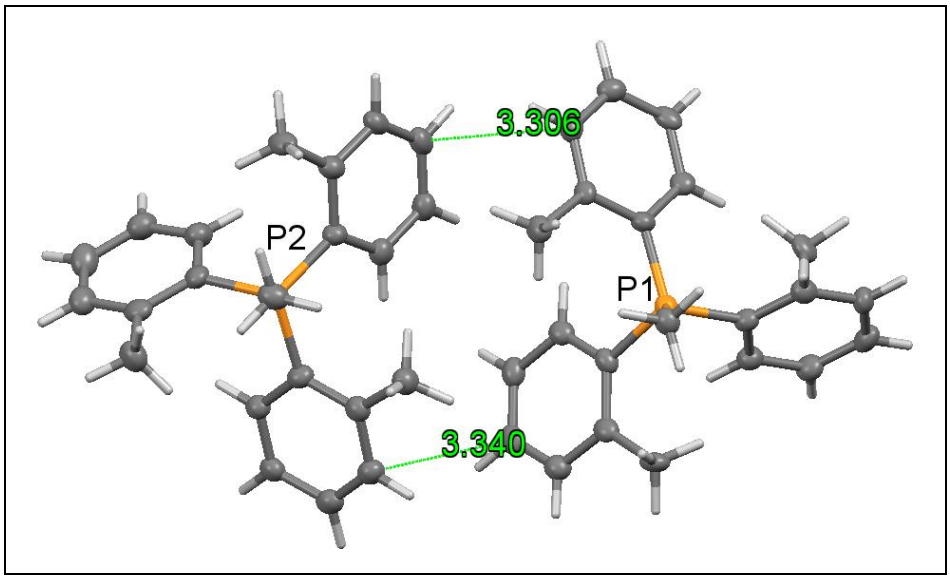

Figure 3-4-3. π-π stacking between the two crystallographically unique cations in structure **III**

3-4-1. Experimental

All non-hydrogen atoms were refined anisotropically via full matrix least squares methods and hydrogen atoms were constrained to chemically reasonable positions. Software and instrumentation were as described for structure **I**.

Table 3-4-3. Data collection and refinement details for **III**

Data collection	
Diffractometer	KappaCCD diffractometer
Absorption correction	Multi-scan R.H. Blessing, Acta Cryst. (1995), A51, 33-38
T_{min}, T_{max}	0.530, 0.765
No. of measured, independent and observed [$I > 2\sigma(I)$] reflections	48562, 9256, 7883
R_{int}	0.076
$(\sin\theta/\lambda)_{max}$ (Å^{-1})	0.617
Refinement	
$R[F^2 > 2\sigma(F^2)]$, $wR(F^2)$, S	0.045, 0.125, 1.04
No. of reflections	9256
No. of parameters	475
No. of restraints	0
H-atom treatment	H-atom parameters constrained
	$w = 1/[\sigma^2(F_o^2) + (0.068P)^2 + 12.6244P]$ where $P = (F_o^2 + 2F_c^2)/3$
$\Delta\rho_{max}$, $\Delta\rho_{min}$ (e Å^{-3})	1.15, -2.07

3-4-2. Synthesis

0.1 g of the previously prepared methyltri-o-tolylphosphonium iodide (See section 3-1) was dissolved in 3 mL dichloromethane and five drops of 0.1 M iodine, also in dichloromethane, added. The resulting solution was allowed to slowly evaporate in a sample container covered with a pierced lid. Brown crystals with the following microanalysis were recovered after 4 days.

Microanalysis of the brown solid $[(o\text{-tolyl})_3PMe][I_3]$ calculated for $C_{22}H_{24}PI_3$: C, 37.7; H, 3.4; I, 54.4; Found: C, 37.5; H, 3.5; I, 54.8

3-5. Bis(methyltri-o-tolylphosphonium) octaiodide (IV)

Crystal details for **IV** are provided in *Table 3-5-1*. An Ortep view of the molecule is presented in *Figure 3-5-1* and selected bond lengths and angles in *Table 3-5-2*. In bis(methyltri-o-tolylphosphonium) octaiodide (IV), the planar 'Z'-shaped I_8^{-2} dianion is located on a crystallographic inversion centre.

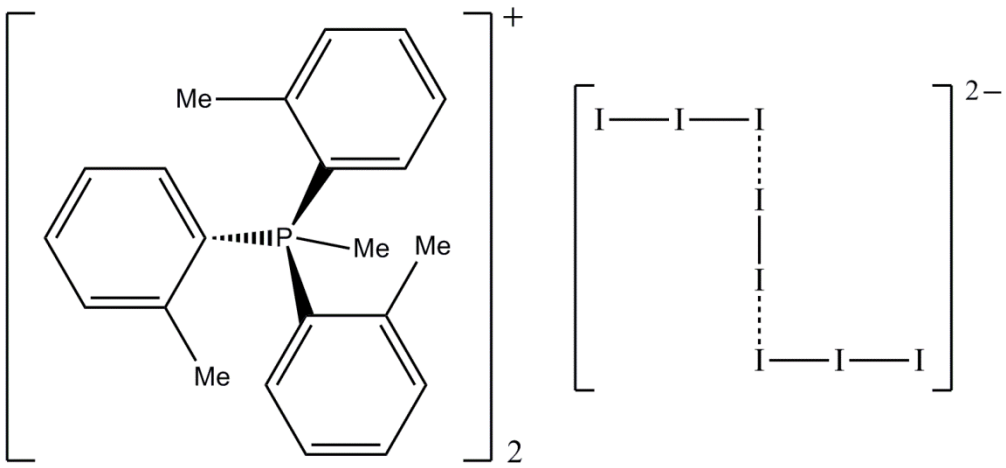

(IV)

Scheme 1. Illustration of the compound **IV**

Table 3-5-1 Crystallographic information for molecule **IV**, 2([tri-o-tolylphosphonium-methyl]$^{+}$) I^{-}

Chemical formula	$2C_{22}H_{24}P^{+}\cdot I_8^{2-}$
M_r	1653.96
Crystal system, space group	Triclinic, $P\bar{1}$
Temperature (K)	100
a, *b*, *c* (Å)	9.6680 (2), 12.3567 (3), 12.8186 (4)
α, β, γ (°)	62.364 (1), 76.410 (1), 73.073 (1)
V (Å^3)	1288.83 (6)
Z	1
Radiation type	Mo *K*α
μ (mm^{-1})	4.90
Crystal size (mm)	0.15 × 0.1 × 0.1

Table 3-5-2. Selected geometric parameters (Å, º) for **IV**.

C1—P1	1.800 (12)	I1—I2	3.0162 (11)
C8—P1	1.806 (11)	I2—I3	2.8511 (11)
C15—P1	1.825 (12)	I4—I4^{i}	2.7663 (17)
C22—P1	1.808 (13)		
I3—I2—I1	174.42 (4)	C1—P1—C15	109.4 (5)
C1—P1—C22	109.8 (6)	C22—P1—C15	109.8 (6)
C1—P1—C8	108.7 (5)	C8—P1—C15	108.7 (5)
C22—P1—C8	110.4 (5)		
C2—C1—P1—C22	-54.0 (11)	C16—C15—P1—C22	-48.2 (11)
C9—C8—P1—C22	-51.3 (11)		

Symmetry code: (i) -x+1, -y, -z+1.

The octaiodide dianion is a member of the dianionic polyiodide series $(I_{2n+2})^{2-}$, whose first three members would be expected to consist of a di-iodine combined, respectively, with two iodide anions, an iodide and tri-iodide, and two tri-iodide anions. The tetra-iodide is the most frequently encountered polyiodide in the $(I_{2n+2})^{2-}$ series and in all cases the I_4^{2-} anion is linear. No intermolecular I· · ·I contacts less than 4 Å have been observed in these compounds (Kloo & Svensson, 2003).

To date no structure containing an undisordered I_6^{2-} anion has been reported. It is therefore somewhat surprising that several I_8^{2-} containing structures are known. The first I_8^{2-} ion was determined by Havinga et al. (1954) in Cs_2I_8. Generally, an I_8^{2-} ion consists of two I_3^- ions that interact with an I_2 molecule to form 'Z'-shaped $[(I_3^-)_2(I_2)]$. This geometry, which includes out-stretched ('S'-shaped) or slightly deformed forms, is the predominating geometry for all structurally characterized octaiodide dianions.

The bonding distances in the octaiodide indicate that it is made up of two tri-iodide anions and a di-iodine molecule *(Table 3-6-1).* Although the 'Z' angle is 81° in the inorganic salt Cs_2I_8, the 'Z' angle of 89.92 (4)° in the current structure is the most acute seen in structures containing organic cations. In the title molecule, the I_8^{2-} 'Z' is completely flat, with the two I_3^- units configured trans to one another. In other words, the torsion angle defined by the angle between the two I_3^- ions when projected down the I_2 bond

is 180°, as required by the centre of inversion that relates them. This is the configuration seen in all known I_8^{2-} ions except in the salts with the tris(1,10-phenanthroline)iron(II) complex (-82.1°; Horn et al., 2001) and the dihydrogen [2.2.2]cryptand (-99.3°; Grafe-Kavoosian et al., 1998). It is interesting that the central torsion angle is either 180° or close to 90°.

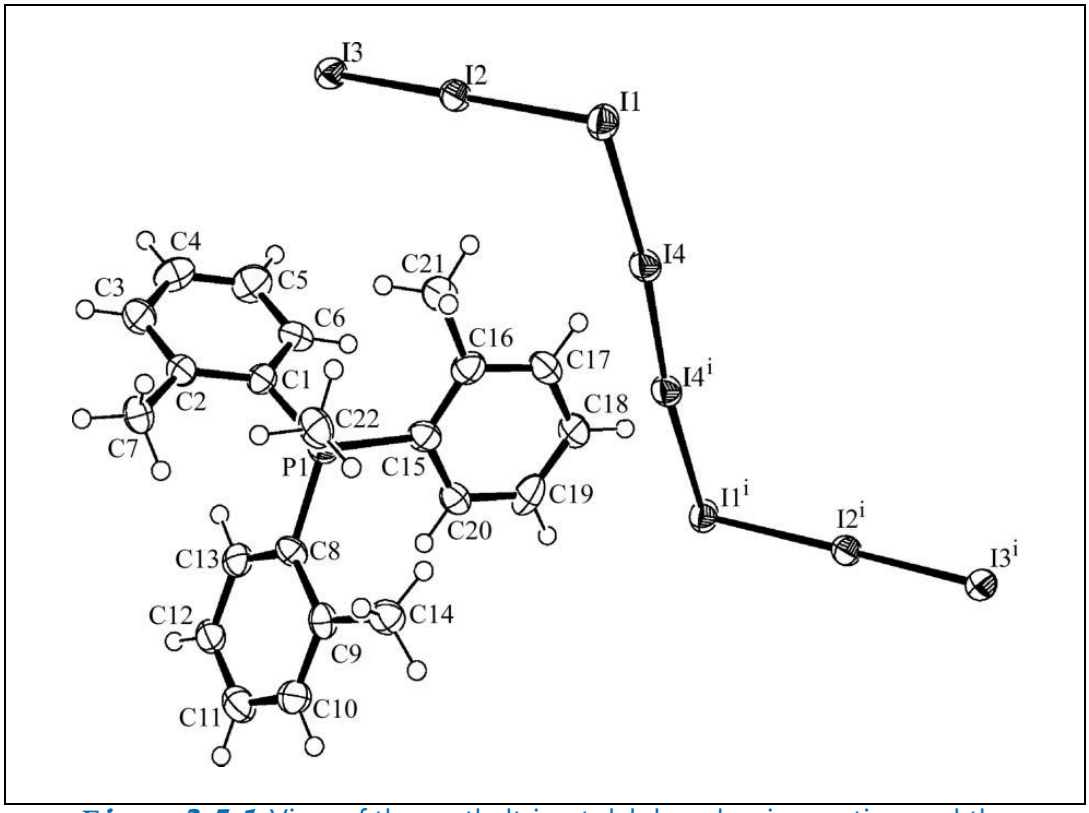

Figure 3-5-1. View of the methyltri-o-tolylphosphonium cation and the centrosymmetric octaiodide dianion of **IV**, including the atom-labelling scheme. [Symmetry code: (i) -x + 1, -y, -z + 1.]

Each I_8^{2-} anion in the present structure associates with two adjacent anions via long contacts of 3.977 (1) Å to form infinite polyiodide ribbons along [100] *(Figure 3-5-2).* Interestingly, this is the first example where the long-range interactions between I_8^{2-}

ions involve both the I_3^- and I_2 moieties. In all other cases where interionic interactions occur between I_8^{2-} units, only the I_3^- ions are involved. When only one iodine in each I_3^- ion takes part in long-range interactions, a helical (Horn et al., 2001) or branched (Kuhn et al., 2000) chain is produced. When both terminal I_3^- iodines are employed, puckered sheets result (Grafe-Kavoosian et al., 1998; Kuz'mina et al., 2000). Although the number of long-range I· · ·I interactions are the same in the title structure as they are in the puckered sheets, involvement of the central I_2 gives lower conformational freedom, leading to flat ribbons.

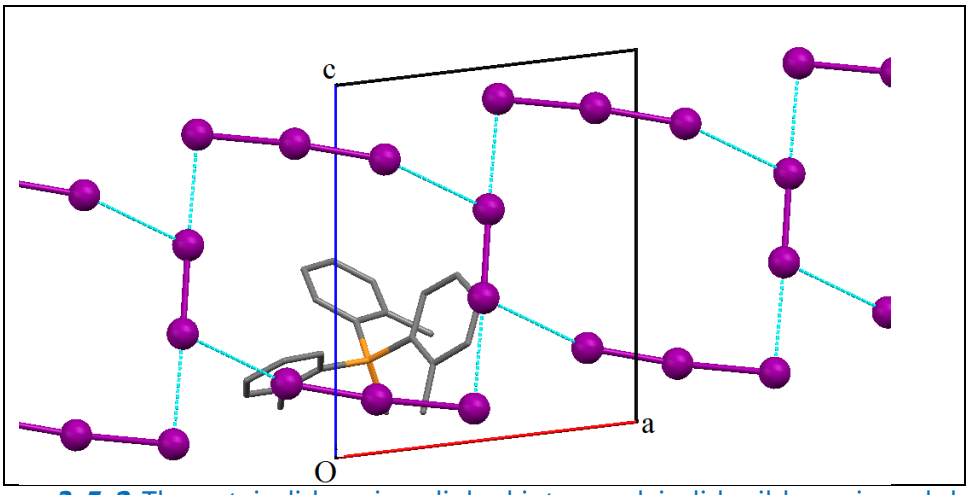

Figure 3-5-2. The octaiodide anions linked into a polyiodide ribbon viewed down the crystallographic **b** axis.

No significant iodide interactions take place between ribbons; the closest inter-ribbon I···I approach, at 5.372Å, is much further than the Van der Waals distances.

The C_{Me}—P—C—C_{Me} torsion-angle values of C22—P1—C1—C2 =

-54.0 (11)°, C22—P1—C8—C9 = -51.3 (11)° and C22—P1—C15—C16 = -48.2 (11)° confirm that the configuration is exo_3

3-5-1. Experimental

Details of data collection and refinement are presented in Table 3-5-3. All non-hydrogen atoms were refined anisotropically. H atoms were constrained to chemically reasonable positions, with C—H bond lengths set at 0.95 A˚ for phenyl and at 0.98 A˚ for methyl groups. Uiso(H) values were set at 1.2 times the Ueq values of the attached C atoms in phenyl rings and at 1.5 times the Ueq values for methyl H atoms. The largest peaks remaining in the difference map have electron densities of 4.7 and 3.6 e A˚-3. They are arranged linearly on either side of I42- at distances of 2.924 and 2.964 A˚ , forming an I3- shape. No credible twin model was found, and no indication of spot splitting could be seen in the X-ray images. It was therefore concluded that the best explanation for the residual electron density was a minor secondary phase that had intergrown with the primary structure.

Table 3-5-3. Details of data collection and structure refinement for **IV**

Data collection	
Diffractometer	Nonius KappaCCD diffractometer
Absorption correction	Multi-scan (Blessing, 1995)
T_{min}, T_{max}	0.527, 0.640
No. of measured, independent and observed [$I > 2\sigma(I)$] reflections	4776, 4776, 3762
R_{int}	0
$(\sin\theta/\lambda)_{max}$ (Å^{-1})	0.606
Refinement	
$R[F^2 > 2\sigma(F^2)]$, $wR(F^2)$, S	0.069, 0.183, 1.15
No. of reflections	4776
No. of parameters	247
No. of restraints	0
H-atom treatment	H-atom parameters constrained
	$w = 1/[\sigma^2(F_o^2) + (0.0697P)^2 + 33.6613P]$ where $P = (F_o^2 + 2F_c^2)/3$
$\Delta\rangle_{max}$, $\Delta\rangle_{min}$ (e Å^{-3})	4.64, -2.84

3-5-2. Synthesis

0.1 g of the previously prepared methyltri-o-tolylphosphonium iodide (See section 3-2-2) was dissolved in 3 mL dichloromethane and eight drops of 0.1 M iodine, also in dichloromethane, added. The resulting solution was allowed to slowly evaporate in a sample container covered with a pierced lid. Dark red crystals were recovered after 4 days.

3-6. Methyltri-o-tolylphosphonium hexaiodide (V)

These crystals had the highest iodine loading in the methyltri-o-tolylphosphonium series but they only diffracted up to 2θ = 40° and their X-ray analysis proved extremely challenging (see section 3-6-1). They tended to loose iodine and it was shown using powder XRD that they converted to the octaiodide (**IV**) on standing in an uncovered container. Crystal details are provided in *Table 6-3-1* and selected bond lengths and angles in *Table 6-3-2*. The structure contains two crystallographically unique methyltri-o-tolylphosphonium cations *(Figure 6-3-1)* but, as each possesses crystallographic C_3 symmetry, the asymmetric unit is composed of a total of 2/3 of a phosphonium cation and four iodine/iodide atoms distributed over several partially occupied sites.

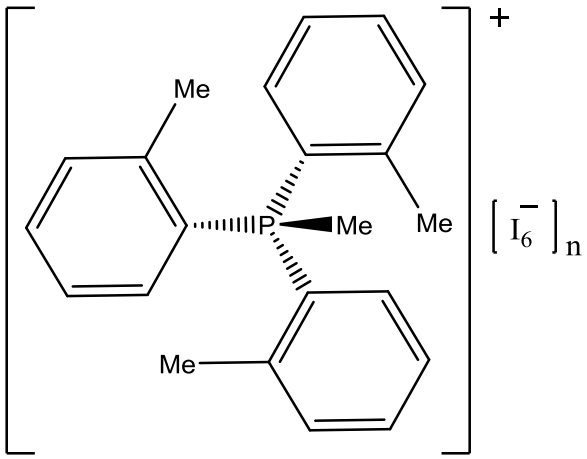

(V)

Scheme 1. Illustration of the compound **V**

Table 3-6-1. Crystal data for **V**

Chemical formula	$C_{22}H_{24}I_6P$
M_r	1080.78
Crystal system, space group	Hexagonal, $P\bar{6}2c$
Temperature (K)	100
a, c (Å)	13.9139 (4), 36.866 (2)
V (Å^3)	6181.0 (4)
Z	8
Radiation type	Mo $K\alpha$
μ (mm^{-1})	6.09
Crystal size (mm)	0.15 × 0.1 × 0.08

Table 3-6-2. Selected geometric parameters (Å, º) for **V**

P1—C8	1.755 (3)	P11—C18	1.762 (5)
P1—C1	1.784 (3)	P11—C11	1.7967
C8—P1—C1	109.36 (17)	C18—P11—C11	109.6
C8-P1-C1-C2	50.1(2)	C18-P11-C11-C12	49.1

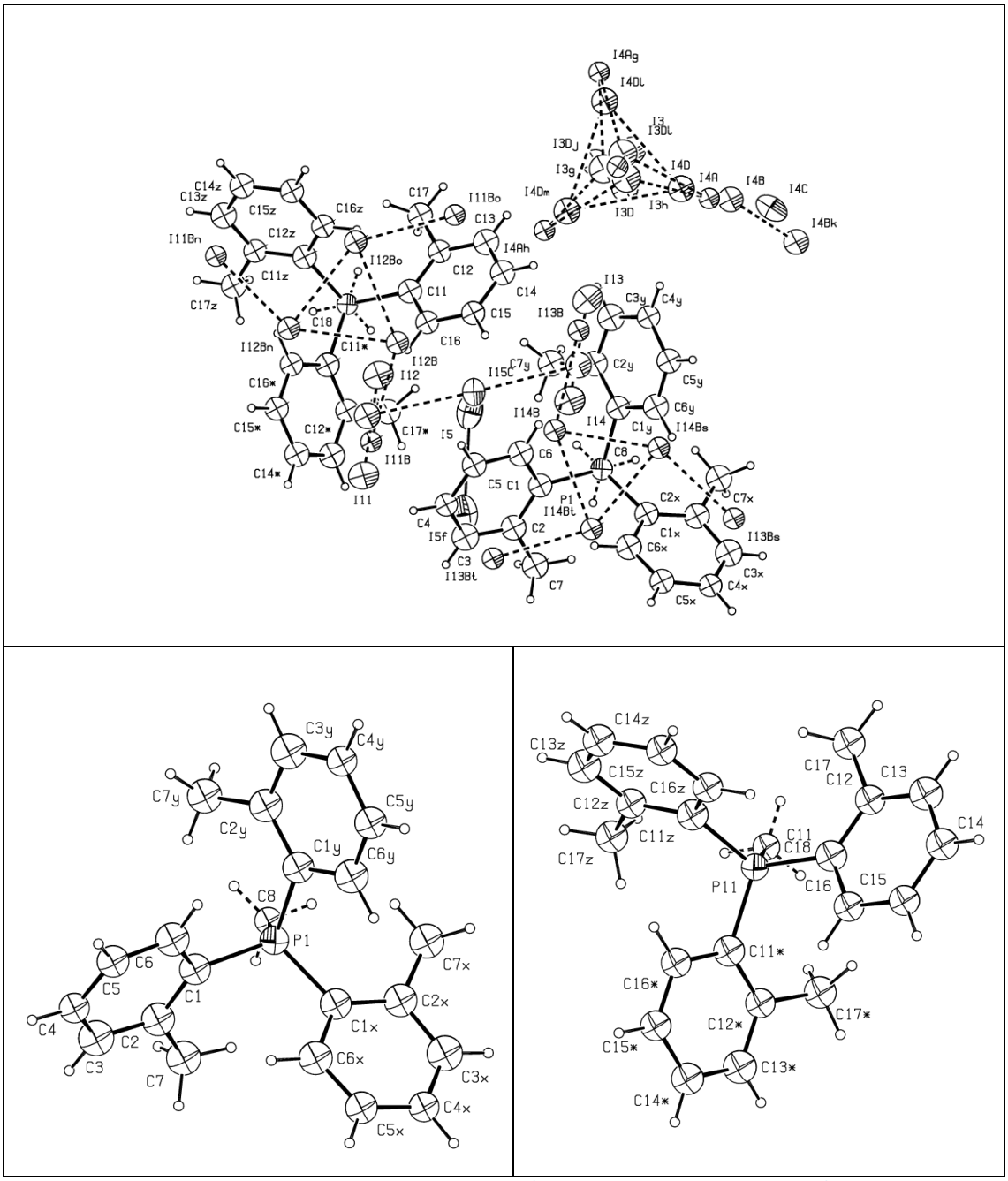

Figure 3-6-1. A labelled ORTEP view of **V** and individual viwes of the two crystallographically independent cations, which each have crystallographic C_3 symmetry.

The exo_3 configuration is retained in **V** and, within experimental error the geometry seen in structures **I – IV** is conserved. Also, as before, the cations associate via π-π interactions, packing into a hexagonal layer parallel to the crystallographic ab plane in this case *(Figure 3-6-2).* Interestingly all the methyl groups project exclusively from one side of the plane with the other side of the plane being composed entirely of phenyl rings. This has an interesting consequence for the polyiodide intercalate *(Figure 3-6-3).* The iodine that is in contact with the methyl side of the plane follows the contours of the surface, whilst, in contrast, the iodine that's in contact with the phenyl rings is completely flat. The two polyiodide zones are distinct with no short I…I contacts between the zones, however there are sixteen crystallographically distinct I…I contacts in the range 2.552 (3) to 3.115 (6) Å in the planar polyiodide layer with eleven I…I contacts in the range 2.076 (4) to 3.084 (11) Å in the undulating layer. See *Figure 3-6-4* for chemically sensible I…I contacts within the planar iodine layer. The H…I contacts are still present but they are now only a small proportion of the total I interactions.

Table 3-6-3. I..I contacts in compound **V** (Å)

I1—I2	2.8972 (15)	I12—I12B^{v}	2.676 (5)
I3—I4A^{i}	2.706 (4)	I13—I14	2.727 (3)
I3—I4A	2.973 (3)	I14—I15C	2.552 (3)
I4A—I4B^{iii}	2.959 (2)	I14—I14B^{vi}	2.673 (5)
I4B—I3D	2.888 (12)	I11B—I12B	2.719 (6)
I4B—I3D^{i}	2.985 (16)	I11B—I15C	3.023 (4)
I4C—I4D	2.881 (7)	I12B—I12B^{v}	2.904 (6)
I4D—I3C	3.006 (8)	I12B—I16C^{vii}	3.115 (6)
I4D—I4D^{i}	3.084 (11)	I13B—I14B	2.727 (6)
I5—I5^{iv}	2.721 (2)	I14B—I14^{viii}	2.673 (4)
I3C—I3D^{i}	2.865 (15)	I14B—I14B^{vi}	2.795 (6)
I3C—I4D^{ii}	3.006 (8)	I14B—I17C^{viii}	3.056 (6)
I11—I12	2.694 (3)	I15C—I17C	2.866 (4)
I12—I15C	2.567 (3)	I15C—I16C	2.890 (4)

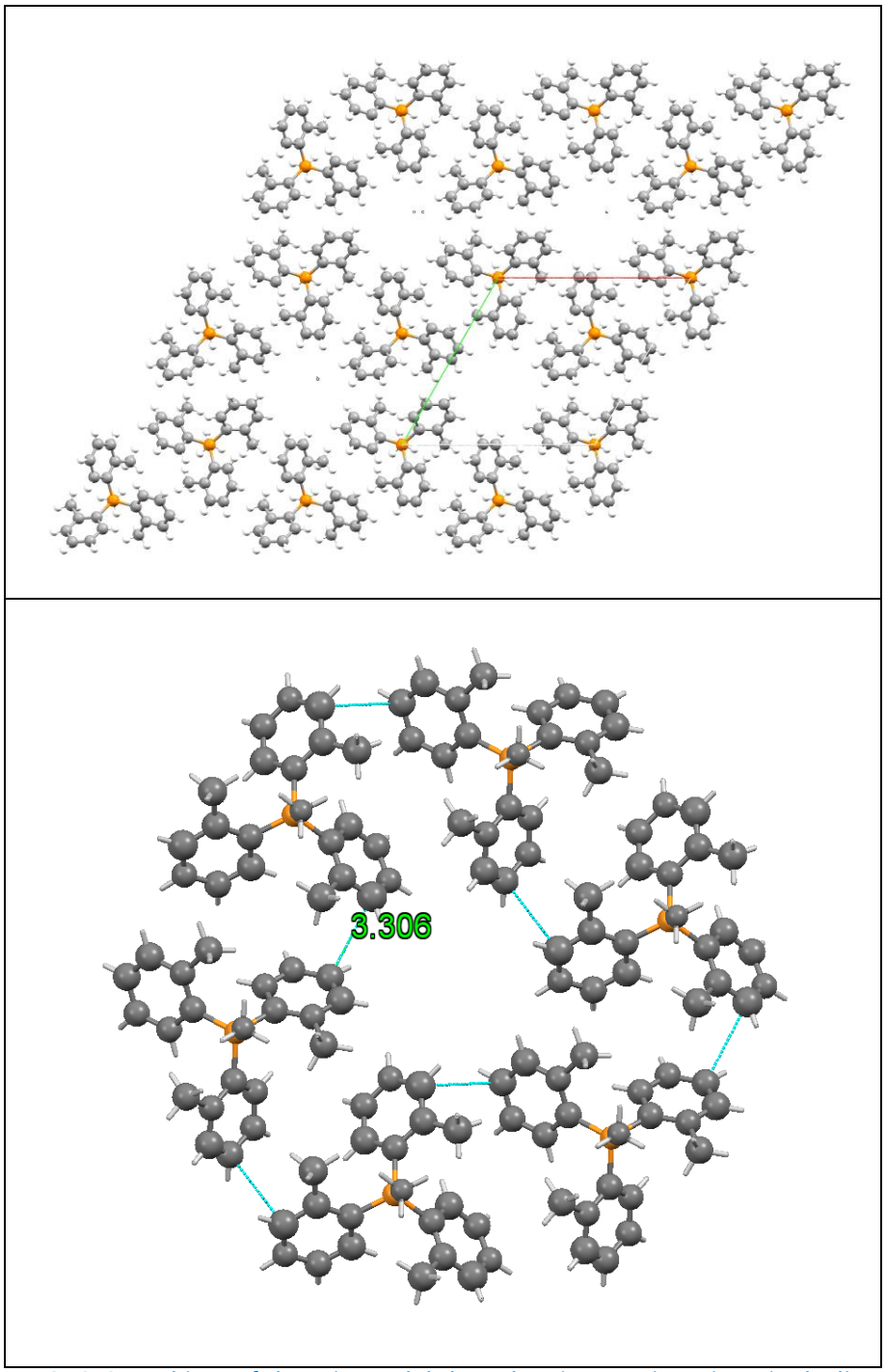

Figure 3-6-2. Packing of the tri-o-tolylphosphonium cations in **V** including π-π contacts (Å)

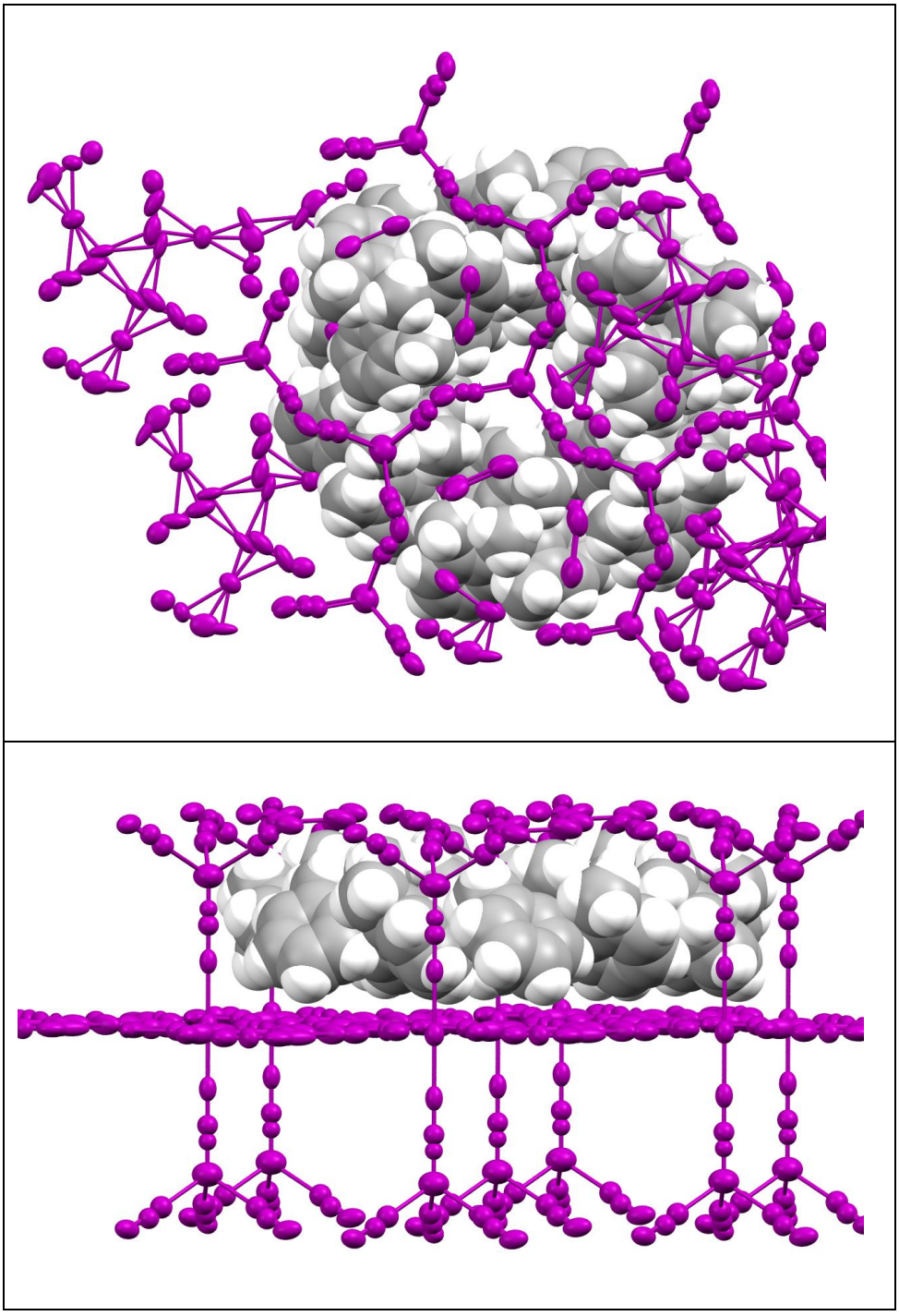

Figure 3-6-3. Packing in **V** viewed down the crystallographic c axis (Top) and perpendicular to the c axis (Bottom)

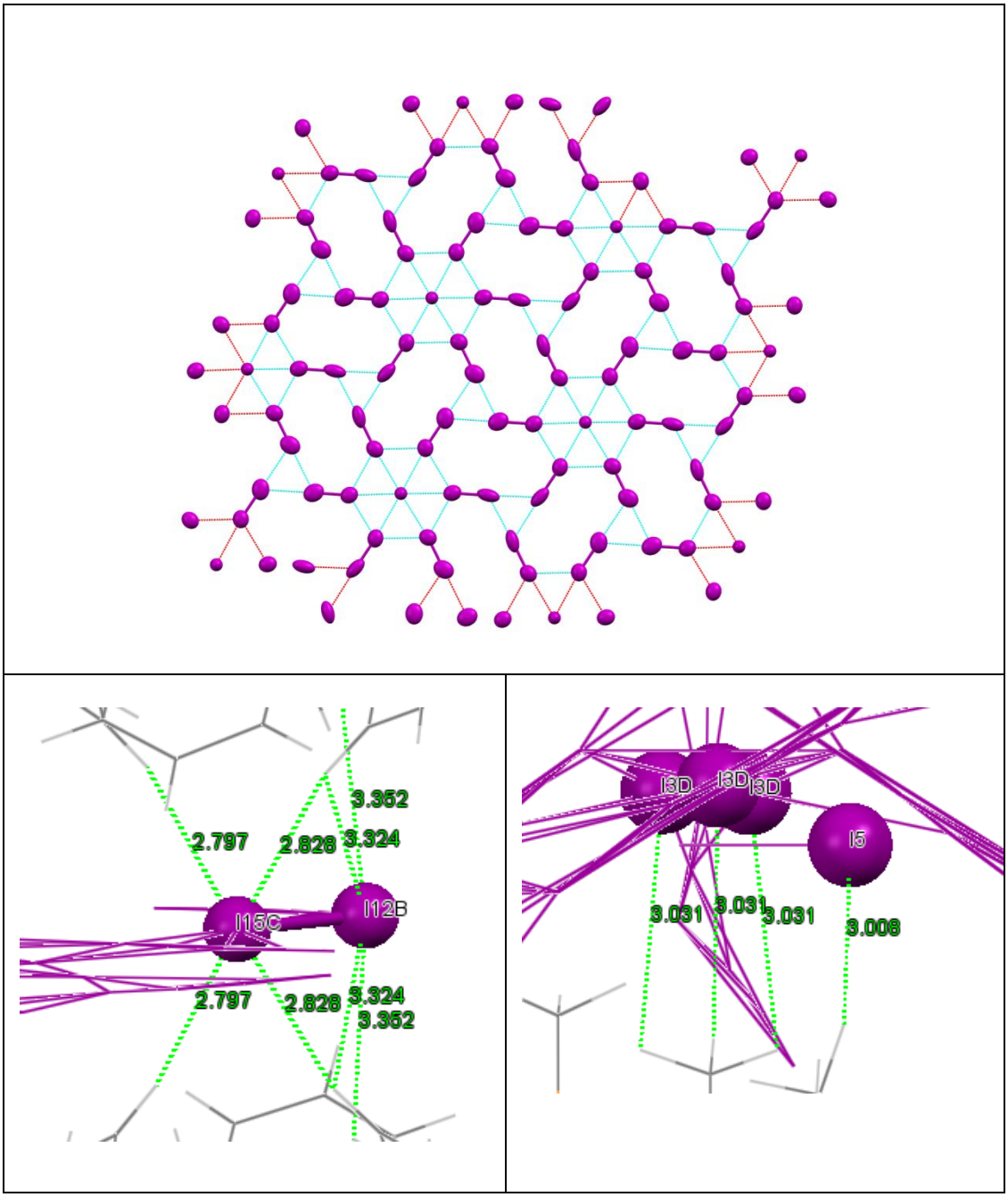

Figure 3-6-4. Iodine interactions in **V**. Possible short I…I contacts in the planar polyiodide layer (Top). H…I contacts between phenyl H and planar iodine layer (Bottom left) and between methyl H and undulating iodine layer (Bottom right)

3-6-1. Experimental

The same procedures and software that were used on the previous structures were used here except structure solution required the charge-flipping software of Platinus and Chapius

(2007). Anisotropic refinement could only be carried out on the P and I atoms. Also because the disordered iodine and limited data made the refinement unstable and damping was left on, even in the final refinement. Hydrogen atoms were constrained to chemically reasonable positions.

Table 3-6-4. Details of data collection and structure refinement for **V**

Data collection	
Diffractometer	KappaCCD diffractometer
Absorption correction	Multi-scan Blessing, R. H. (1995) Acta Cryst., A51, 33-38.
T_{min}, T_{max}	0.462, 0.642
No. of measured, independent and observed [$I > 2\sigma(I)$] reflections	9355, 1960, 1311
R_{int}	0.128
θ_{max} (°)	20.0
$(\sin\theta/\lambda)_{max}$ (Å^{-1})	0.481
Refinement	
$R[F^2 > 2\sigma(F^2)]$, $wR(F^2)$, S	0.086, 0.241, 1.37
No. of reflections	1960
No. of parameters	157
No. of restraints	26
H-atom treatment	H-atom parameters constrained
	$w = 1/[\sigma^2(F_o^2) + (0.0823P)^2 + 31.8691P]$ where $P = (F_o^2 + 2F_c^2)/3$
$\Delta\rangle_{max}$, $\Delta\rangle_{min}$ (e Å^{-3})	1.31, -0.63
Absolute structure	Flack H D (1983), Acta Cryst. A39, 876-881
Absolute structure parameter	0.43 (5)

3-6-2. Synthesis

0.1 g of the previously prepared methyltri-o-tolylphosphonium iodide (See section 3-2-2) was dissolved in 3 mL dichloromethane and twenty drops of 0.1 M iodine, also in dichloromethane, added. The resulting solution was allowed to slowly evaporate in a sample container covered with a pierced lid. Black crystals were recovered after 4 days.

3-7. Hydrogen bis[tris(4-fluorophenyl)-phosphine oxide] triiodide (VI)

In **VI**, $C_{36}H_{25}F_6O_2P_2^+ \cdot I_3^-$, hydrogen-bonded $[\{(p\text{-}FC_6H_4)_3PO\}_2H]^+$ dimers assemble along the crystallographic *c* axis to form channels that house extended chains of triiodide anions. Although the I—I bond lengths of 2.9452 (14) and 2.9023 (15) Å are typical, the inter-ion I···I distance of 3.5774 (10) Å is unusually short. A posteriori modelling of nonmerohedral twinning about (100) has been only partially successful, achieving a reduction in the maximum residual electron density from 5.28 to 3.24 e $Å^{-3}$. The inclusion of two low-occupancy I-atom sites (total 1.7%), which can be interpreted as translational disorder of the triiodide anions along the channels, reduced the maximum residual electron density to 2.03 e $Å^{-3}$. The minor fractional contribution volume of the nonmerohedral twin domains refined to 0.24 and simultaneous refinement of the inversion twin domains showed the crystal to be a 0.5:0.5 inversion twin.

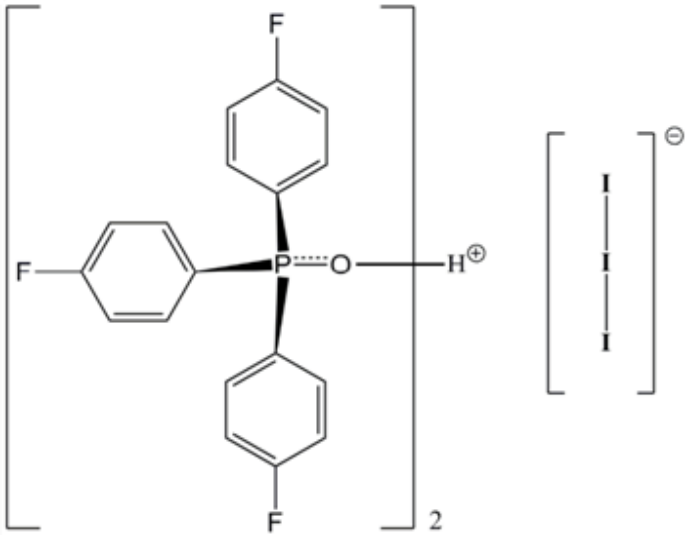

(**VI**)

Scheme 1. Illustration of the compound **VI**

VI, consists of triiodide anions and H^+ counter-ions that link pairs of tris(4-fluorophenyl) phosphine oxide entities into hydrogen-bonded dimers *(Figure. 3-7-1)*.

Table 3-7-1. Crystal data for **VI**

Crystal data	
Chemical formula	$C_{36}H_{25}F_6O_2P_2^+ \cdot I_3^-$
M_r	1046
Crystal system, space group	Monoclinic, *Cc*
Temperature (K)	100
a, *b*, *c* (Å)	13.2153 (4), 15.9752 (6), 18.5695 (6)
α (°)	108.818 (2)
V (Å^3)	3710.8 (2)
Z	4
Radiation type	Mo *K*α
μ (mm^{-1})	2.68
Crystal size (mm)	0.18 × 0.15 × 0.06

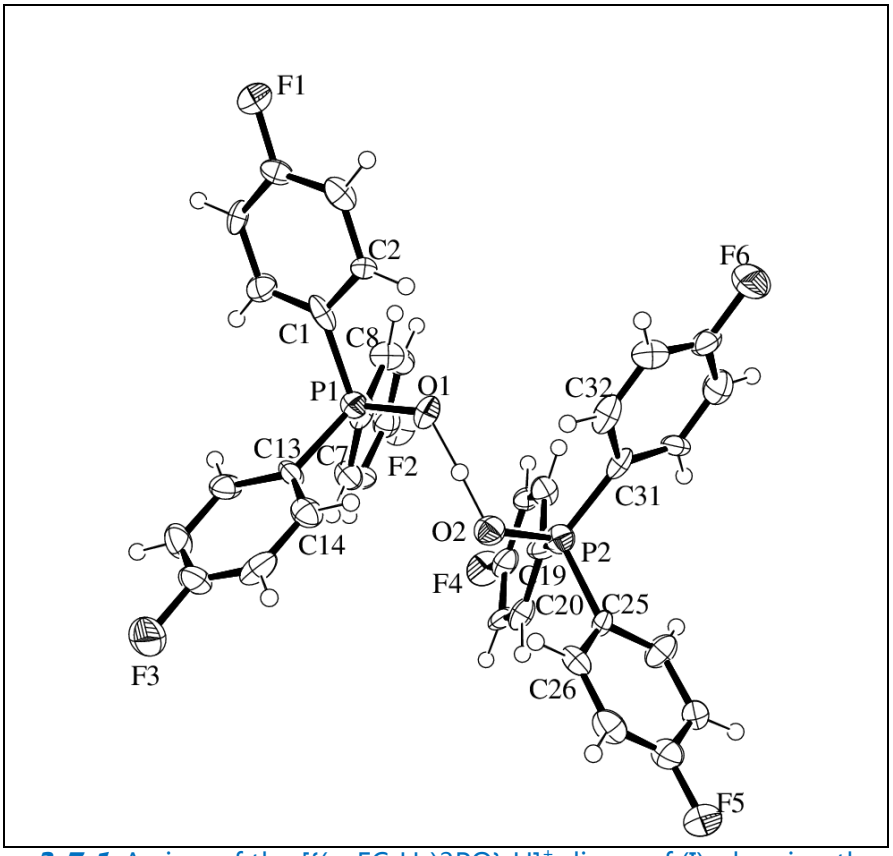

Figure 3-7-1. A view of the $[\{(p\text{-}FC_6H_3)3PO\}_2H]^+$ dimer of (I), showing the atom labelling scheme.

The two crystallographically unique $(p\text{-}FC_6H_4)_3PO$ molecules have similar conformations, as indicated by their O—P—C—C torsion angles of 3.9 (11), 78.0 (12) and -13.7 (13)° involving O1—P1, and of 80.2 (12), 10.1 (13) and -15.5 (12)° involving O2—P2 *(Table 3-7-2).*

Table 3-7-2. Selected geometric parameters (Å, º) for **VI.**

C1—P1	1.811 (15)	O1—P1	1.526 (10)
C7—P1	1.783 (13)	O2—P2	1.530 (10)
C13—P1	1.799 (12)	I1—I3	2.9023 (15)
C19—P2	1.740 (15)	I1—I2	2.9452 (14)
C25—P2	1.799 (14)	I2—I3^{i}	3.5774 (11)
C31—P2	1.797 (14)		
O1—P1—C7	112.9 (6)	O2—P2—C19	112.4 (6)
O1—P1—C13	109.4 (6)	O2—P2—C31	110.5 (5)
O1—P1—C1	107.4 (6)	O2—P2—C25	107.0 (6)
C8—C7—P1—O1	78.0 (12)	C20—C19—P2—O2	80.2 (12)
C14—C13—P1—O1	-13.7 (13)	C32—C31—P2—O2	-15.5 (12)
C2—C1—P1—O1	3.9 (11)	C26—C25—P2—O2	10.1 (13)

Symmetry code: (i) *x*, -*y*+1, *z*+1/2.

This type of parallel–parallel–orthogonal conformation has been named 'orthogonal flipper' by Dance & Scudder (2000) and is also the conformation adopted in an analogous unfluorinated structure with $FeBr_4^-$ as the counterion (corresponding torsion angles = 19.5, 27.3 and 83.2, and 19.5, 27.3 and 83.2°; Lane et al., 1994). However, when the counter-ion is ClO_4^-, a rotor-type conformation is adopted (corresponding torsion angles = 29.9, 37.3 and 64.1, and 16.2, 30.0 and 42.7°; Antipin et al., 1980). In the structure of **VI**, the orthogonal rings are opposite each other in

the hydrogen bonded dimers and participate in face-to-face π interactions. In contrast, each orthogonal ring is opposite a parallel one in the unfluorinated dimer reported by Lane et al. (1994), facilitating edge-to-face π interactions.

In the structure of **VI**, the P—O bonds of 1.526 (10) and 1.530 (10) Å are significantly longer than typical double P=O bonds of, for example, 1.487 (3) Å in $(C_6H_5)_3P{=}O$ (Thomas & Hamor, 1993) and 1.467 (2) Å in $(C_6F_5)_3P{=}O$ (Nicholson & Thwaite, 2003). However, they are shorter than the single P—O bonds of 1.581 (4), 1.579 (4) and 1.553 (3) Å in triphenylphosphane oxyl derivatives (Kunnari et al., 2001; Carcedo et al., 2004; Chow et al., 1996), which average 1.571 Å. As the P—O bond lengths fall midway between single- and double-bond values, it is clear that the correct depiction of these bonds should be viewed as intermediate single/double bonds. Because of this and as the H atom was not found in the difference electron-density map, it has been fixed at the initial halfway position between the O atoms in this strong hydrogen bond *(Table 3-7-3),* with its displacement parameter refined freely.

Table 3-7-3. Hydrogen- bond geometry (Å, °)

D—H···*A*	*D*—H	H···*A*	*D*···*A*	*D*—H···*A*
O1—H12P···O2	1.20	1.23	2.431 (13)	179

Although this is reasonable it may not be strictly correct, as asymmetric positioning of the H atom is common in even the strongest hydrogen bonds; see, for example, Konu & Chivers (2006) and Antipin et al. (1980), who found that the O···H···O bond in $[\{(C_6H_5)_3P{=}O\}_2H]^+.ClO_4^-$ changes from symmetric at room temperature to asymmetric on cooling.

Packing of the hydrogen-bonded dimers of **VI** forms tunnels parallel to the crystallographic c axis *(Figure 3-7-2).* The tunnels house triiodide anions, which are also aligned along the crystallographic c axis. Within each tunnel, adjacent iodide anions are related by crystallographic c-glide operations. In stacked structures or structures with channels, triiodides often form infinite linear chains with weak $I_3^-\cdots I_3^-$ interactions, with typical I···I separations ≥3.6 Å (Svensson & Kloo, 2003).

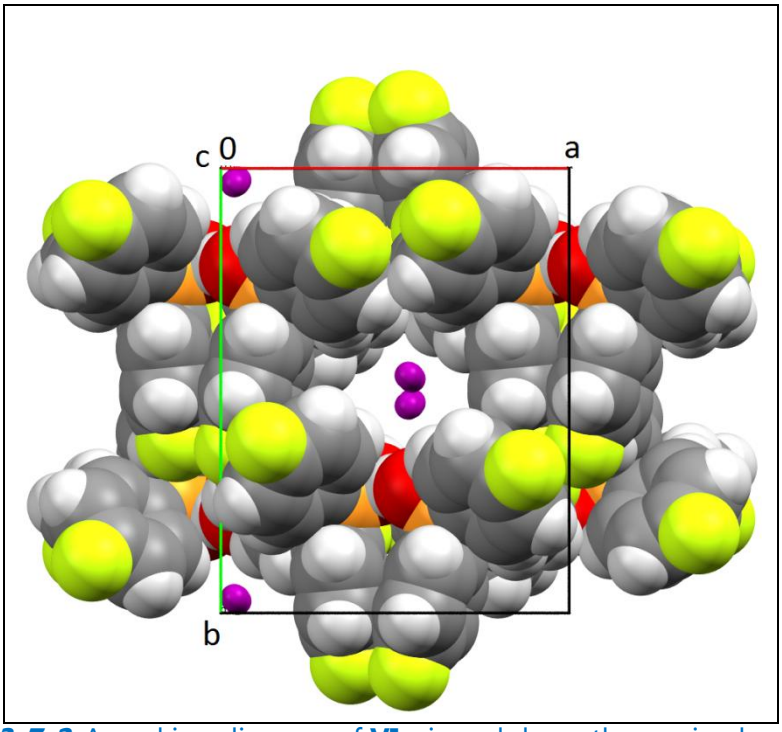

Figure 3-7-2. A packing diagram of **VI**, viewed down the *c* axis, showing the channels that house the I_3^- anions.

The I···I distance of 3.5774 (11) Å seen in **VI** is a rare example of an interionic I_3^-··· I_3^- separation of less than 3.6 Å. In contrast, the most significant contact between the triiodide anion and the surrounding tunnel atoms is 3.156 Å between phenyl atom H32 and the central iodine atom I1, which is only marginally shorter than the van der Waals contact (3.35 Å; Harrison, 1978).

The two I—I bonds [2.9023 (15) and 2.9452 (14) Å] show significant asymmetry. This is not unusual and is caused by nonbonded interactions within the crystal structure. In the case of **VI**, the most significant sub-van der Waals contacts involving the terminal triiodide I atoms are I···I contacts, which are of equal length for symmetry reasons. However,

atom I2 has five I···H contacts shorter than the sum of the van der Waals radii (3.283–3.347 Å), compared with only two for I3 (3.222 and 3.291 Å).

3-7-1. Experimental

C-bound H atoms were idealized with C—H bond lengths of 0.95 Å and with the H atom on the external bisector of the C—C—C angle, with $U_{iso}(H) = 1.2U_{eq}(C)$. Initial refinement with anisotropic displacement parameters for all non-H atoms converged to R1 =0.0659 with a maximum $\Delta \rho_{max}$ of 5.79 e $Å^{-3}$.

Table 3-7-4. Data collection and refinement details for **VI**

Data collection	
Diffractometer	Nonius KappaCCD area-detector diffractometer
Absorption correction	Multi-scan (*SORTAV*; Blessing, 1995)
T_{min}, T_{max}	0.645, 0.856
No. of measured, independent and observed [$I > 2\sigma(I)$] reflections	14255, 5376, 4363
R_{int}	0.081
$(\sin\theta/\lambda)_{max}$ (Å^{-1})	0.606
Refinement	
$R[F^2 > 2\sigma(F^2)]$, $wR(F^2)$, S	0.050, 0.131, 1.05
No. of reflections	5376
No. of parameters	466
No. of restraints	17
H-atom treatment	H-atom parameters constrained
	$w = 1/[\sigma^2(F_o^2) + (0.0392P)^2 + 81.0459P]$ where $P = (F_o^2 + 2F_c^2)/3$
$\Delta\rho_{max}$, $\Delta\rho_{min}$ (e Å^{-3})	2.03, -1.60
Absolute structure	Flack (1983), with 1024 Friedel pairs
Absolute structure parameter	0.50 (3)

A posteriori screening for twinning by looking for $F_o^2 >> F_c^2$ was carried out using PLATON (Spek, 2009). A nonmerohedral twin, with {100} as the twin plane *(Figure 3-7-4)* and with twin matrix (1

0 0.459, 0 -1 0, 0 0 -1), was identified and used to construct expanded reflection files, in which overlapping reflections were assigned indices for each contributing twin domain. The inclusion of inversion twins gave a total of four domains: (i) the initial domain, (1 0 0, 0 1 0, 0 0 1); (ii) the inverse of (i), (-1 0 0, 0 -1 0, 0 0 -1); (iii) a nonmerohedral twin, (1 0 0.459, 0 -1 0, 0 0 -1); and (iv) the inverse of (iii), (-1 0 -0.459, 0 1 0, 0 0 1).

Three expanded reflection files were generated using three different 2θ resolution tolerance criteria for establishing nonmerohedral reflection overlap, namely 0.05, 0.10 and 0.15°, which gave 465, 863 and 1210 overlapping reflections, respectively. Refinements carried out using these reflection files, in which the fractional contribution volumes of the above domains were allowed to vary, were compared on the basis of R factors, bond-length s.u. values, mean (F_o^2)/mean (F_c^2) distribution versus F_c/F_c (max) and $\Delta \rho_{max}$, and, in each case, the 0.05° data were found to be the best, e.g. $\Delta \rho_{max}$ values for the 0.05, 0.10 and 0.15° 2θ tolerance data were 3.24, 4.02 and 5.28 e $Å^{-3}$, respectively. All further structure refinement was therefore carried out using the 0.05˚ data. The fractional contribution volumes refined to 0.37 (3), 0.38 (3), 0.124 (6) and 0.123 (6) for domains (i)–(iv), respectively. The last two numbers were restrained to be equal because of the high correlation between the two parameters (-0.99).

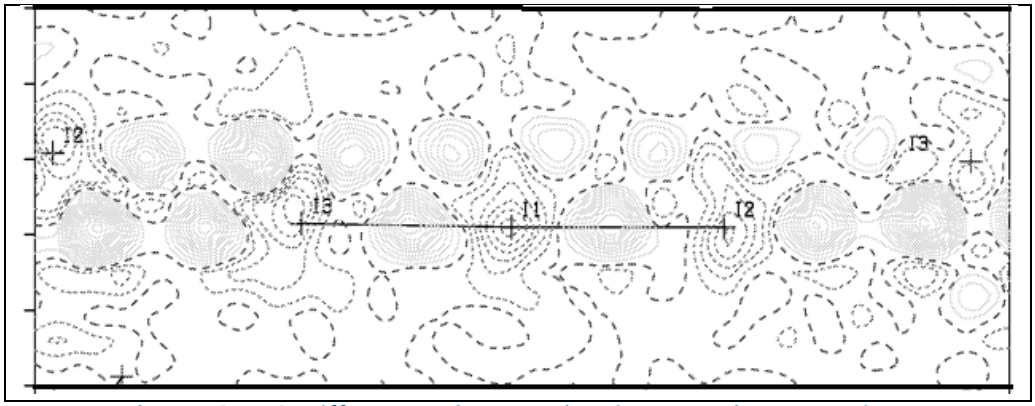

Figure 3-7-3. Difference electron density map close to I_3^- in **VI**

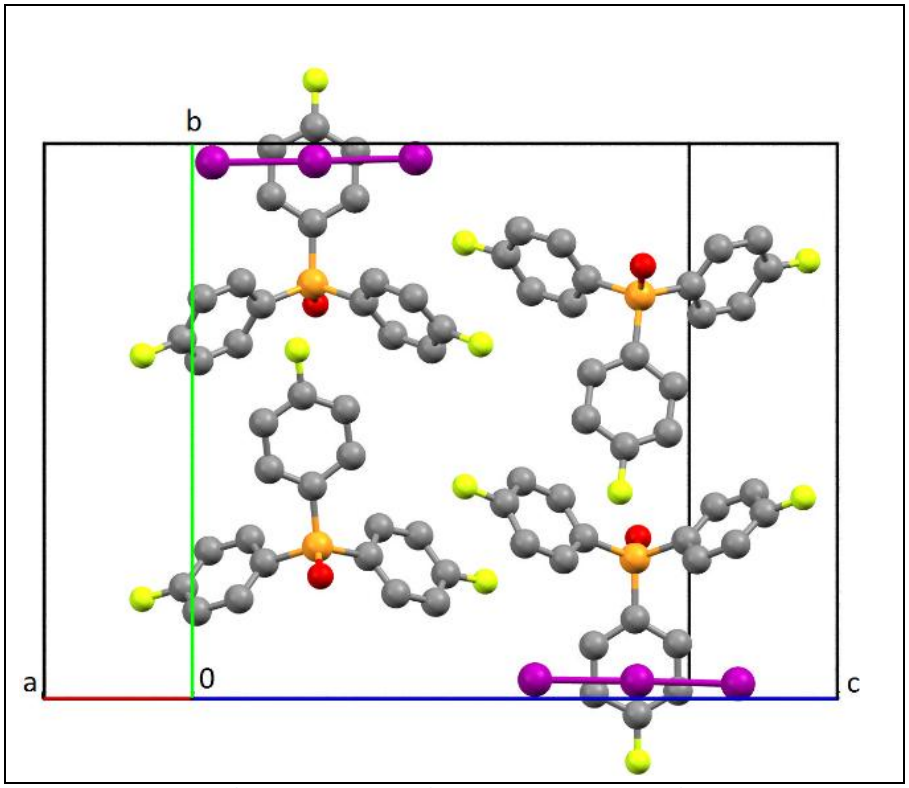

Figure 3-7-4. A view of the packing of **VI** in the vicinity of the ***bc*** plane, showing local non-crystallographic two fold rotation and mirror symmetries, which act as a twinning plane

Ideally, twinning should be dealt with at the data-processing stage, but this was not possible with the version of the diffractometer software being used in the current case. Given the

rudimentary method used to assign nonmerohedral reflection overlap, i.e. a global 2θ tolerance parameter, which assumes average reflection width, shape and twin obliquity, it is reasonable to anticipate that further improvements could be achieved if the software examined each reflection on a more individual basis, allowing for crystal anisotropy and the way the area detector intersects the Ewald sphere. Also, the small changes that are automatically made to the orientation matrix to compensate for slight crystal movement during the data collection could also be taken into account, rather than assuming a fixed orientation matrix. In fact, the nonmerohedral twin correction was only partially successful and left rows of residual electron-density peaks spanning the cell in the z direction near the triiodide ions, with an inter-peak separation of approximately half an I—I bond, which also approximates to c/12 *(Figure 3-7-3).* The two highest remaining peaks in the residual electron-density map were suitably positioned to be modelled as a translational disorder of the triiodide anions along the channels. They were therefore treated as disordered minor I-atom sites I2B and I3B, whose occupancies refined to 0.021 (4) and 0.030 (4), respectively, reducing $\Delta \rho_{max}$ to 2.03 e $Å^{-3}$. The minor-site displacement parameters were subjected to 'rigid-body' restraints, in which the anisotropic displacement parameters in the direction of their I—I bonds, I2—I3B and I3—I2B, were restrained to be equal. Also, the

U^{ij} values for the minor I-atom sites were restrained to be equal to those of the major I-atom sites they are bonded to, as the I atoms in the minor sites are generated from those in the major sites by translation of the triiodide along the channels parallel to c.

3-7-2. Synthesis

$(p\text{-}FC_6H_4)_3P$ (0.418 g, 1.32 mmol) was dissolved in anhydrous diethyl ether (30 ml). To this was added iodine (two equivalents, 0.671 g, 2.64 mmol), which caused rapid precipitation of a brown solid. The reaction was stirred for 48 h, after which time the solid was isolated by standard Schlenk techniques. Crystals were prepared by dissolving the brown solid in dichloromethane (5 ml) in a Rotaflo tube. Hexane (15 ml) was layered on top of the solution and the layers were allowed to diffuse slowly over a period of 48 h, after which time purple–brown crystals of **VI** had formed.

3-8. Conclusions

This work is the first structural study of the tri-o-tolylphosphonium cation and shows that it retains the exo_3 configuration in all the investigated crystal structures and that the C_{Me}-P-C_{Ph}-C_{Ph} torsion angle is remarkably constant with mean values ranging from 49.1 to 52.3° and individual values from 45.5(9) to 55.4(8)° *(table 3-8-1)*.

Table 3-8-1. The three tri-o-tolylphosphonium torsion angles that define the exo_3 configuration in structures **I** to **V**. Any sets that are all negative have been replaced by positive values, as permitted by a centrosymmetric space group.

Structure	C_{Me}-P-$C_{Ph}C_{Ph}$ torsion angles (°)			
	Φ_1	Φ_2	Φ_3	Φ_{mean}
I	48.8(9)	50.4(8)	55.4(8)	51.5
I	45.5(9)	50.1(8)	54.7(9)	50.1
II	49.5(5)	52.6(4)	54.5(4)	52.2
III	49.3(6)	50.8(6)	50.9(6)	50.3
III	50.5(6)	52.8(6)	53.7(6)	52.3
IV	48.2(11)	51.3(11)	54.0(11)	51.2
V				50.1
V				49.1

It is also noteworthy that even under the heaviest iodine loading, adjacent tri-o-tolylphosphonium cations are able to participate in π-π-bonding with inter-ring contacts of approximately 3.3 Å.

As would be anticipated I…I interactions increase with iodine loading but, even for the I_8^{2-} anions in structure **IV** the inter-anion I…I contacts that link the anions into an extended structure are

extremely tenuous at 3.977(1) Å. In **V** the disordered polyiodide layers feature many, relatively short, I…I contacts, reminiscent of the alpha-cyclodextrin metal iodide inclusion compounds (Rietman, 1990), offering the possibility of electrical conduction but would not be of practical use as it readily looses iodine, converting to structure **IV**.

A comparison of the triiodides **III** and **VI** provides a dramatic example of the influence of the surrounding matrix on the closest approach of the triiodide anions.

In **III**, the closest approach is side-on and slightly above the VDW limit but there is a hint that one of the triiodides has been bent to avoid closer contact. In contrast the triiodides in **VI** are remarkably close at 3.5774 (11) Å with the closest I…H approach of 3.156 Å.

3-9. References

Allen, F. R. (2002). *Acta Cryst.* B**58**, 380–388.

Altomare, A., Cascarano, G., Giacovazzo, C., Guagliardi, A., Burla, M. C., Polidori, G., Camalli, M. (1994). *J. Appl. Cryst.* **27**, 435-436.

Antipin, M. Yu., Kalinin, A. E., Struchkov, Yu. T., Matrosov, E. I., Kabachnik, M. I. (1980). *Kristallografiya*, **25**, 514–515.

Blessing, R. H. (1995). *Acta Cryst.* A**51**, 33–38.

Burnett, M. N. & Johnson, C. K. (1996). Report ORNL-6895. Oak Ridge National Laboratory, Tennessee, USA.

Cameron and Millar, (1974), *Cryst. Struct. Comm.*, **3**, 489-490.

Carcedo, C., Dervisi, A., Fallis, A. L. O. I. & Malik, A. (2004). *Chem. Commun*. 1236–1237.

Chow, T., Pyngli, L., Lee, R., Jiuhlin, K., Yow Chen, C. (1996). *J. Chem. Soc. Perkin Trans. 2*, 2681–2685.

Coppens, P., Leung, P. C. W., Ortega, R., Young, W. S. and Laporta, C. J., (1983), *Phys. Chem.*, **87**, 3355-3359.

Courtois, B. (1813) *Ann. Chim.* **88**, 304 – 310.

Dance, I., Scudder, M. (2000). J*. Chem. Soc. Dalton Trans*. 1579–1585.

Farrugia, L. J. (1997). *J. Appl. Cryst.* **30**, 565-570.

Farrugia, L. J. (1999). *J. Appl. Cryst.* **32**, 837–838.

Fey, N., Howell, J.A.S., Lovatt, J.D., Yates, P.C., Cunningham, D., McArdle, P., Gottlieb, H.E., Coles, S.J., (2006), *Dalton Trans*, 5464-5475.

Flack, H. D. & Bernardinelli, G. (2000). *J. Appl. Cryst.* **33**, 1143–1148.

Grafe-Kavoosian, A., Nafepour, S., Nagel, K., Tebbe, K. –F, (1998), *Z.Naturforsch B:Chem.Sci.*, **53**, 641-646.

Harrison, R. D. (1978). Book of Data, p. **54**. London: Nuffield Advanced Science, Longman Group Ltd.

Havinga, E.E., Boswijk, K.H. and Wiebenga, E.H. (1954) *Acta Cryst*. **7**, 487.

Horn, C., Scudder, M., Dance, I. (2001) *Cryst. Eng. Comm*, **3**, 1-10.

Howell, J. A. S., Palin, M. G., Yates, P. C., McArdle, P., Cunningham, D.,Goldschmidt, Z., Gottlieb, E. H., Lagerman, D. H. (1992). *J.Chem. Soc. Perkin. Trans. 2*, 1769–1775.

Kopper, F.C., Feiters, M.C., Olofsson, B., Kaiho, T., Yanagida, S., Zimmermann, M.B., Carpenter, L.J., Luther III, G.W., Lu, Z., Jonsson, M., and Kloo, L. (2011) *Angew. Chem. Int. Ed.*, **50**, 11598 – 11620

Kuhn, N., Kotowski, H., Steimann, M., Speiser, B., Wurde, M., Henkel, G., (2000) *J.Chem.Soc.,Perkin Trans. 2*, 353-363

Kunnari, M., Oilunkaniemi, R., Laitinen, S., Ahlgren, M. (2001). *J. Chem. Soc. Dalton Trans*. 3414–3415.

Konu, J., Chivers, T. (2006).). *J. Chem. Soc. Dalton Trans*. 3941–3942.

Kuz'mina, N.E., Palkina, K.K., Savinkina, E.V., Kozlova, I.A., Kuznetsov, N.T., (2000) *Zh.Neorg.Khim.(Russ.)(Russ.J.Inorg.Chem.)*, **45**, 6-10.

Lane, H., Godfrey, S. M., McAuliffe, C. A. & Pritchard, R. G. (1994). *J. Chem. Soc. Dalton Trans*. 3249–3250.

Macromolecular Crystallography, Part A, edited by C. W. Carter Jr., R. M. Sweet, 307-326. New York: Academic Press

Macrae, C. F., Edgington, P. R., McCabe, P., Pidcock, E., Shields, G. P., Taylor, R., Towler, M., van de Streek, J. (2006). *J. Appl. Cryst.* **39**, 453–457.

Hooft, R.W. (1998). COLLECT. Nonius BV, Delft, The Netherlands.

Nyhlen, J., Boschloo, G., Hagfeldt, A., Kloo, L. and Privalov, T., (2010), *ChemPhysChem*, **11**, 2140-2145.

Otwinowski, Z., Minor, W., (1997)., *Methods in Enzymology*, 276, 307-326.

Palatinus, L., Chapuis, G. (2007). *J. Appl. Cryst.* **40**, 786–790.

Pritchard, R.G. and Moreland, L. (2006). *Acta Cryst*. **C62**, o656-o658.

Privalov, T., Boschloo, G., Hagfeldt, A., Svensson, P.H. and Kloo, L.,(2009), *J. Phys. Chem*. C, **113**, 783–790

Rietman, E.A., (1990), *Mat. Res. Bull.*, **25**, 649-655.

Santiago A., (2013), *J. Chem. Soc.*, *Dalton Trans.*, **42**, 8617-8637

Schiffmann, F., Vondele, J.V., Hutter, J., Urakawa, A., Wirz, R. and Baiker, A., (2010), *Proc Natl Acad Sic*, **107**, no 11, 4830–4833

Sheldrick, G. M. (2008). *Acta Cryst.* A**64**, 112–122.

Spek, A. L. (2003). *J. Appl. Cryst.* **36**, 7–13.

Svensson, P.H. et al (1998) *J. Chem. Soc.*, *Dalton Trans.*, 1425–1429

Svensson, P.H. and Kloo, L., (1999), *Inorg. Chem.*, **38**, 3390-3393

Svensson, P.H. and Kloo, L., (2003) *Chem. Rev*, **103**, No. 5, 1649-1684

Svensson, P. H., Kloo, L. (2003). *Chem. Rev.* **103**, 1650–1683.

Thomas, J. A., Hamor, T. A. (1993). *Acta Cryst.* **C49**, 355–357.

Westrip, S. P. (2008). Software used to prepare material for publication: *publCIF.*

4- 2,2`-dipyridyl ketone and its reactions with 3d transition metal and lanthanides salts

4-1. Introduction

2,2′-dipyridyl ketone forms colourless crystals with a melting point of 52-55°C and dissolves in water and organic solvents.

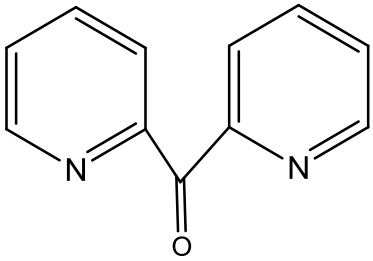

In the crystalline state its pyridyl rings are not co-planar (Hans et al. 1998) *(Figure 4-1-1).* Also, in contrast to its Chemdraw view above, the two pyridyl rings have adopted an anti configuration with torsion angles O-C-C-N of -40.9 (2) and 163.3 (1) ° .

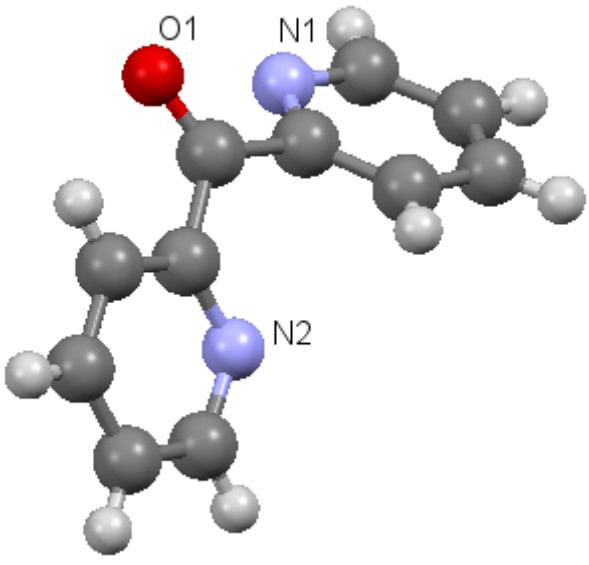

Figure 4-1-1. Illustration of 2,2′-dipyridyl ketone molecule.

The anti configuration removes the repulsive interaction between the nitrogen, N2, electron pair and the in-plane CO oxygen electron pairs but N1 has reduced the repulsion by twisting relative to the CO bond.

2,2′-dipyridyl ketone offers the synthetic chemist two reaction avenues with transition metals centres:

1- It can utilise two pyridine N atoms to act as a bidentate ligand (Sarkar et al, 2005).

2- The ketonic carbon is susceptible to attack by Lewis bases to form tri-substituted methanol which has the potential to act as a tri-dentate or even tetra-dentate ligand, (Basu et al, 1988; Abrahams et al, 2006).

Abrahams et al (2006) synthesised a new generation of ligands from 2,2′-dipyridyl ketone coordinated to metal through nucleophilic attack by pyrazole and SO_3^{-2}. This work was extended more recently by Efthymiou et al (2011).

In this chapter the synthesis of a number of novel 2,2′-dipyridyl ketone based metal complexes are reported. The first two complexes are monomers which contain Cu and Co and were synthesised from water. The next two complexes are Cu dimers one of which was synthesised in alcohol solution and the another

in water. Following that two dimeric Pr complexes are presented which both crystallized from the same aqueous solution. A series of monomeric iso-structural complexes of Dy, Er, Ho and Yb are than reported, followed by a further two iso-structural monomeric complexes of Pr and Nd, which have a different molecular structure to those of the first series. Finally the synthesis and structural characterisation of a Fe^{II} complex of 2,2′dipyridyl, methoxy pyrazole is discribed.

The complexes presented in this chapter are listed below.

- Bis[hydroxybis(pyridin-2-yl)methanesulfonato-κ^3N,O,N′]MII series (M = Mn to Zn) with the copper(II) and cobalt(II) structures
- Poly-(μ-nitrato-O,O′)[{μ_2-di 2 pyridyl (hydroxy) methanolato-N,N′,O}-{μ-pyrazolato-N,N′}-di-pyrazol-nitrato-di-copper(ii)] mono hydrate
- $[(C_{11}H_{10}N_2O_2C_2H_5)(C_3H_3N_2)_2(NO_3)_4Cu_2]_3\,(C_2H_5OH)$
- $(C_{11}H_8N_2OSO_3)_2(NO_3)_2Pr_2(H_2O)_n$
- $(C_{11}H_8N_2OSO_3)_2Pr_2(SO_3)_2(H_2O)_n$
- $[(C_{11}H_8N_2O)\ OCH_3]_2\ LnCl_2$, Cl Ln = Dy, Er, Ho and Yb
- $[(C_{11}H_8N_2O)\ OCH_3]_3\ LnCl_3$ Ln = Pr and Nd
- $[(C_{11}H_8N_2)OH(C_3H_3N_2)]_2$ Fe

4-2. Bis[hydroxybis(pyridin-2-yl)methanesulfonato-κ^3N,O,N′]MII series (M = Mn to Zn) with the copper(II) and cobalt(II) structures

The current study is based on work carried out by Abrahams et al (2006), who generated transition metal complexes of tri substituted methanol ligands from 2,2′-dipyridyl ketone, using the metal centre as a template. An example of their synthesis, in which aqueous solutions of 2,2′-dipyridyl ketone, with various divalent transition metal cations, including Mn, Fe, Co, Ni, Cu and Zn and bisulfite were mixed in a ratio of 2:1:2 is given below *Scheme 4-2-1.*

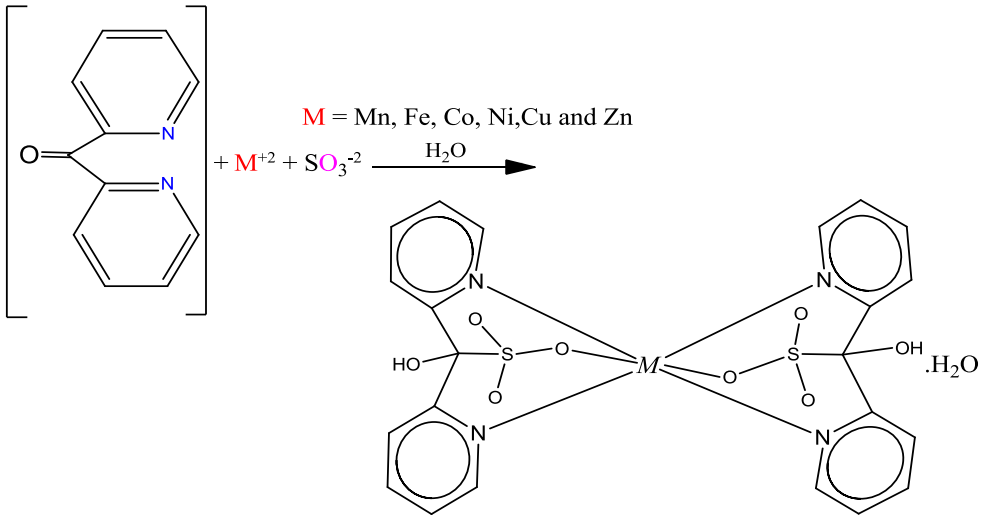

Scheme 4-2-1. The divalent transition metal in centre from (Mn to Zn) obtained from synthesises above, which structure complexes of **VII** and **VIII** have been considered

The reaction conditions used by Abrahams et al (2006) failed to produce the copper complex and the crystals of the cobalt

compound were not of sufficient quality for full single crystal structure determination.

In an effort to improve crystal quality it was decided to use more dilute solutions of 0.025 M and 0.05 M compared to the 0.27 M and 0.54 M solutions used by Abrahams et al (2006) in their synthesis. The solutions were left standing in open containers at room temperature. After a week good quality crystals formed in the containers and were subjected to single crystal X-ray diffraction measurements. Crystal details are presented in *Table 4-2-1* and labelled ORTEP view in *Figure 4-2-1* selected bond length and angles are presented in *Tables 4-2-4*.

The Cu^{II} complex bis[hydroxybis(pyridin-2-yl)methanesulfonato-κ^3 N,O,N′]copper(II) hexahydrate, $[Cu(C_{11}H_9N_2O_4S)_2]\cdot 6H_2O$, (**VII**), crystallizes in the space group $P\bar{1}$, compared with $P2_1/c$ for the anhydrous Co^{II} analogue bis[hydroxybis(pyridin-2-yl)methanesulfonato-κ^3N,O,N′] cobalt(II), $[Co(C_{11}H_9N_2O_4S)_2]$, (**VIII**). However, both molecules sit on a crystallographic inversion centre and are thus very similar in appearance.

Jahn–Teller elongation of the Cu—O bonds [2.347 (3) Å in **VII** and 2.064 (2) Å in **VIII**] influences the S—O bond lengths, which are all around 1.455 (3) Å in **VII** and 1.436 (2)–1.473 (2) Å in **VIII**.

The distinction between bonding and supramolecular interactions is blurred in Jahn–Teller-distorted systems, where the weakening

of some coordination bonds puts them on a par with hydrogen bonds. The interplay between the two types of bonding is of particular interest in copper complexes because of its occurrence in enzymes, e.g. the active site in copper amine oxidase from Hansenula polymorpha Li et al. (1998).

Because of their complexity and, often, low resolution, protein structures are not the ideal platform for studying the subtler details of the relationship between these two interactions. Small inorganic complexes and salts provide a higher resolution and a more systematic means of investigation.

Beagley et al. (1989) established that, for the hexaaqua divalent metal cations in Tutton's salts, $Cs_2[M(H_2O)_6](SO_4)_2$, Jahn–Teller distortion weakens the hydrogen bonds from the coordinated water, with elongated Cu—O bonds. This is because the partial positive charge on their H atoms is reduced relative to the water H atoms, which are more fully coordinated to the metal.

The current study is based on work carried out by Abrahams et al. (2006), who previously reported the structures of the bis[hydroxybis(pyridin-2-yl)methanesulfonato-κ^3 N,O,N′]- M^{II} complexes for Mn, Fe, Ni and Zn. The structures of the Co and Cu complexes reported herein, namely bis[hydroxybis-(pyridin-2-yl)methanesulfonato-κ^3N,O,N′]copper(II) hexahydrate, and

bis[hydroxybis(pyridin-2-yl)methanesulfon ato- κ^3 N,O,N′]cobalt^{II} , complete the series from Mn to Zn.

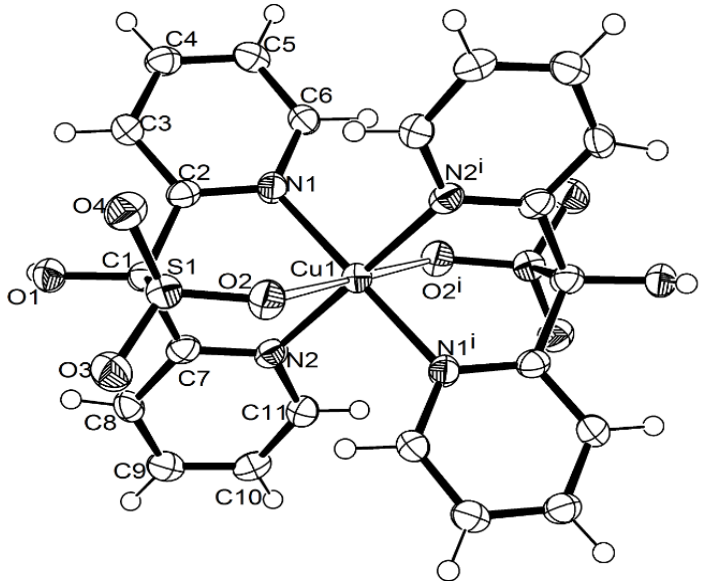

(a)

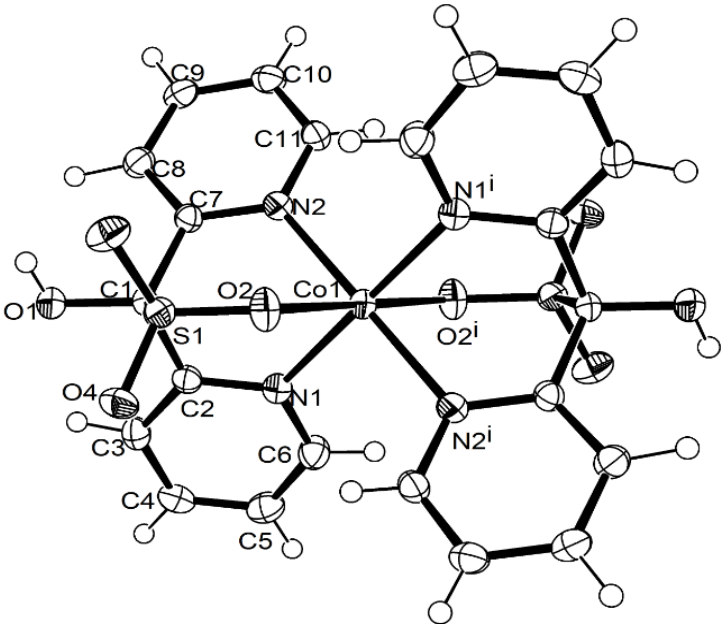

(b)

Figure 4-2-1. (a) The structure complex of (**VII**), showing the atom-labelling scheme. Displacement ellipsoids are drawn at the 50% probability level. The solvent water molecules have been omitted for clarity. (b) The structure complex of (**VIII**), showing the atom-labelling scheme. Displacement ellipsoids are drawn at the 50% probability level. [Symmetry codes: (v) -x + 2, -y + 1, -z + 1; (i) -x + 1, -y + 1, -z + 1.]

Each divalent metal in **VII** and **VIII** is coordinated by two hydroxybis (pyridin-2-yl)methanesulfonate ligands in a centrosymmetric arrangement (*Figures 4-2-1 a and b*), with distinct Jahn–Teller tetragonal elongation involving the M—O bonds in the Cu case. The Jahn–Teller radius, R_{JT}, calculated using $R_{JT}^2 = \sum_{i=1}^{6} \Delta d_i^2$, where d_i represents the deviation of the ***i***th M—L bond length from the mean of the six (Falvello, 1997), has a value of 0.385 Å, which is appropriate for the static Jahn–Teller tetragonal distortion seen in this case. It is interesting that, despite all the complexes being crystallized from aqueous solutions, it is only the copper complex that forms a hydrate; all the other complexes in this series form iso-structural anhydrous crystals.

The extent of the M—O Jahn–Teller distortion can be seen when the M—O and M—N bond lengths from Abrahams et al. (2006) and the current work are plotted against *d* electron configuration *(Figure 4-2-2),* while a similar plot of the three S—O bond lengths against d electron configuration *(Figure 4-2-3)* shows the combined effect of hydrogen bonding and coordination on the sulfite group.

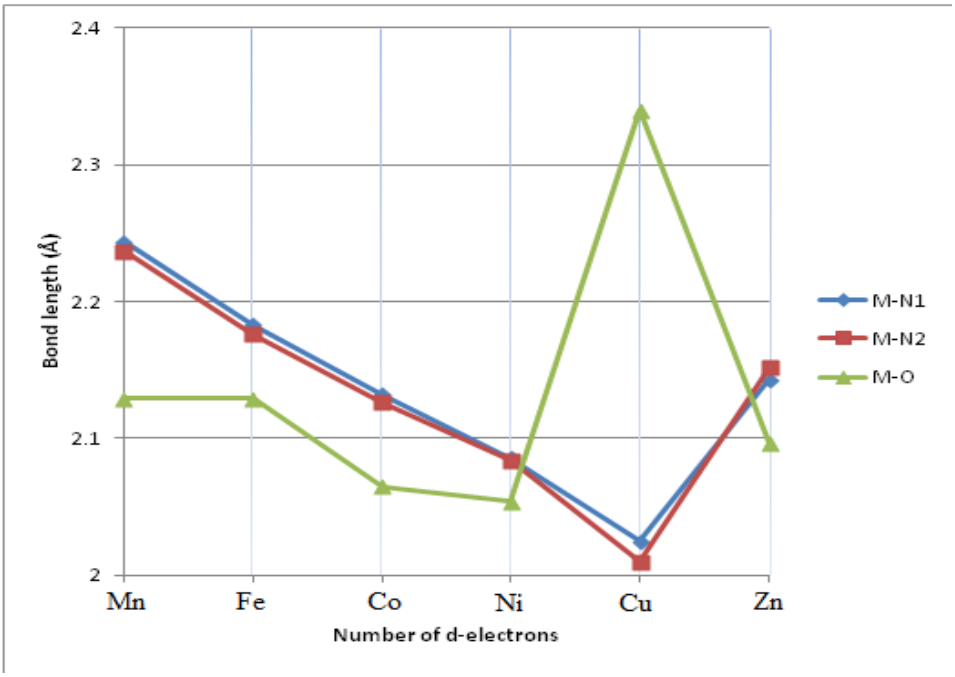

Figure. 4-2-2. Bond lengths to the transition-metal atom in the bis[hydroxybis(pyridin-2-yl)methanesulfonato-κ^3N,O,N′]M^{ii} series, where M = Mn to Zn

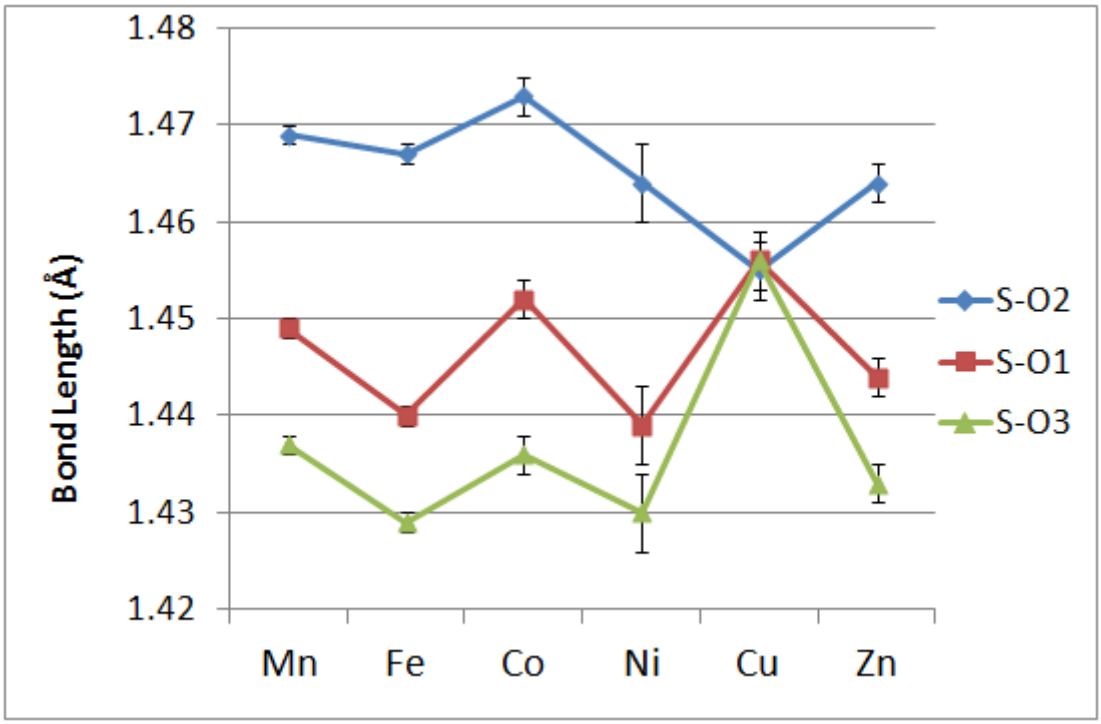

Figure 4-2-3. S—O bond lengths in the bis[hydroxybis(pyridin-2-yl)methanesulfonato-κ^3N,O,N′]MII series, where M = Mn to Zn.

The S—O bond for the coordinated O atom is significantly longer than the two noncoordinating S—O bonds in all but the copper complex. The nearly identical S—O bond lengths in the copper complex suggest that the strength of the Cu· · ·O interaction is on a par with the SO· · ·HOH hydrogen bonds *(Figure 4-2-4).* This contrasts with the situation in all the other complexes, where the S—O bonds involving the coordinated O atom remain significantly longer than the other S—O bonds, despite the involvement of one of the other O atoms in a strong hydrogen bond with the alcohol H atom *(Figure 4-2-5).*

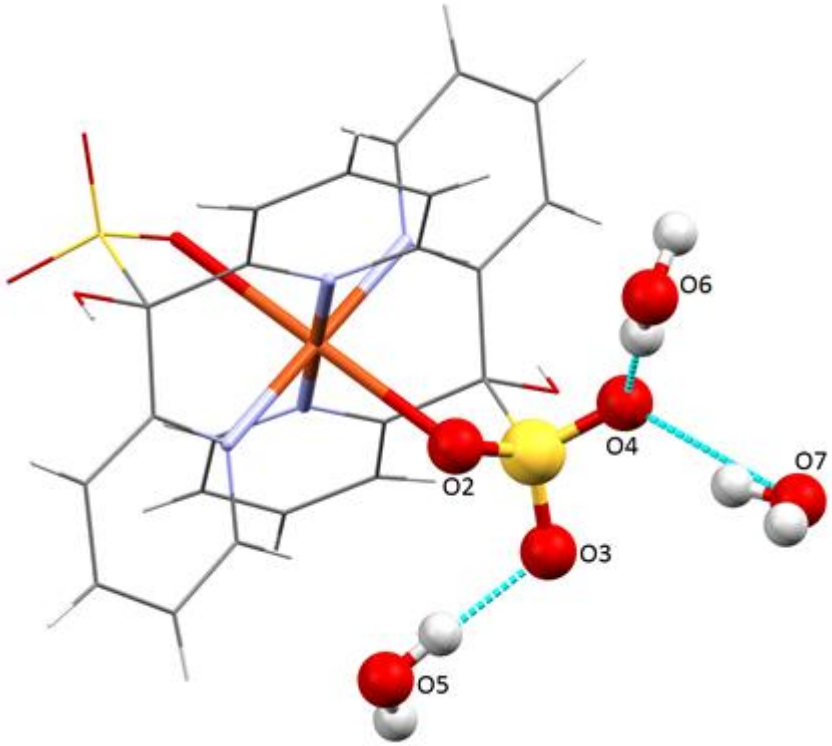

Figure 4-2-4. Water–sulfate hydrogen bonding in complex **VII** (dashed lines). [Symmetry code:(vii) x + 1, y, z.]

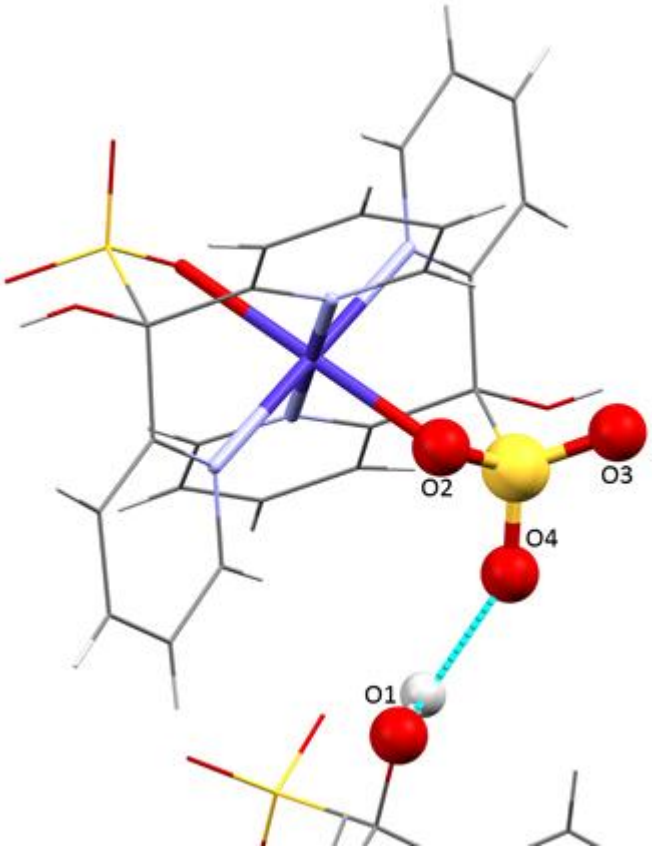

Figure 4-2-5. Hydroxy–sulfate hydrogen bonding in complex **VIII** (dashed lines). [Symmetry code: (viii) -x + 1, y – 1/2, -z + 1/2.]

A useful comparison may be made between the current structure of **VII** and bis[bis(3,5-dimethylpyrazol-1-yl)acetato]-copper(II) and its hydrate (Kozlevcăr et al., 2003). In both these structures, the Cu atom sits on an inversion centre. In the anhydrous compound, typical Jahn–Teller elongation of the Cu—O bonds is observed. On dehydration, the Cu—O bond shrinks and a pair of Cu—N bonds lengthen to maintain the Jahn–Teller distortion. This is an unusual situation, as only 5% of crystal structures established to date in the well studied CuN_4O_2 system adopt Cu—N elongation rather than Cu—O. In the anhydrous compound, a significantly longer

C—O bond length 1.262 (3) Å is observed for the coordinated carboxylate O atom than for the noncoordinated carboxylate O atom [1.214 (3) Å]. For the hydrated compound, the two C—O bond lengths are indistinguishable [1.245 (4) and 1.241 (4) Å]. The authors attributed the similar carboxylate C—O bonds in the hydrate to the binding of both O atoms to a Lewis acid, i.e. to the Cu and to a water molecule. In Cu structure complex **VII**, the overall effect is to make all three S—O bonds identical within experimental error, suggesting that a similar process to that seen in the above carboxylate is in operation.

The triclinic crystal structure of the copper complex includes water of crystallization but all other members of the series are anhydrous and form monoclinic iso-structural crystals *(Table 4-2-1).* The difference in molar volume between the copper and cobalt structure is 692.53 – 1118.52/ 2 = 133.27 $Å^3$. This value is as expected for the extra six water molecules per complex molecule found in the copper structure.

Table 4-2-1. Crstallographically comparison of the two crystals $[\{(C_5H_4N)_2(SO_3)C(OH)\}_2Cu.6H_2O]$ and $[\{(C_5H_4N)_2(SO_3)C(OH)\}_2Co]$

Bis[hydroxyl(dipyridin-2-yl)methanesulfonato-N,N',O]-M(ii), M=Cu,Co		
	Cu	Co
Formula	$[\{(C_5H_4N)_2(SO_3)C(OH)\}_2Cu.6H_2O]$	$[\{(C_5H_4N)_2(SO_3)C(OH)\}_2Co]$
M_w	702.16	589.45
Crystal syst	triclinic	monoclinic
Space group	P -1	P $2_1/c$
a/Å	7.5892(3)	7.7300(3)
b/Å	10.1399(4)	9.3475(4)
c/Å	10.7325(5)	15.6518(6)
α/deg	108.675(2)	90.00
β/deg	109.920(2)	98.499(2)
γ/deg	101.025(4)	90.00
$V/Å^3$	692.527	1118.52
Z	1	2
R	6.4	4.43

It is thought that the structural changes brought about by *Jahn-Teller* distortion are not sufficient to change the hydrogen bonding opportunities; however bond length changes about the S atom suggest that the SO_3 group carries a greater negative

charge when the bond to the metal is weakened by *Jahn-Teller* distortion *(Table 4-2-2).*

Table 4-2-2. The sulfate distance to oxygen in the two crystals $[\{(C_5H_4N)_2(SO_3)C(OH)\}_2Cu.6H_2O]$ and $[\{(C_5H_4N)_2(SO_3)C(OH)\}_2Co]$ (the distance are in Å)

	O1	O2	O3
$[\{(C_5H_4N)_2(SO_3)C(OH)\}_2Cu.6H_2O]$	1.453(3)	1.464(4)	1.457(5)
$C_5H_4N)_2(SO_3)C(OH)\}_2Co]$	1.473(3)	1.452(3)	1.436(3)

Over 3500 structures containing the SO_3 group as part of structure were identified in the Cambridge Crystallographic Data base (CCD) single and double SO bonds were distinguished by searching for the fragments shown below and histograms for the two type of bonds are presented in *Figure 4-2-2*.

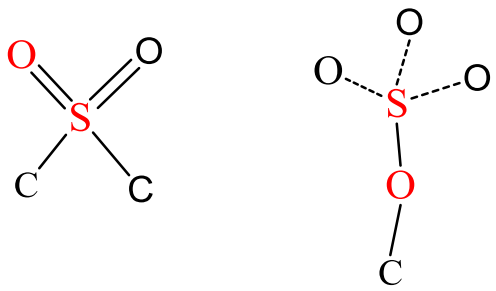

For the single bond the average distances is 1.602Å, and the average double bond distance is 1.437Å. For both complexes **VII** and **VIII** the bond distances of S···O are 1.453 and 1.473Å. *(See Table 4-2-2)*

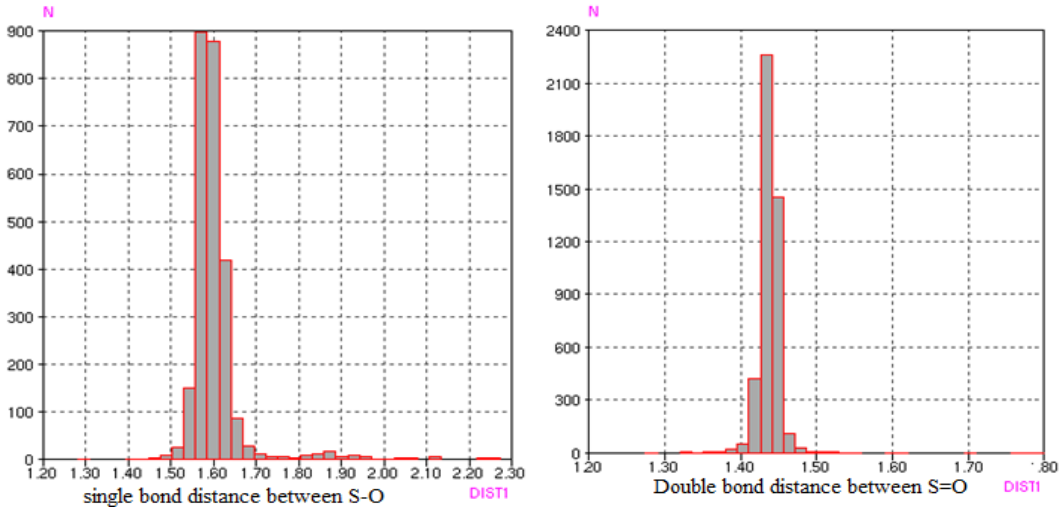

Figure 4-2-2. The fragment of -S···O were used for the single (left) and double (right) bond distances between S to O. The sulfur tri-oxide is bonded to compounds, the collection are from the Cambridge crystallography database

4-2-1. Experiment

H atoms were refined isotropically in both structures **VII** and **VIII**. Additionally, for the complex **VII**, distance restraints were applied to the water H atoms, whereby the O—H distances were restrained to 0.958 (10) Å and the H···H distances to 1.516 (10) Å.

4-2-2. Synthesis

The complexes of **VII** and **VIII** were prepared using aqueous solutions of 2,2′-dipyridyl ketone, sodium bisulfite and transition metal nitrate in a 2:2:1 molar ratio. 0.025M 2,2′-dipyridyl ketone (2 ml), 0.025M sodium sulfite (2 ml) and 0.025M copper or cobalt nitrate (1 ml). These were mixed together and left to stand in open containers at room temperature for a week in order to produce good-quality crystals.

Table 4-2-4. Selected geometric parameters (Å , ˚) for (**VII**).

N1—Cu1	2.020 (3)	O2—Cu1	2.347 (3)
N2—Cu1	2.009 (4)	O3—S1	1.455 (3)
O2—S1	1.455 (3)	O4—S1	1.456 (3)
N2—Cu1—N1	85.91 (14)	N1—Cu1—O2	88.63 (12)
N2—Cu1—O2	85.52 (13)		

Table 4-2-5. Hydrogen-bond geometry (Å, ˚) for (**VII**).

D—H···A	D—H	H···A	D···A	D—H···A
O1—H1···O6	0.83 (6)	1.84 (6)	2.653 (5)	167 (6)
O5—H5A···O3	0.96 (1)	1.83 (1)	2.783 (5)	176 (6)
O5—H5B···O1^{i}	0.96 (1)	2.15 (6)	2.902 (5)	134 (7)
O5—H5B···O3^{i}	0.96 (1)	2.41 (4)	3.212 (5)	141 (5)
O6—H6A···O4^{ii}	0.96 (1)	1.87 (1)	2.828 (5)	178 (5)
O6—H6B···O7^{iii}	0.97 (1)	1.82 (2)	2.731 (6)	155 (4)
O7—H7A···O4	0.96 (1)	1.91 (2)	2.828 (5)	157 (5)
O7—H7B···O5^{iv}	0.96 (1)	1.80 (2)	2.745 (5)	168 (6)

Symmetry codes: (i) -x+1, -y+1, -z; (ii) x-1, y, z; (iii) –x+1, -y, -z; (iv) -x+2, -y+1,-z.

Table 4-2-6. Selected geometric parameters (Å, ˚) for (**VIII**).

N1—Co1	2.127 (3)	O2—Co1	2.064 (2)
N2—Co1	2.128 (3)	O3—S1	1.436 (2)
O2—S1	1.473 (2)	O4—S1	1.453 (2)
O2—Co1—N1	88.92 (9)	N1—Co1—N2	83.57 (10)
O2—Co1—N2	86.40 (10)		

Table 4-2-7. Hydrogen-bond geometry (Å, ˚) for (**VIII**).

D—H···A	D—H	H···A	D···A	D—H···A
O1—H1···O4viii	0.79 (5)	2.04 (5)	2.789 (3)	159 (5)

Symmetry code: (viii) –x+1, y+1/2, -z+1/2

4-3. Poly-(μ-nitrato-O,O')[{μ_2-2,2'-dipyridyl (hydroxy) methanolato-N,N',O}-{μ-pyrazolato-N,N'}-di-pyrazol-nitrato-di-copper(ii)] mono hydrate

$[\mu_2\text{-}\{C(OH)(O)(C_5H_4N)_2\}\mu\text{-}(C_3H_3N_2)Cu_2(C_3H_4N)_2(NO_3)_2]_n$ **IX** was synthesised from equimolar quantities of aqueous 2-2'-dipyridyl ketone, pyrazole and copper nitrate in water (*Scheme 4-3-1*). After two weeks dark blue cubic crystals had formed and were analyzed by X-ray single crystal diffraction *(figure 4-3-1).* Crystallographic details are presented in *Table 4-3-3* and a fully labelled ORTEP view *Figure 4-3-1*

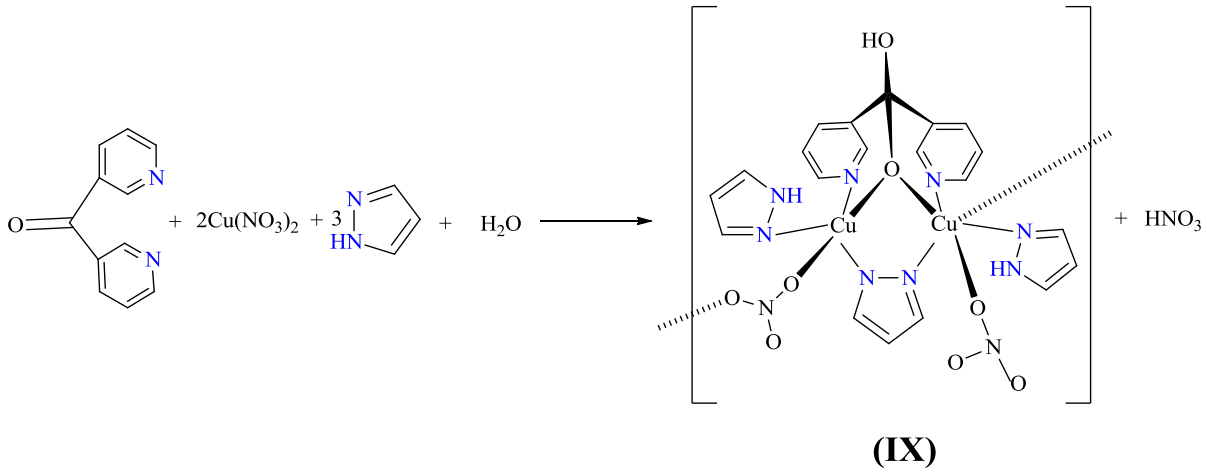

Scheme 4-3-1. Illustration of structure complex **IX**, which shows polymerised structure through the nitrato oxygen

IX forms a coordination polymer through a nitrato bridge. Although both CuN_3O_3 centres are meridional. There are significant geometric differences between them that extend

beyond their formal six and five coordination and hint at underlying electronic differences *Figure 4-3-1*.

As expected Jahn-Teller distortion is seen in both copper atoms, leading to the Cu-ONO_2 bonds being extremely elongated. In Cu2 the Jahn-Teller distorted Cu-ONO_2 bonds are significantly longer than the equivalents to Cu1, to the extent that the copper is formally five coordinate *Table 4-3-1*.

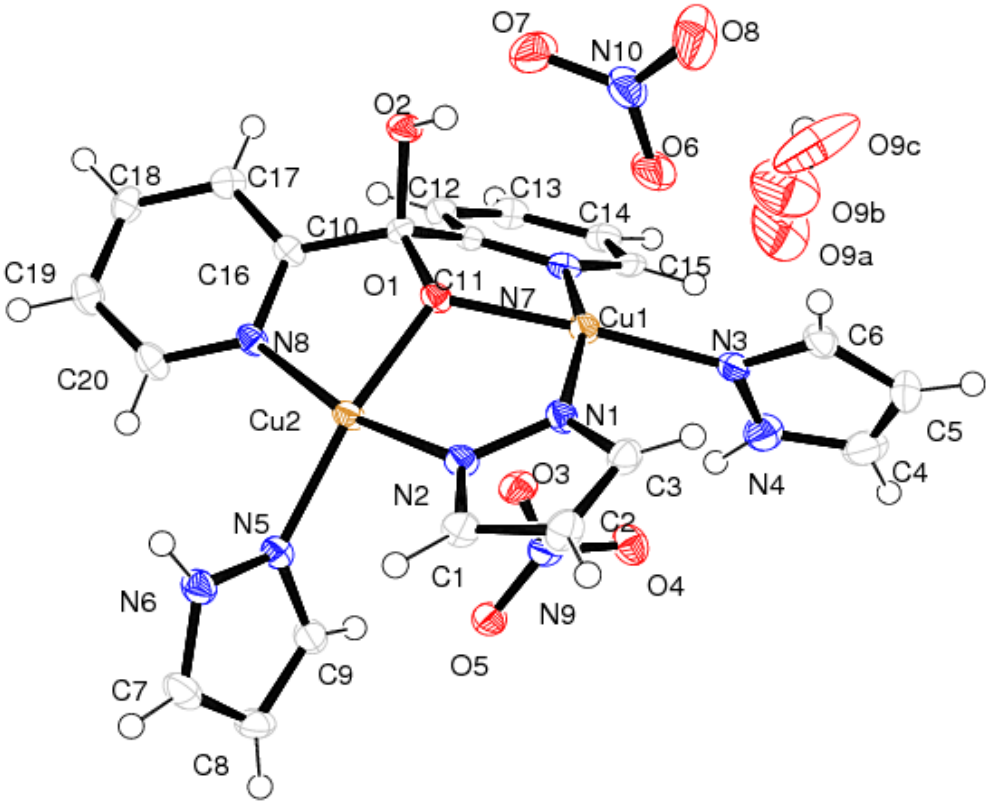

Figure 4-3-1. The structure complex of **IX** with dimer metals Cu centre.

Accompanying this change there is a contraction of the remaining bonds around Cu2, in particular those to the 2-2′-dipyridyl ligand,

suggesting that the alkoxide electron is disproportionately distributed to Cu2 relative to Cu1 *(Table 4-3-1)*.

Table 4-3-1. The table give the bond distances of copper atoms to ligands (N,O) for compound $[Cu\{C(OH)_2(C_5H_4N)_2\}_2](NO_3)_2.2H_2O$ (measurement is Å)

	Pyridyl (N)	Pyrazole (N)	Pyrazolate (N)	Alkoxide (O)	Nitrato (O6,O4)	Nitrato (O3)
Cu1	2.017(3)	1.998(3)	1.965(3)	1.941(3)	2.441(3)	2.699(3)
Cu2	1.993(3)	1.990(3)	1.957 (3)	1.929 (3)	2.522(3)	3.051(3)

Referring to *Figure 4-3-2,* the alkoxy oxygen atom, O1, participates in two strong Cu-O bonds of 1.929 (3) and 1.941 (3) Å, which bridges the two copper atoms; also a pyrazolate bridges the two copper with nitrogen atoms N1 and N2 in cis-position relative to the alkoxy oxygen atom. The bond lengths of Cu-N are 1.965 (3) and 1.957 (3) Å *(Table 4-3-1)*.

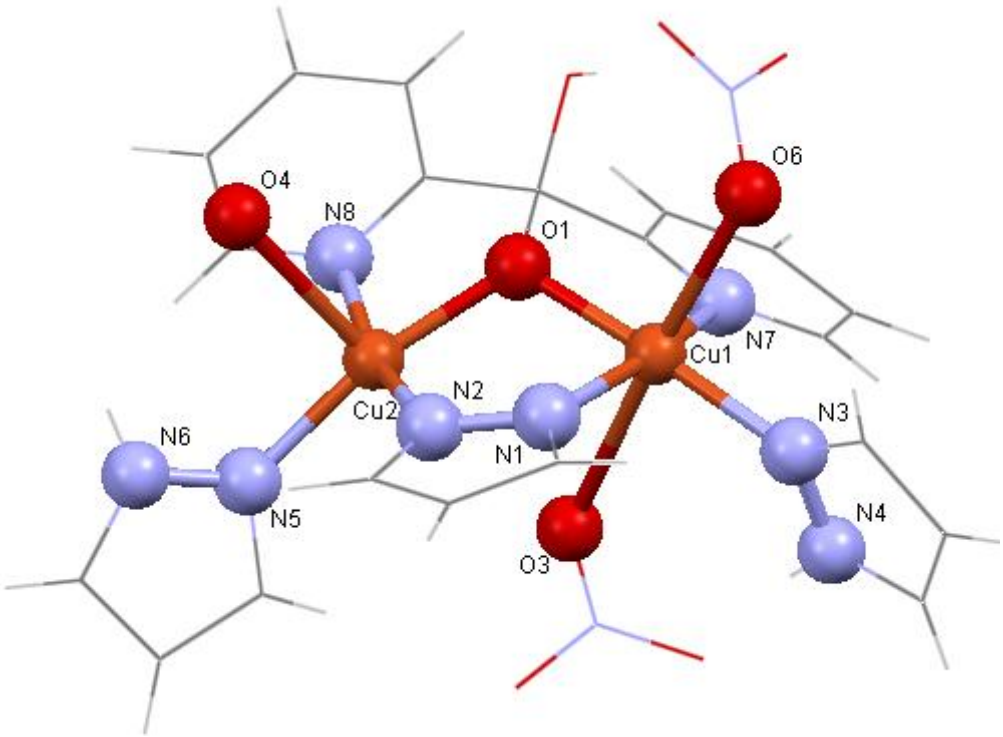

Figure 4-3-2. Illustration of Cu geometry in complex of **IX**. Above dimer farther associate into coordinate polymer via bridging nitrato group (O3 and O4)

A terminal pyrazole also coordinates to each Cu in tetragonally compressed positions [Cu1-N 1.998 (3) and Cu2-N 1.990 (3) Å] forming "wings" trans to the bridging alkoxy. They both eclipse a nitrato oxygen atom, [N-N-Cu-O 17.0˚(3), -5.3˚(3)] allowing an intermolecular N-H···ONO_2 hydrogen bond to form in each case at N···O distances of 2.838 (3) Å and 2.795 (5) Å, *(Figure 4-3-3)*. The nitrato oxygen atoms also coordinate to Cu through Jahn-Teller elongated 2.441 (3), 2.522 (3) and 2.699 (3) Å Cu-O bonds *(Table 4-3-1)*.

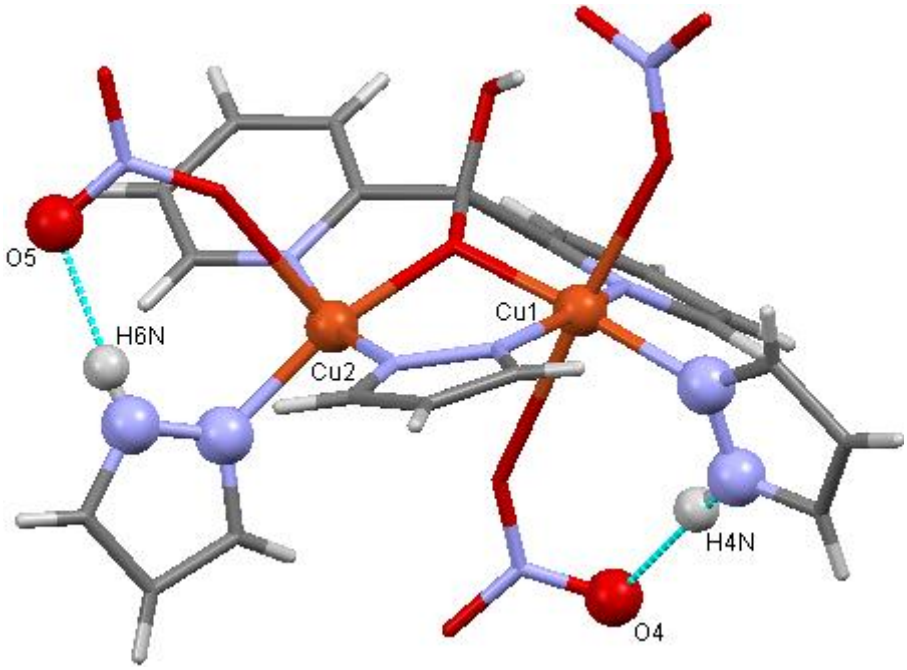

Figure 4-3-3. Illustration intra-molecular hydrogen bonding in complex of **IX**

A search of the Cambridge Crystallography Data base using Conquest and the illustrated fragment yielded 1500 compounds *(Figure 4-3-5)*. *Figure 4-3-4* shows the search fragment that has been used.

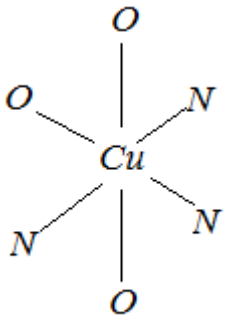

Figure 4-3-4. The conquest search fragment used to search the Cambridge Crystallography Data base for complexes which similar coordination geometry of **IX**.

The two histograms in *Figure 4-3-5* illustrate the occurrence of Cu-O and Cu-N bond lengths in octahedral CuO_3N_3 complexes.

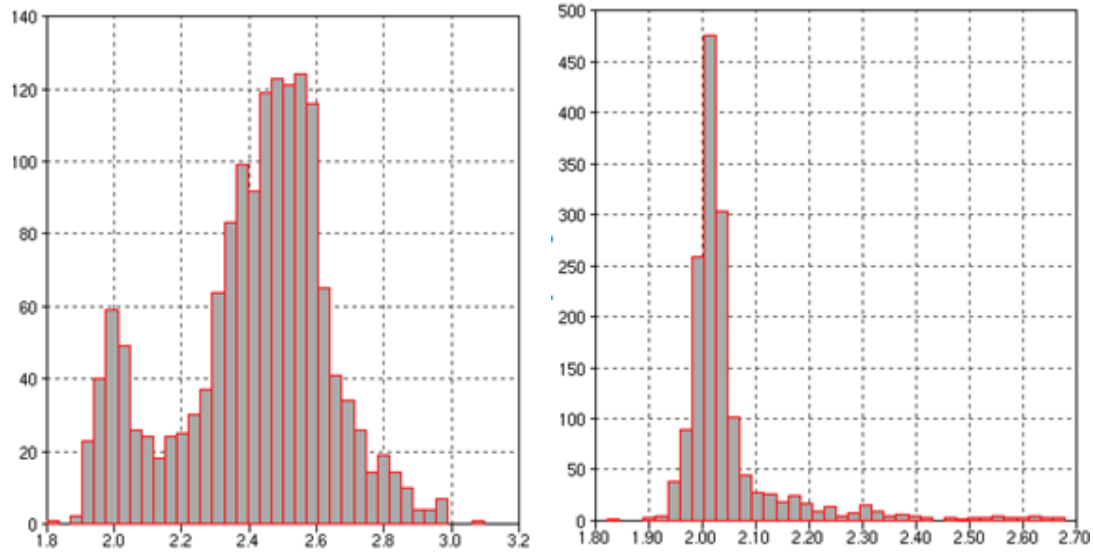

A. Histogram of Cu-O bond length in the above CuN_3O_3 fragment. **B.** Histogram of Cu-N bond length in above CuN_3O_3 fragment

Figure 4-3-5. The A & B illustrate more than 1500 compounds collected from Cambridge crystallography Data base with octahedral geometry, ONO_2 in elongated positions and nitrogen atoms in compressed positions as complex **IX** (Cu^{2+} it was chosen and the measurements are in Å)

As was noted for the CuN_4O_2 core in complex **VII** there is predominance of oxygen atoms in the Jahn-Teller elongated capping position *(Figure 4-3-5 above)*. For both nitrogen and oxygen atoms in the tetragonally compressed sites the Cu-N/O distances are approximately 2 Å, however the elongated Cu-O distance has a mean value of approximately 2.5 Å.

The Cu dimers associate into coordination polymer via bridging NO_3^-, which also participate in hydrogen bonds with pyrazole, strengthening the link between the dimers *Figure 4-3-6.*

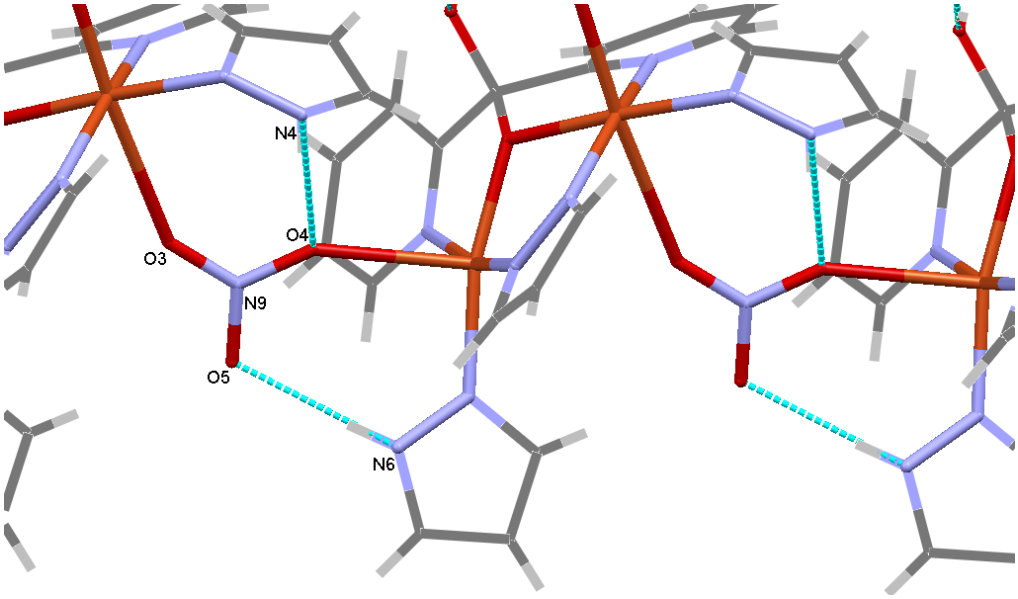

Figure 4-3-6. Hydrogen bond between pyrozle and nitrato ligands supporting Jahn Teller elongated nitrato bridges to form a polymer along the crystallographic a-axis in complex **IX**

The angles subtended at Cu involving bridging ligands show little variation between the two copper centres, however the terminal pyrazole show a greater degree of flexibility and there is a difference of 10° between the two O1-Cu-N angles [176.53º (11) and 166.96º (11)]

Table 4-3-2. Comparison of the angles of the two copper in centre with O1 and the ligands for complex **IX**

	Pyridyl (N)	Pyrazole (N)	Pyrazolate (N)
O1-Cu1-N	N7= 81.59(11)	N3= 176.53(11)	N1= 85.23(11)
O1-Cu2-N	N8= 82.36(11)	N5= 166.96(11)	N2= 85.78(11)

Adjacent coordination polymer chains are linked by hydrogen bonds between a capping nitrate and lattice water *(see Figure 4-3-7)*. This nitrate group also hydrogen bonds to the methoxy OH group.

The lattice water is disordered and partially occupies three crystallography independent sites (O9A, O9B and O9C) making a total of six sites when the crystallographic inversion operation is applied. For hydrogen bonds involving water and adjacent coordination polymer chains only one of the disordered water sites is illustrated for clarity *(see figure 4-3-7).*

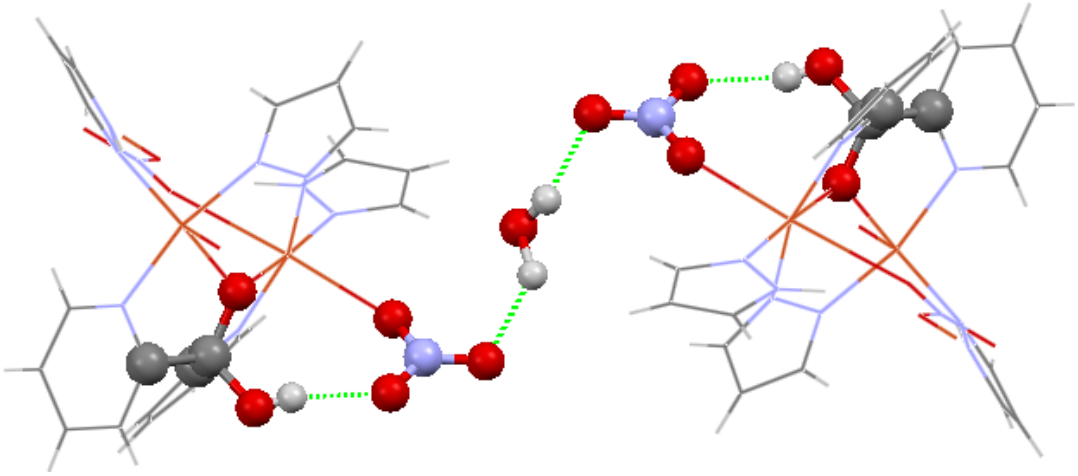

Figure 4-3-7. The structure complex of **IX** are polymerizing through the nitrato oxygen atoms. The two rows of polymer are connected by hydrogen bonding water molecule to nitrato oxygen atom.

4-3-1. Synthesis

Three separate solutions of starting materials were prepared in vials. 0.176g of 2,2′-dipyridyl ketone in 10mL water 0.1M, 0.064g of pyrazole in 10mL water 0.1M and 0.195g of $Cu(NO_3)_2$ in 10mL water (0.1M).

1ml of each of the starting materials were mixed and left standing at room temperature for two weeks. After two weeks two different

kind of crystals formed, some pale purple glassy needles and some dark blue cubes. The purple crystals were poorly formed $[Cu\{C(OH)_2(C_5H_4N)_2\}_2](NO_3)_2.2H_2O$, which has already been reported (Sumby et al 2003). The dark blue blocks were well formed and allowed easy selection of suitable crystal for full structural characterisation of complex **IX**.

Some crystallography information is provided in *Table 4-3-3.*

Table 4-3-3. crystallography data and refinement information for complex of **IX**

Chemical formula	$C_{20}H_{21}Cu_2N_{10}O_{8.50}$
M_r	664.55
Crystal system, space group	Monoclinic, $P2_1/n$
Temperature (K)	100
a, b, c (Å)	7.7105 (1), 22.4877 (4), 14.7640 (3)
β (°)	102.703 (1)
V (Å^3)	2497.29 (7)
Z	4
Radiation type	Mo $K\alpha$
μ (mm^{-1})	1.77
Crystal size (mm)	0.25 × 0.12 × 0.05
Data collection	
Diffractometer	KappaCCD diffractometer
Absorption correction	Multi-scan Blessing, R. H. (1995) Acta Cryst., A51, 33-38.
T_{min}, T_{max}	0.665, 0.917
No. of measured, independent and observed [$I > 2s(I)$] reflections	10633, 5437, 4061
R_{int}	0.055
(sin Θ/λ)$_{max}$ (Å^{-1})	0.639
Refinement	
$R[F^2 > 2\sigma(F^2)]$, $wR(F^2)$, S	0.045, 0.120, 1.09
No. of reflections	5437
No. of parameters	453
No. of restraints	18
H-atom treatment	All H-atom parameters refined
Δ›$_{max}$, Δ›$_{min}$ (e Å^{-3})	0.69, -1.05

4-4. $3[(C_{11}H_{10}N_2O_2C_2H_5)(C_3H_3N_2)_2(NO_3)_2Cu_2]_n.2(C_2H_5OH)$

$3[(C_{11}H_{10}N_2O_2C_2H_5)(C_3H_3N_2)_2(NO_3)_2Cu_2]_n.2(C_2H_5OH)$ was synthesised from 2,2′-dipyridyle ketone, pyrazole and copper nitrate in ethanol. Crystallographic details are presented in *Table4-4-6.* The asymmetric unit consist of three crystallography unique copper dimers (**X**), and two (**XI**). In each case the copper dimer are bridged by a pyrazolate, 2,2′-dipyridyl (ethanol) methanolato and nitrato. Dimers **X** and **XI** are distinguished by the way the copper atoms are bridged by the nitrate. In **X** a single nitrato oxygen bridged the copper atoms (Cu-O-Cu) but in **XI** two oxygen atoms are involved (Cu-ONO-Cu) *(Figure 4-4-2)*.

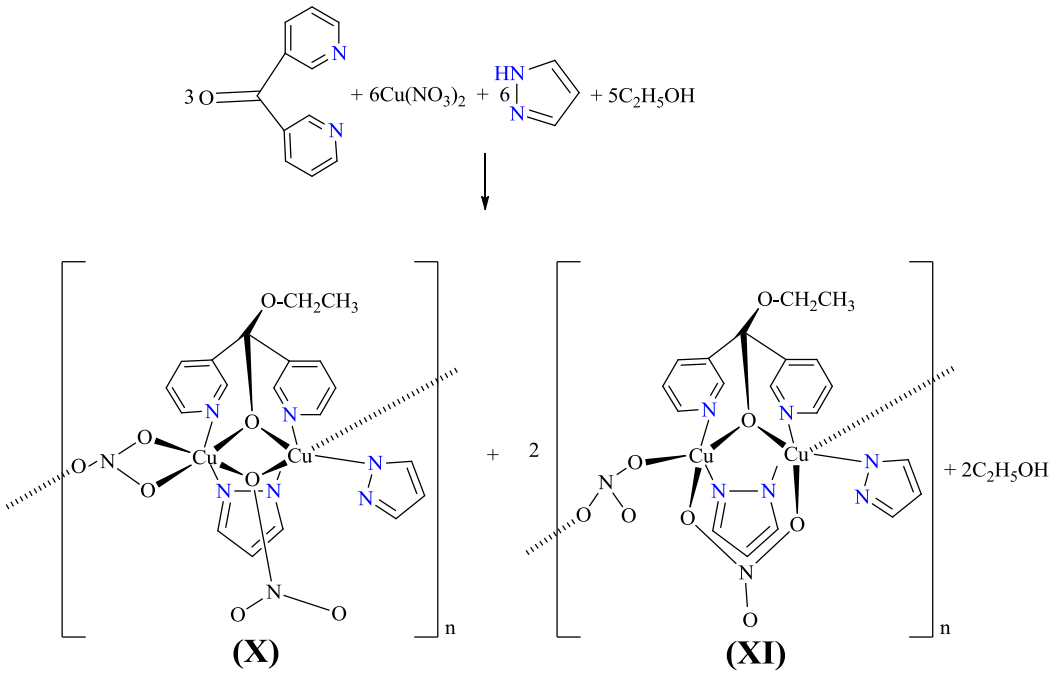

Scheme 4-4-1. In single crystal three independent structure complexes were formed with dimer Cu metals in centre, the Cu1-Cu2 complex **(X)** and the two complexes of Cu3-Cu4 and Cu5-Cu6 complex **(XI)**.

Between the two copper centre complexes of **XI** there are significant geometric differences that extend beyond their six and five coordinate geometries at underlining electronic differences.

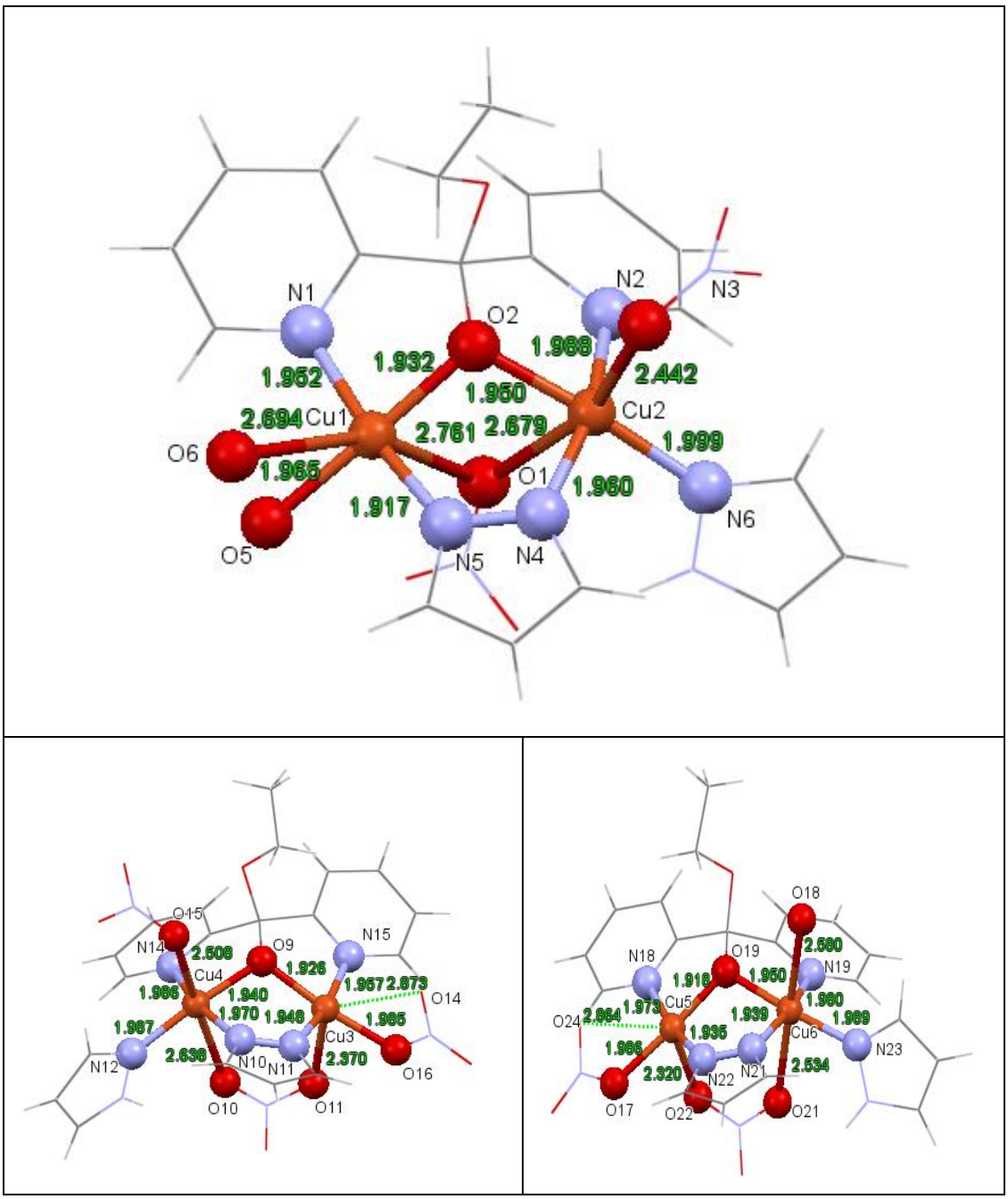

Figure 4-4-1. Three structures are identified in a single crystal by X-ray diffraction. Above illustrate the complex of **X** and below those two complexes of **XI.**

Table 4-4-1. Selected geometric parameters (Å, º) for complexes of **X**, **XI**

C1—O2	1.393 (4)	C27—O13	1.450 (3)
C1—O3	1.459 (4)	C39—O19	1.404 (3)
C27—O9	1.404 (3)	C39—O20	1.412 (4)
C9—C1—C4	116.6 (3)	Cu1—O2—Cu2	109.15 (10)
C30—C27—C26	116.4 (2)	Cu3—O9—Cu4	110.77 (10)
C46—C39—C41	113.6 (2)	Cu5—O19—Cu6	108.40 (10)
O2—Cu2—N6—N7	-26.6 (9)	O19—Cu6—N23—N24	-141.5 (13)
Cu3—Cu4—N12—N13	-49.5 (3)		

Jahn-Teller distortion is seen in both copper atoms all three crystallographically unique dimers. In Cu3 and Cu5 the J-T distorted Cu-ONO_2 bonds are significantly longer at 2.873 (3), 2.864 (3) Å than their equivalents in Cu4 and Cu6, to the extent that the copper is formally five coordinate *(Table 4-4-2)* in the former.

Table 4-4-2. The bond lengths of two Copper metals to the ligands for the structure complexes of **X**, **XI**.

	Pyridyl (N,N')	Pyrazole (N)	Pyrazolate (N,N')	Alkoxide (O,O)	Nitrato (O,O andO,O')	Nitrato (O)
Cu1**X**	1.952 (3)		1.917 (3)	1.932 (3)	2.761 (3)	1.965 (3)
Cu2**X**	1.988 (3)	1.999 (3)	1.960 (3)	1.950 (2)	2.679 (3)	2.442 (3)
Cu3**XI**	1.957 (3)		1.948 (3)	1.926 (3)	2.370 (3)	1.965 (3)
Cu4**XI**	1.986 (3)	1.987 (3)	1.970 (3)	1.940 (2)	2.638 (3)	2.581 (3)
Cu5**XI**	1.973 (3)		1.935 (3)	1.919 (3)	2.320 (3)	1.966 (3)
Cu6**XI**	1.979 (3)	1.988 (3)	1.939 (2)	1.950 (3)	2.534 (3)	2.508 (3)

A terminal pyrazole coordinates to one of the Cu centres in each of the structure complexes of **X** and **XI**, the bond length distances

of Cu2-N, Cu4-N and Cu6-N are 1.999 (3), 1.987 (3) and 1.988 (3) Å respectively.

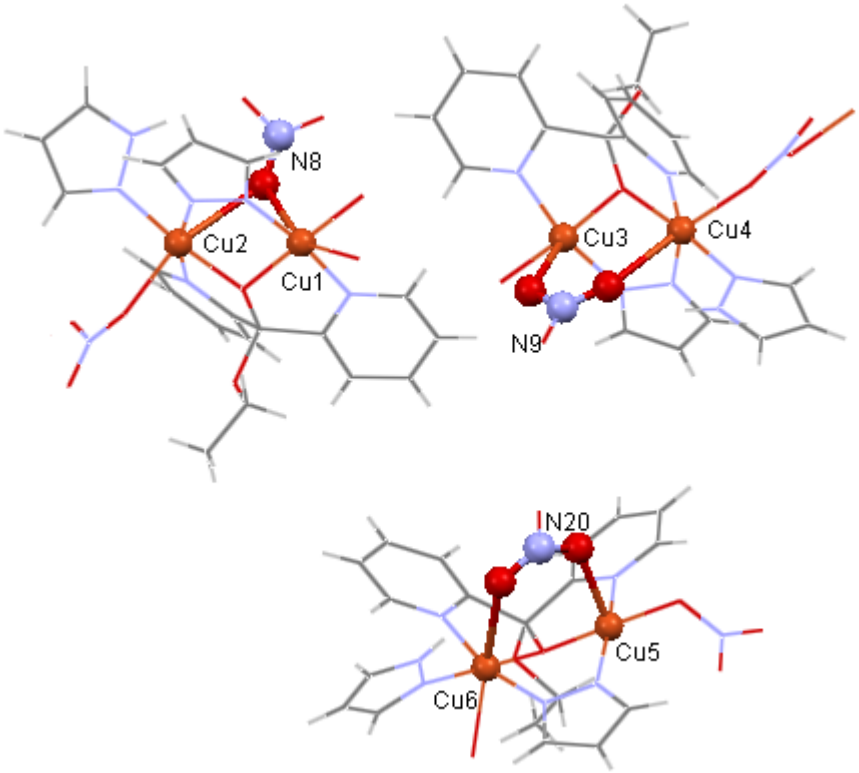

Figure 4-4-2. The nitrato ligands bridged two copper atoms in different ways in the structure complexes of **X**, **XI** (μ_2 nitrato O,O and μ_2 nitrato O,O')

A search of the Cambridge Crystallography Data base for structures that include pyrazolate bonds to copper was carried out and histogram for the distribution of Cu-N distances are presented

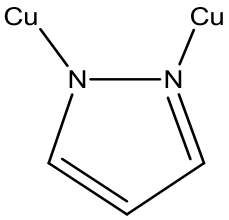

Figure 4-4-3 (A,B).

In *Figure 4-4-3 (A,B)* shows the average bond length distance of Cu-N 1.948 Å. The average bond length distances for Pyrazolate to Cu is 1.944 Å for complexes of **X** and **XI** which agrees well with the average literature value.

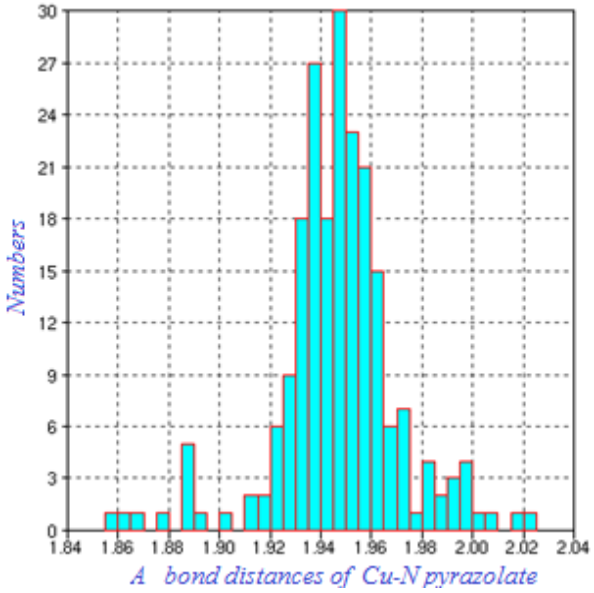

Figure 4-4-3. Disterbution of Cu-N bond lengths to bridged pyrazolate

From the Cambridge Crystallography Data base a search was carried out for the bond length distances of Pyrazole to Cu, the average bond distance of Cu-N is 1.997 Å *(Figure 4-4-4)*. The average bond distances Cu centre to pyrazole is 1.991 Å for complexes **X** and **XI**.

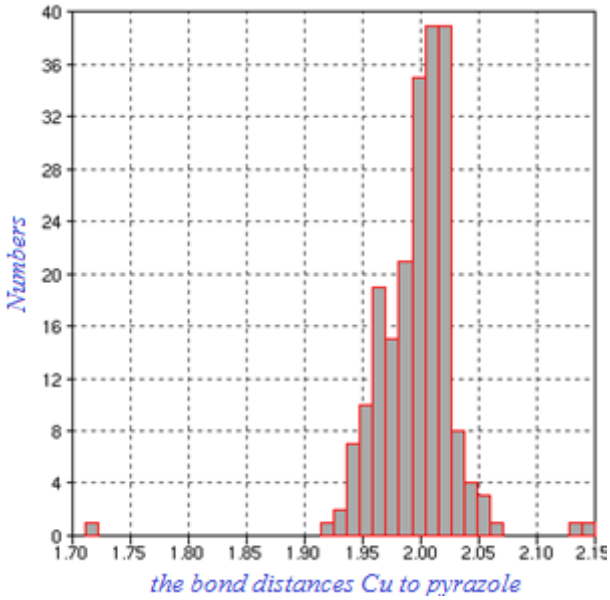

Figure 4-4-4. The Cu^{2+} bond distances to pyrazole collected from Cambridge Crystallography Data base

The hydrogen bond distance between the nitrato oxygen and pyrazole hydrogen H7A· · ·O8 in the structure complex of **X** is 1.943 (3) Å, this is the shortest hydrogen bond length distance in all the complexes **X** and **XI**. The distance between the two copper centres of **X** is 3.163 (3) Å *(Figure 4-4-5)*.

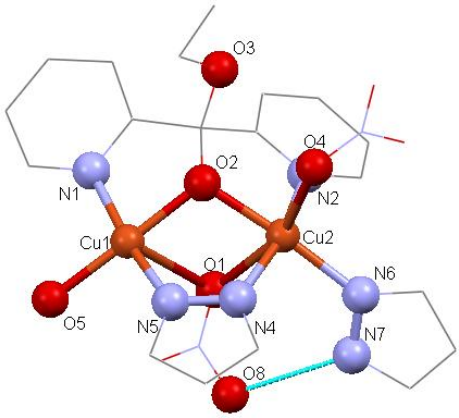

Figure 4-4-5. This illustrates the structure complex of **X**, which μ_2-nitrato-O,O bridged two copper atoms, also illustrate the hydrogen bond between oxygen' nitrato and pyrazole (H7A···O8), this is the shortest hydrogen bond in all the structure complexes **X** and **XI**

Table 4-4-3 displays some of the angles of ligand-Cu-ligand for complex of **X**. The angle between two elongated nitrato oxygen atoms O4-Cu2-O1 is 162.3 (8)˚.

Atoms (compressed positions)	Angles/ °	Atoms (elongated positions)	Angles/ °
N5-Cu1-O5	92.3 (1)	O1-Cu1-N5	84.44 (9)
O5-Cu1-N1	94.87 (9)	O1-Cu1-O5	103.35 (8)
N1-Cu1-O2	82.72 (9)	O1-Cu1-N1	96.50 (9)
O2-Cu1-N5	90.16 (9)	O1-Cu1-O2	75.33 (8)
N4-Cu2-N6	91.3 (1)	O1-Cu2-N4	85.83 (9)
N6-Cu2-N2	97.40 (9)	O1-Cu2-N6	96.01 (9)
N2-Cu2-O2	81.28 (9)	O1-Cu2-N2	79.83 (9)
O2-Cu2-N4	88.5 (1)	O1-Cu2-O2	77.16 (8)
		O4-Cu2-N4	92.07 (9)
		O4-Cu2-N6	101.61 (9)
		O4-Cu2-N2	99.36 (9)
		O4-Cu2-O2	85.23 (8)
		O4-Cu2-O1	162.30 (8)

A-Angles from compress positions **B**- Angles from elongate positions

Table 4-4-3. The angles for the complex of **X** are displayed. In *Figure 4-3-5.* ***A*** and **B** shows the angles for compressed and elongated positions respectively, also there is two elongated nitrato oxygen (O4-Cu2-O1)atoms angle is 162.30(8)˚

Figure 4-4-8 illustrate the complex of **XI**, The distance between the two copper centre, is 3.182 (3) Å. The angles of ligand-Cu-ligand are displayed in *Table 4-4-4*. The angle between two elongated nitrato oxygen atoms is O15-Cu4-O10 173.59 (7)˚.

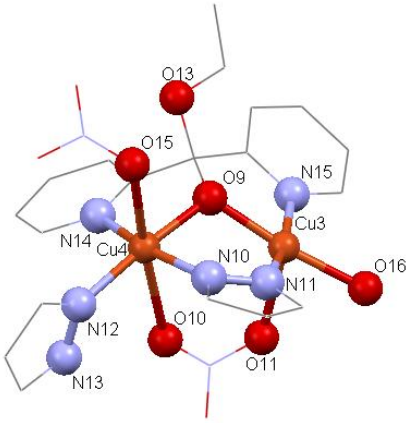

Figure 4-4-6. Complex of **XI**, clearly show the μ_2 nitrato O,O′ bridged the two copper atoms

Atoms (compressed positions)	Angles/ °	Atoms (elongated positions)	Angles/ °
N11-Cu3-O16	94.91 (9)	O11-Cu3-N11	96.54 (8)
O16-Cu3-N15	95.53 (9)	O11-Cu3-O16	75.83 (8)
N15-Cu3-O9	81.48 (9)	O11-Cu3-N15	93.57 (8)
O9-Cu3-N11	87.31 (9)	O11-Cu3-O9	110.13 (8)
N10-Cu4-N12	95.28 (9)	O10-Cu4-N10	90.64 (8)
N12-Cu4-N14	96.83 (9)	O10-Cu4-N12	81.88 (8)
N14-Cu4-O9	82.01 (9)	O10-Cu4-N14	81.36 (8)
O9-Cu4-N10	84.89 (9)	O10-Cu4-O9	91.95 (8)
		O15-Cu4-N10	82.97 (8)
		O15-Cu4-N12	98.07 (8)
		O15-Cu4-N14	104.99 (8)
		O15-Cu4-O9	88.07 (7)
		O15-Cu4-O10	173.59 (7)

C-Angles from compress positions **D**- Angles from elongate positions

Table 4-4-4. The angles for the complex of **XI** are displayed. In *Figure 4-3-6.* **C** and **D** shows the angles for compressed and elongated positions respectively, also there is two elongated nitrato oxygen atoms angle is 173.59 (7)˚

Figure 4-4-7 illustrates complex **XI**. The distance between the two copper centres is 3.138 (2) Å. In *Table 4-4-5* the angles for ligand-

Cu-ligand are displayed, the angle between two elongated nitrato oxygen atoms is O21-Cu6-O18 177.25 (7)˚.

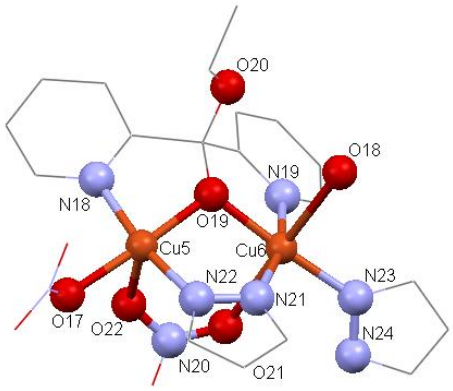

Figure 4-4-7. Illustration of the complex of **XI** which shows the μ_2 nitrato O,O' bridged two copper atoms

Atoms (compressed positions)	Angles/ °	Atoms (elongated positions)	Angles/ °
N22-Cu5-O17	93.17 (9)	O22-Cu5-N22	100.59 (9)
O17-Cu5-N18	95.91 (9)	O22-Cu5-O17	79.34 (8)
N18-Cu5-O19	82.24 (9)	O22-Cu5-N18	86.48 (9)
O19-Cu5-N22	88.45 (9)	O22-Cu5-O19	102.89 (8)
N21-Cu6-N23	96.5 (1)	O21-Cu6-N21	86.78 (9)
N23-Cu6-N19	95.3 (1)	O21-Cu6-N23	83.63 (9)
N19-Cu6-O19	81.65 (9)	O21-Cu6-N19	84.87 (9)
O19-Cu6-N21	86.87 (9)	O21-Cu6-N19	98.53 (8)
		N21-Cu6-O18	90.91 (8)
		O18-Cu6-N23	95.16 (9)
		O18-Cu6-N19	97.72 (9)
		O18-Cu6-O19	82.83 (8)
		O21-Cu6-O18	177.25 (7)

E- Angles from compressed positions **F**- Angles from elongated positions

Table 4-4-5. The angles for complex of **XI** are displayed. In *Figure 4-3-7.* **E** and **F** shows the angles for compressed and elongated positions respectively, also there is two elongated nitrato oxygen atoms angle is 177.25 (7)˚

4-4-1. Synthesis

Three separate solutions of starting materials were prepared in vials. 0.176g of 2,2′-dipyridyl ketone in 10mL ethanol (0.1M), 0.064g of pyrazole in 10mL ethanol (0.1M) and 0.195g of $Cu(NO_3)_2$ in 10mL ethanol (0.1M).

1mL of each of the three solutions above were mixed together, this was covered and allowed to stand at room temperature. The next day dark blue cubic crystals formed. When the crystals were left for another day purple needles started to form and eventually covered the cubic crystals completely. After a further two weeks, the pom-pom shaped cluster was covered by small, light bluish needles. One of the blue needles was selected for full structural characterisation from which the complexes **X** and **XI** have been identified. *$3[(C_{11}H_{10}N_2O_2C_2H_5)(C_3H_3N_2)_2(NO_3)_2Cu_2]_n\ (C_2H_5OH)$*.

Crystallographic data is presented in *Table 4-4-6*.

Table 4-4-6. Crystallography data for the complexes of **X** and **XI** are collected

Chemical formula	$C_{67}H_{53}Cu_6N_{24}O_{26}$
M_r	3842.29
Crystal system, space group	Monoclinic, *C*2
Temperature (K)	100
a, *b*, *c* (Å)	34.69 (3), 7.945 (7), 27.83 (3)
β (°)	94.134 (18)
V (Å^3)	7650 (13)
Z	2
Radiation type	Cu *K*α
μ (mm^{-1})	2.63
Crystal size (mm)	0.15 × 0.1 × 0.1
Diffractometer	Bruker *APEX*-II CCD diffractometer
Absorption correction	Multi scan
No. of measured, independent and observed [$I > 2s(I)$] reflections	77243, 10352, 7539
R_{int}	0.163
σ_{max} (°)	59.1
$(\sin \Theta/\lambda)_{max}$ (Å^{-1})	0.556
$R[F^2 > 2\sigma(F^2)]$, $wR(F^2)$, S	0.064, 0.150, 1.02
No. of reflections	10352
No. of parameters	1057
No. of restraints	1
H-atom treatment	H atoms treated by a mixture of independent and constrained refinement
	$w = 1/[\sigma^2(F_o^2) + (0.0481P)^2 + 66.4035P]$ where $P = (F_o^2 + 2F_c^2)/3$
$(\Delta/\sigma)_{max}$	0.348
$\Delta\rho_{max}$, $\Delta\rho_{min}$ (e Å^{-3})	0.76, -0.69
Absolute structure	Flack H D (1983), Acta Cryst. A39, 876-881
Absolute structure parameter	0.00 (4)

4-5. $(C_{11}H_8N_2OSO_3)_2(NO_3)_2Pr_2(H_2O)_n$

Two types of crystals, one yellow and the other red, were obtained by mixing of $Pr(NO_3)_3$, 2,2′-dipyridyl ketone and $Na_2(SO_3)$ in water and standing at room temperature. The structure determination of a pale yellow crystals is described in the remainder of this section. It's chemical structure is illustrated in *Scheme 4-5-1* and an ORTEP view is presented in *Figure 4-5-1*. Crystal details are presented in *Table 4-5-3* and selected bond lengths and angles in *Table 4-5-1*. The distance between the two Pr...Pr atoms of 4.0598 (8) Å is 1.78 Å below the sum of their Van der Waals radii.

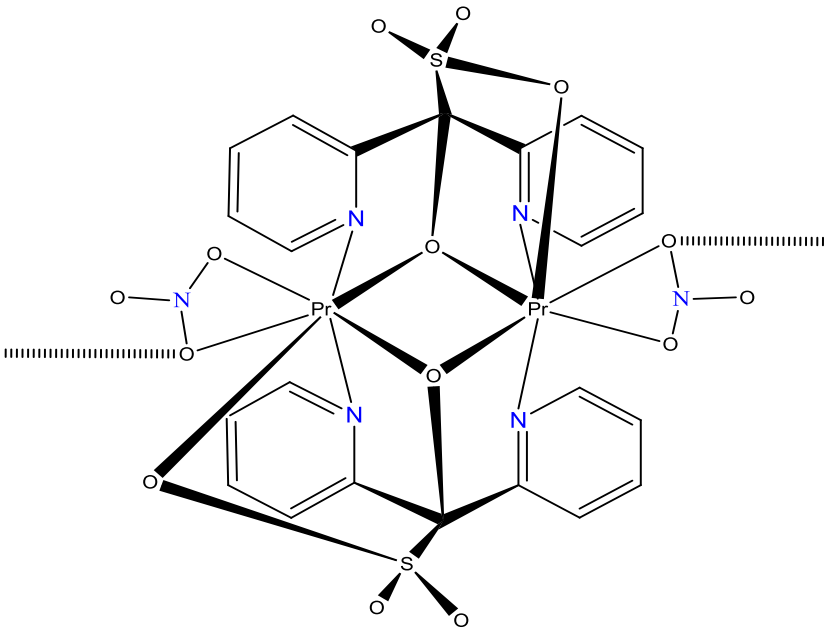

(XIII)

Scheme 4-5-1. Illustration of the structure complex of **XIII**. The coordination polymer compound was formed through the nitrato oxygen atoms.

A crystallographic inversion centre sits between the two Pr atoms in the dimer. Furthermore the NO_3^-, which links the Pr dimers into

a coordination polymer also lies close to a crystallographic inversion point and is therefore disordered over two sites.

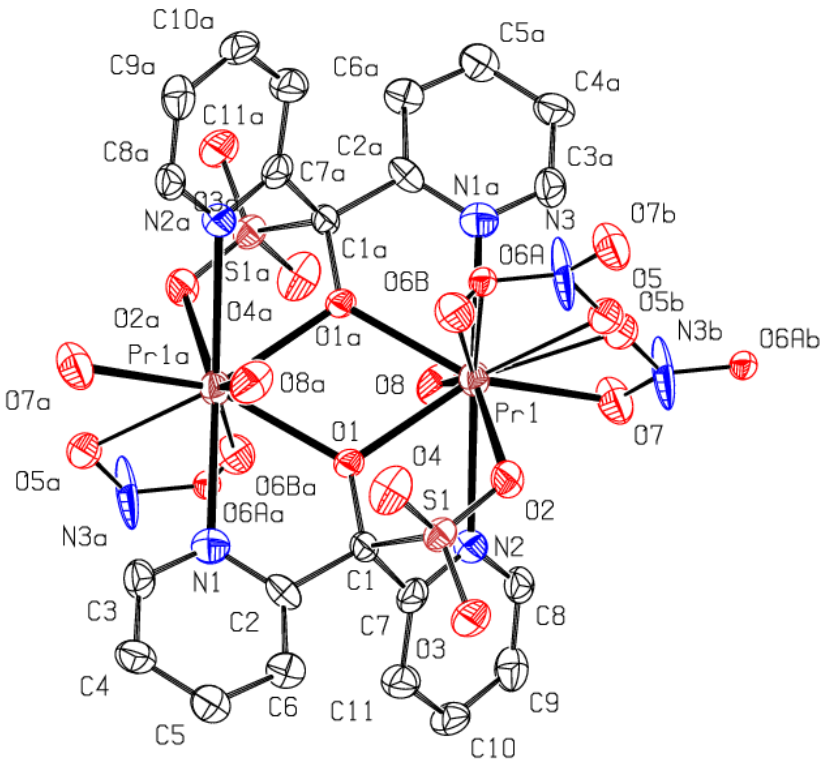

Figure 4-5-1. In complex of **XIII** each Pr coordinated to nine atoms. The bridging nitrate is disordered over an inversion point. Half the time it is replaced by a H_2O, OH hydrogen bonding bridge. The 3H atoms associated with the disorder could not be seen and were omitted from the refinement.

Referring to *Figure 4-5-2* two symmetry related alkoxy oxygen atoms, O1 bridged the Pr atoms via strong Pr-O bonds of 2.397 (5) and 2.444 (5) Å

Table 4-5-1. Selected geometric parameters (Å, º) for complex of **XIII**

C1—O1	1.377 (8)	O2—S1	1.467 (6)
C1—S1	1.869 (7)	O2—Pr1	2.529 (5)
N1—Pr1^{i}	2.663 (6)	O3—S1	1.452 (5)
N2—Pr1	2.705 (6)	O4—S1	1.471 (6)
N3—Pr1^{ii}	2.950 (14)	O5—Pr1	2.54 (2)
N3—Pr1	2.993 (15)	O5—Pr1^{ii}	2.55 (2)
O1—Pr1^{i}	2.397 (5)	O6A—Pr1	2.637 (10)
O1—Pr1	2.444 (5)		
C7—C1—C2	115.5 (6)	Pr1^{i}—O1—Pr1	113.97 (19)
C1—O1—Pr1^{i}	129.6 (4)	S1—O2—Pr1	120.3 (3)
C1—O1—Pr1	116.4 (4)	O1^{i}—Pr1—O1	66.03 (19)

Symmetry codes: (i) -*x*+1, -*y*+1, -*z*; (ii) -*x*+2, -*y*+1, -*z*.

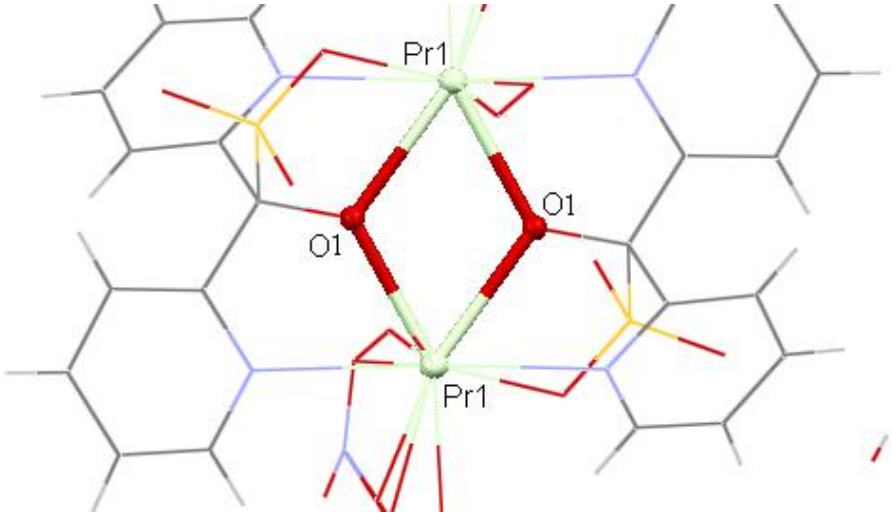

Figure 4-5-2. Two metal in centre are bridged by two oxygen O1 in complex of **XIII**

Each Pr is nine coordinate, two 2,2′-dipyridyl N atoms, and seven O atoms *Table 4-5-2*.

Table 4-5-2. The distances of atoms coordinate to Pr metal in centre for complex of **XIII**.

Pri -N1	2.663 (6)	Pr-O5 $_{Nitrate}$	2.54 (2)
Pr-N2	2.705 (6)	Pr-O6 $_{Nitrate}$	2.637 (10)
Pri-O1	2.397 (5)	Pr-O7$_{Nitrate}$	2.501 (6)
Pr-O1	2.444 (5)	Pr-O8$_{water}$	2.496 (7)
Pr-O$_{solphate}$	2.529 (5)		

The three sulfite SO bond lengths are 1.450 (6), 1.474 (8) 1.470 (7) Å *Figure 4-5-3*. The last bond length involves the oxygen which bonds to the Pr atom Pr—O, 2.527 (4) Å and surprisingly, is not the longest SO bond.

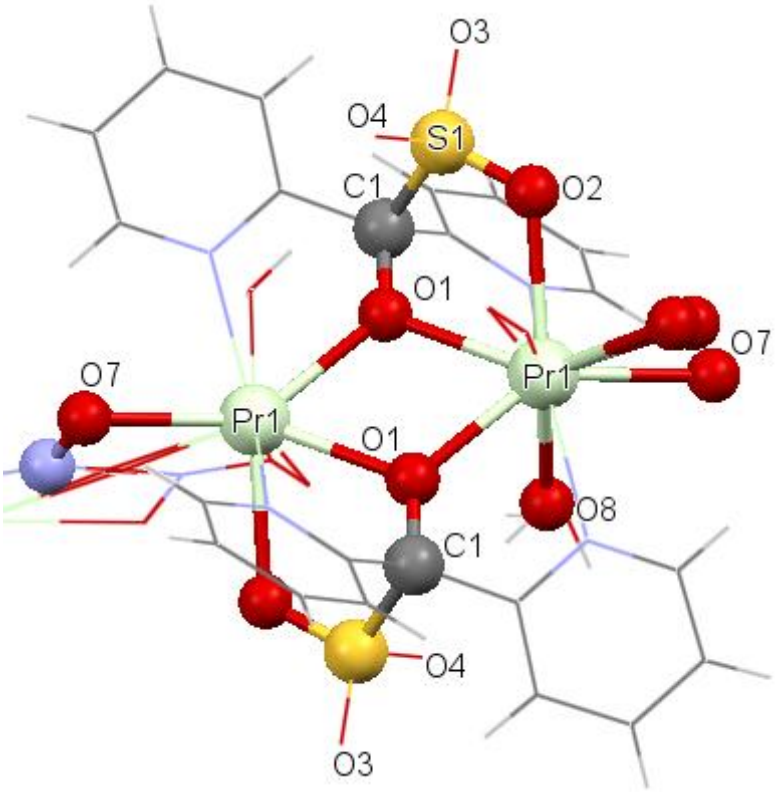

Figure 4-5-3. Illustration of the structure complex of **XIII**, showing some of the oxygen atoms bonded to metals.

The coordination polymer chains are linked by hydrogen bonds via lattice water *(Figure 4-5-5).*

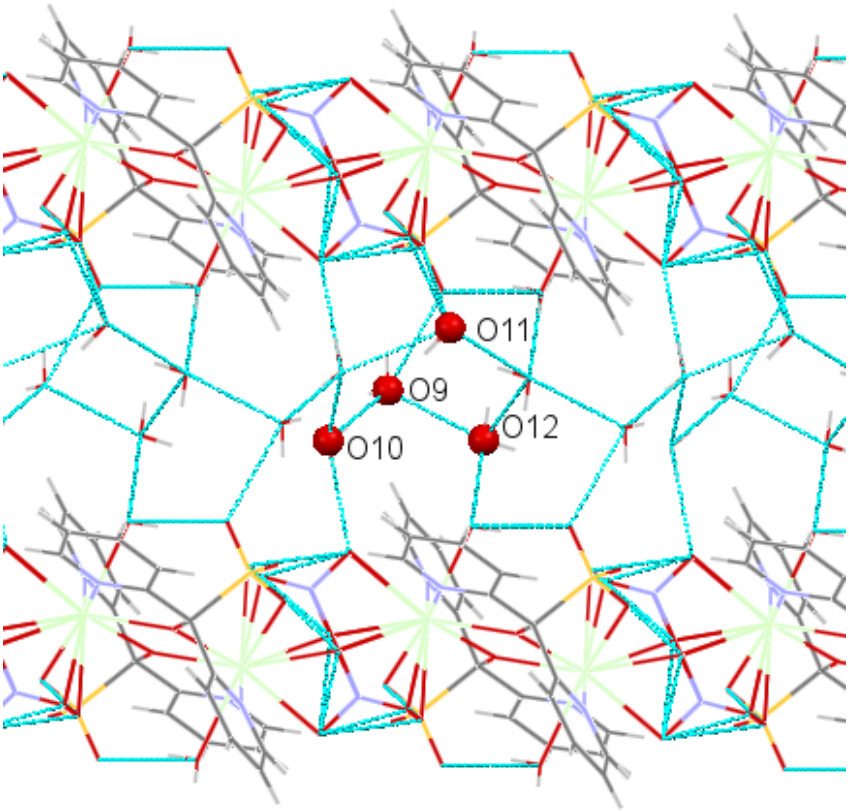

Figure 4-5-5. The hydrogen boning to lattice water in **XIII**

4-5-1. Synthesis

Stock solutions were prepared as follows; 0.176g of 2,2′-dipyridyl ketone in 10ml water (0.1M), 0.468g of $Pr(NO_3)_3$ in 10ml water (0.1M), 0.126g of $Na_2(SO_3)$ in 10ml water (0.1M).

1ml of each of above three solutions were mixed together, covered and allowed stand in room temperature for three days. When no crystals appeared the lid was removed and the solution allowed to stand for a further three days whereupon pale yellow crystals appeared by slow evaporation.

Table 4-5-3. Crystallography data of complex **XIII**

Chemical formula	$C_{22}H_{24}N_5O_{17}Pr_2S_2$
M_r	1087.21
Crystal system, space group	Triclinic, *P* -1
Temperature (K)	100
a, *b*, *c* (Å)	8.7027 (3), 11.0165 (3), 11.5080 (4)
α, β, γ (°)	66.326 (1), 89.558 (1), 70.169 (2)
V (Å^3)	939.90 (5)
Z	1
Radiation type	Mo *K*α
μ (mm^{-1})	2.77
Crystal size (mm)	0.14 × 0.08 × 0.05
Diffractometer	KappaCCD diffractometer
Absorption correction	Multi-scan Blessing, R. H. (1995) Acta Cryst., A51, 33-38.
T_{min}, T_{max}	0.698, 0.874
No. of measured, independent and observed [$I > 2\sigma(I)$] reflections	7075, 3685, 2963
R_{int}	0.077
(sin Θ/λ)$_{max}$ (Å^{-1})	0.617
$R[F^2 > 2\sigma(F^2)]$, $wR(F^2)$, S	0.052, 0.118, 1.06
No. of reflections	3685
No. of parameters	295
No. of restraints	30
H-atom treatment	H atoms treated by a mixture of independent and constrained refinement
	$w = 1/[s^2(F_o^2) + (0.0001P)^2 + 11.5785P]$ where $P = (F_o^2 + 2F_c^2)/3$
$\Delta\rho_{max}$, $\Delta\rho_{min}$ (e Å^{-3})	1.32, -1.23

4-6. $(C_{11}H_8N_2OSO_3)_2Pr_2(SO_3)_2(H_2O)_n$

The structure determination of the pale red crystals introduced in the previous section is now described. In this case the nitrato group that bridges the Pr dimers into a coordination polymer has been replaced by sulfate anions, which formed by air-oxidation of the SO_3^{2-} ions *(Scheme 4-6-1, Figure 4-6-1).* Crystal details are reported in *Table 4-6-2* and selected bond lengths and angles in *Table 4-6-1.* The two Pr metals are separated by 4.0536 (5) Å and bridged by two oxygen and four nitrogen atoms from two μ_2-bis(2-pyridyl)-sulfonatomethanolato-N,N',O,O'ligands.

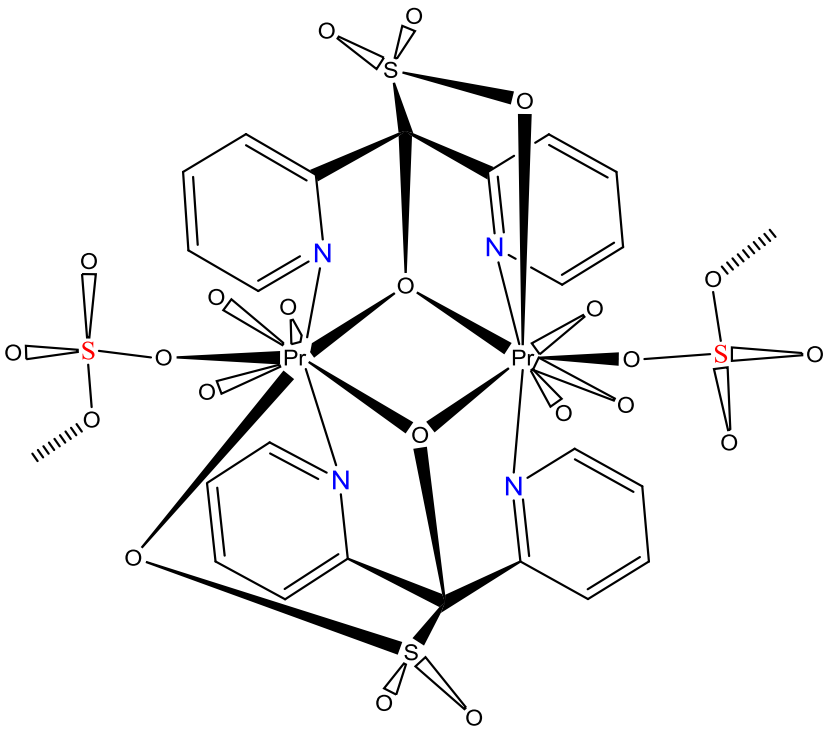

(XIV)

Scheme 4-6-1. Dimer XIV nine coordinate to ligands.

Like the nitro analogue, the two Pr in dimer **XIV** are related by a crystallographic inversion centre. Also the sulfate anion is disordered over two sites but, in contrast to **XIII**, does not link the dimers with a coordination polymer but instead associates adjacent dimers with hydrogen bonded chains.

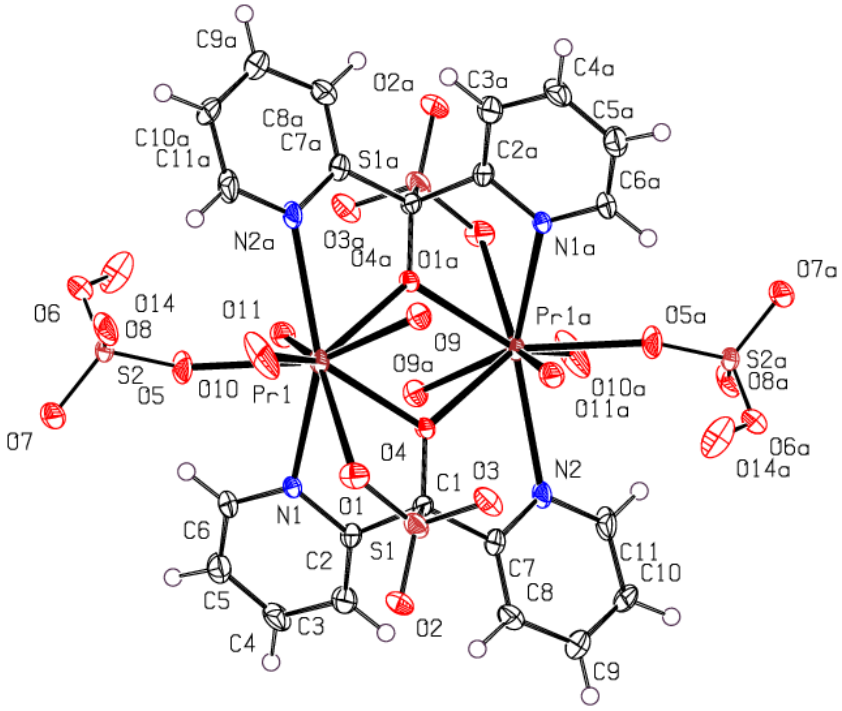

Figure 4-6-1. Illustration of structure complex of **XIV** which is formed in space group P-1

Table 4-6-1. Selected geometric parameters (Å, º) for complex of **XIV**

C1—O1	1.383 (2)	O4—S1	1.461 (5)
C1—S1	1.853 (2)	O1—Pr1^{i}	2.418 (4)
N1—Pr1	2.693 (5)	O1—Pr1	2.424 (4)
N2—Pr1^{i}	2.656 (5)	O5—Pr1	2.536 (5)
O2—S1	1.461 (5)	O6—Pr1	2.556 (5)
O2—Pr1	2.535 (5)	O8—S2	1.458 (10)
O3—S1	1.445 (5)		
O1—C1—C2	110.75 (13)	C1—O1—Pr1	117.49 (9)
S1—O2—Pr1	121.13 (7)	Pr1^{i}—O1—Pr1	113.70 (5)
C1—O1—Pr1^{i}	128.44 (9)	O1^{i}—Pr1—O1	66.30 (5)

Symmetry code: (i) -x+1, -y+1, -z+2.

Each Pr centre in complex of **XIV** is a nine coordinate three-face centred trigonal prism.

4-6-1. Synthesis

For the preparation of **XIV** see synthesis of complex **XIII**.

Table 4-6-2. Collection of some crystallography data for complex of **XIV**

Chemical formula	$C_{22}H_{42}N_4O_{25}Pr_2S_3$
M_r	1140.6
Crystal system, space group	Triclinic, *P* -1
Temperature (K)	100
a, *b*, *c* (Å)	8.3697 (6), 10.7385 (7), 11.2969 (7)
α, β, γ (°)	108.883 (6), 94.706 (5), 97.788 (5)
V (Å^3)	943.21 (11)
Z	1
Radiation type	Mo *K*α
μ (mm^{-1})	2.82
Crystal size (mm)	0.15 × 0.09 × 0.04
Diffractometer	Xcalibur, Sapphire2, large Be window diffractometer
Absorption correction	Multi-scan *CrysAlis PRO*, Agilent Technologies, Version 1.171.35.19 (release 27-10-2011 CrysAlis171 .NET) (compiled Oct 27 2011,15:02:11) Empirical absorption correction using spherical harmonics, implemented in SCALE3 ABSPACK scaling algorithm.
T_{min}, T_{max}	0.677, 0.896
No. of measured, independent and observed [$I > 2\sigma(I)$] reflections	5736, 3903, 3277
R_{int}	0.058
$(\sin \Theta/\lambda)_{max}$ (Å^{-1})	0.628
$R[F^2 > 2s(F^2)]$, $wR(F^2)$, S	0.050, 0.121, 1.06
No. of reflections	3903
No. of parameters	287
No. of restraints	0
H-atom treatment	H-atom parameters constrained
$\Delta\rho_{max}$, $\Delta\rho_{min}$ (e Å^{-3})	1.88, -1.49

4-7. $[(C_{11}H_8N_2OH)\ OCH_3]_2\ LnCl_2,\ Cl$ {Ln = Dy, Ho, Er and Yb}

2,2′-dipyridyl ketone, pyrazole and trivalent lanthanides ions were reacted in methanol in the hope of producing a complexe with a tetrapodal ligand. The resulting solutions were subjected to vapour diffusion using diethyl ether as the anti-solvent and produced crystals of the above monomeric isostructural complexes instead *(Scheme 4-7-1; Figure 4-7-1)*.

Crystals details are presented in *Table 4-7-5* and selected bond lengths and angles in *Tables 4-7-1 to 4-7-4*.

The eight coordinate square anti prism coordination shell around each lanthanide does not include a pyrazole. Methanol proved to be the more affective as nucleophile, in this case. As anticipated, the bonds lengths to each lanthanide decrease as atomic number climbs *Figure 4-7-2.*

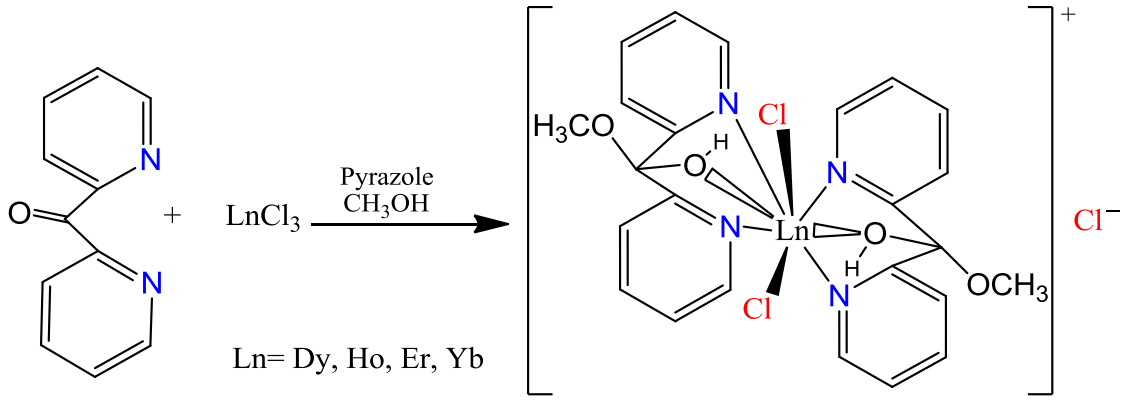

(XV, XVI, XVII, XVIII)

Scheme 4-7-1. The structure complexes have the same configurations, the Ln used for structure complexes are Dy = **XV**, Ho = **XVI**, Er = **XVII** and Yb = **XVIII**

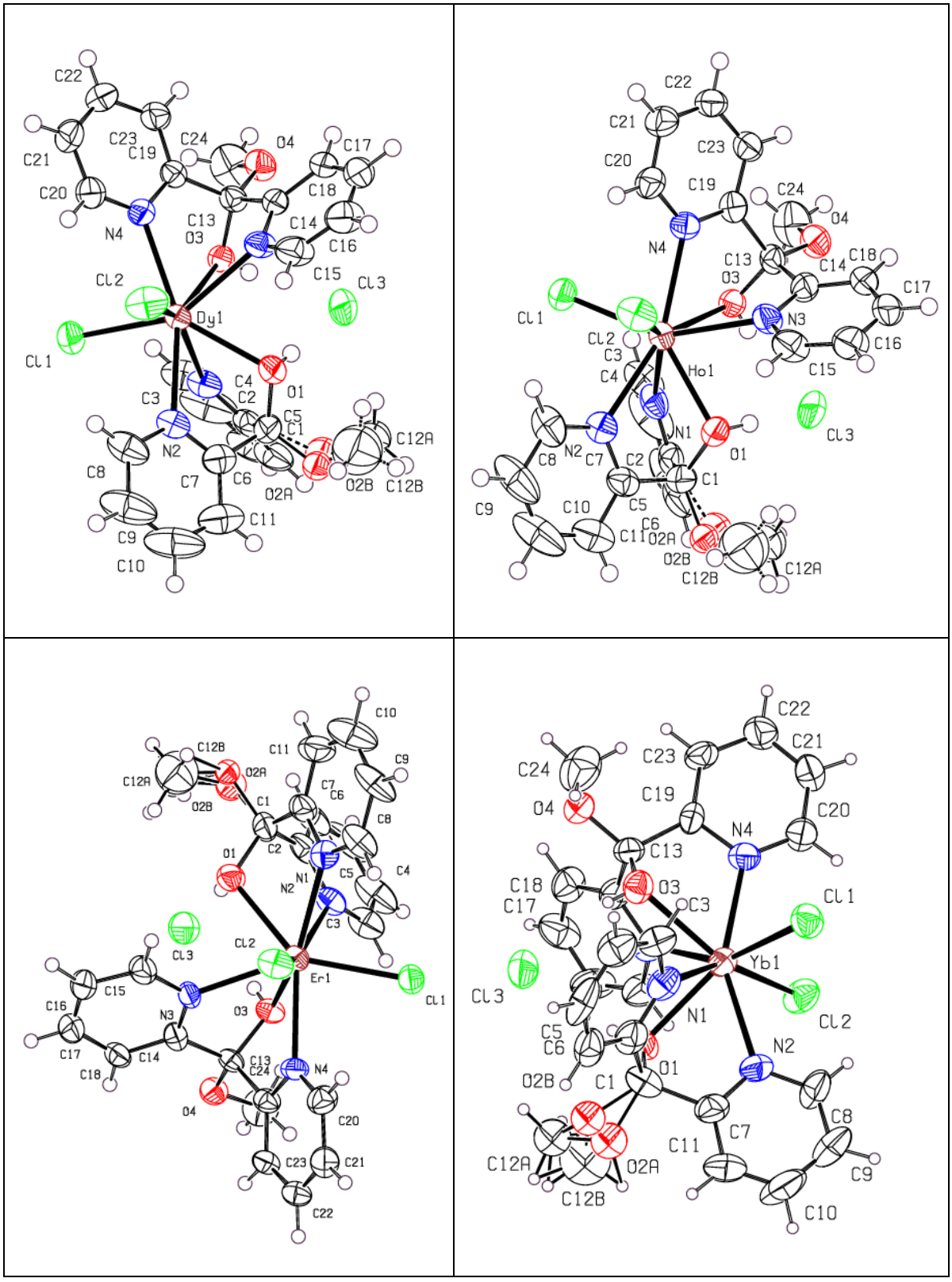

Figure 4-7-1. Illustration of complexes **XV**, **XVI**, **XVII** and **XVIII**. All have disorder around the methanol.

Table 4-7-1. Selected geometric parameters (Å, º) for complex of **XV**

C1—O1	1.434 (4)	O1—Dy1	2.441 (2)
N1—Dy1	2.555 (3)	O3—Dy1	2.439 (2)
N2—Dy1	2.530 (2)	Cl1—Dy1	2.6171 (8)
N3—Dy1	2.564 (3)	Cl2—Dy1	2.6097 (8)
N4—Dy1	2.502 (2)		
O1—C1—O2A	112.0 (3)	Cl2—Dy1—Cl1	96.77 (3)
O1—C1—C7	105.9 (3)		

Table 4-7-2. Selected geometric parameters (Å, º) for complex of **XVI**

C1—O1	1.437 (7)	O1—Ho1	2.429 (4)
N1—Ho1	2.541 (5)	O3—Ho1	2.423 (4)
N2—Ho1	2.503 (5)	Cl1—Ho1	2.6065 (15)
N3—Ho1	2.545 (5)	Cl2—Ho1	2.6026 (14)
N4—Ho1	2.481 (5)		
O1—C1—O2A	111.2 (6)	Cl2—Ho1—Cl1	96.61 (5)
O1—C1—C7	106.6 (5)		

Table 4-7-3. Selected geometric parameters (Å, º) for complex **XVII**

C1—O1	1.445 (12)	O1—Er1	2.410 (7)
N1—Er1	2.526 (8)	O3—Er1	2.408 (6)
N2—Er1	2.495 (8)	Cl1—Er1	2.603 (2)
N3—Er1	2.529 (7)	Cl2—Er1	2.594 (2)
N4—Er1	2.477 (7)		
O1—C1—O2A	110.9 (9)	Cl2—Er1—Cl1	96.60 (8)
O1—C1—C7	104.2 (8)		

Table 4-7-4. Selected geometric parameters (Å, º) for complex of **XVIII**

C1—O1	1.46 (2)	O1—Yb1	2.380 (10)
N1—Yb1	2.537 (14)	O3—Yb1	2.400 (12)
N2—Yb1	2.474 (13)	Cl1—Yb1	2.575 (4)
N3—Yb1	2.526 (15)	Cl2—Yb1	2.570 (4)
N4—Yb1	2.441 (13)		
O2A—C1—O1	112.6 (18)	Cl2—Yb1—Cl1	96.36 (15)
O1—C1—C7	105.2 (14)		

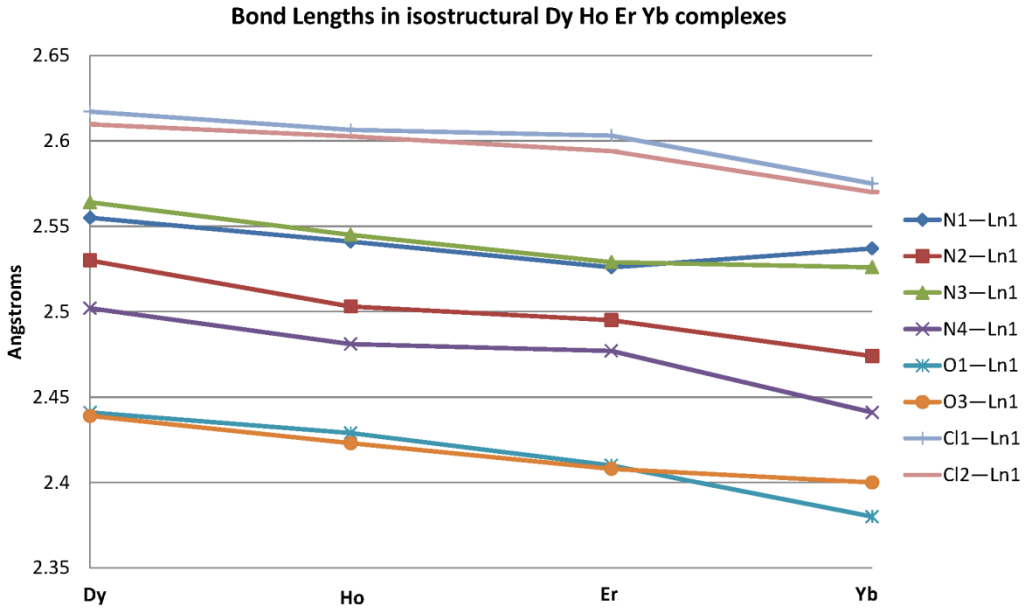

Figure 4-7-2. Illustration of the bond length distances of complexes of **XV**, **XVI**, **XVII** and **XVIII** to the ligandes.

The methoxy group was disordered in all four structures and was refined over two partially occupied sites in each case. *(Figure 4-7-3)*

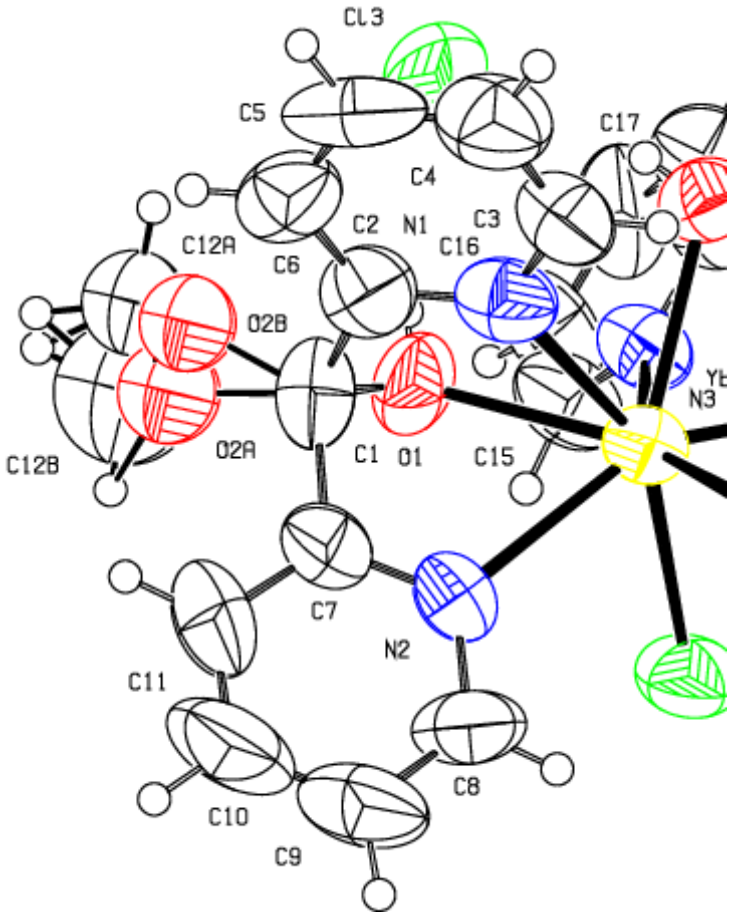

Figure 4-7-3. The methanol's carbon and oxygen are disordered across two sites in all the structure complexes of **XV**, **XVI**, **XVII** and **XVIII.** (the complex **XVIII** used as an example)

In all the complexes Cl3 receives two hydrogen bonds from H1B and H3B, *Figure 4-7-4*.

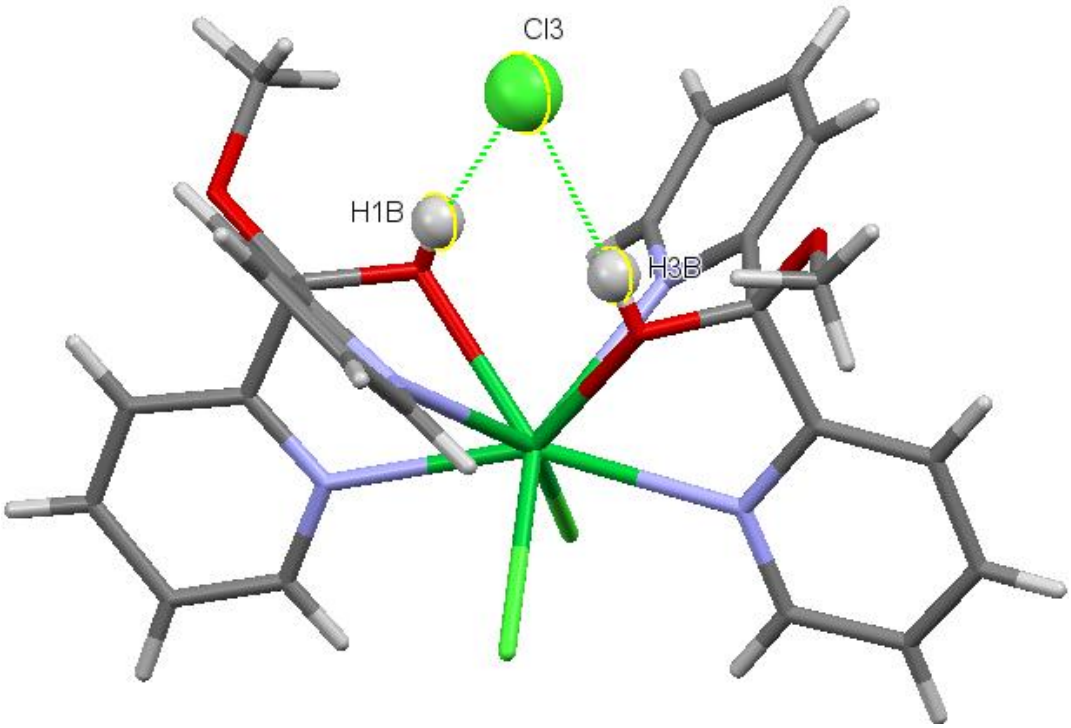

Figure 4-7-4. Hydrogen bonding of H1B and H3B to Cl3 in **XV**, **XVI**, **XVII** and **XVIII**.

Table 4-7-5. Some of crystallography data are collected for complexes of **XV**, **XVI**, **XVII** and **XVIII**

	XV	**XVI**	**XVII**	**XVIII**
Formula	$[C_{24}H_{24}N_4O_4Cl_3Dy]$	$[C_{24}H_{24}N_4O_4Cl_3Ho]$	$[C_{24}H_{24}N_4O_4Cl_3Er]$	$[C_{24}H_{24}N_4O_4Cl_3Yb]$
M_w	703.34	705.77	708.10	713.88
Crystal syst	Monoclinic	Monoclinic	Monoclinic	Monoclinic
Space group	P $2_1/n$	P $2_1/n$	P $2_1/n$	P $2_1/n$
a/Å	11.0378(3)	10.9875(2)	10.9809(3)	10.9341(18)
b/Å	13.7509(4)	13.7355(3)	13.7851(4)	13.946(3)
c/Å	17.3583(5)	17.2960(4)	17.2842(4)	17.334(4)
α/deg	90	90	90	90
β/deg	98.975(3)	99.2460(10)	99.186(2)	99.318(7)
γ/deg	90	90	90	90
V/Å^3	2602.38(13)	2576.38(9)	2582.80(12)	2608.4(9)
Z	4	4	4	4
R	2.45	3.88	5.62	6.79

4-7-1. Synthesis

36.8mg of 2,2′-dipyridyl ketone, 1.24mg of pyrazole, 376mg of $DyCl_3.6H_2O$, 379mg of $HoCl_3.6H_2O$, 381mg of $ErCl_3.6H_2O$ and 387 mg of $YbCl_3.6H_2O$ were each dissolved in 1ml of methanol to produce 0.1M solutions.

Two drops of 2,2′-dipyridyl ketone, two drops of pyrazole and one drop of the $DyCl_3$ solution were placed in a small vial, which was then sealed in a larger vial containing 1ml of diethyl ether anti-solvent.The same procedure was repeated for the other lanthanides solution.

After 48 hours crystals suitable for X-ray measurements had formed and were subjected to single crystal analysis.

As pyrazole did not react with 2,2′-dipyridyl ketone using the above method it was decided to omit it from subsequent reactions. However this changed the product as described in the next section.

4-8. $[(C_{11}H_8N_2O)\ OCH_3]_3\ LnCl_3$ Ln = Pr and Nd

When 2,2′-dipyridyl ketone and lanthanide chlorides were reacted following the scheme outlined in the previous section but with pyrazole omitted, neutral, nine coordinate $[(C_{11}H_8N_2O)\ OCH_3]_3\ LnCl_3$ (Ln= Pr, Nd) complexes were produced, which were analysed using X-ray single crystal methods, (*Figure 4-8-1)*. Crystallographic details are presented in *(Table 4-8-3)* and selected bond lengths and angles in *(Table 4-8-1 and Table 4-8-2).*

A crystallographic C_3 axis passes though the lanthanides atom to generate a three-face centred trigonal prism *(Figure4-8-1).*

In contrast to the previous structures, intermolecular hydrogen bonding links the methanolic OH to a pyridyl nitrogen *(Figure 4-8-3).*

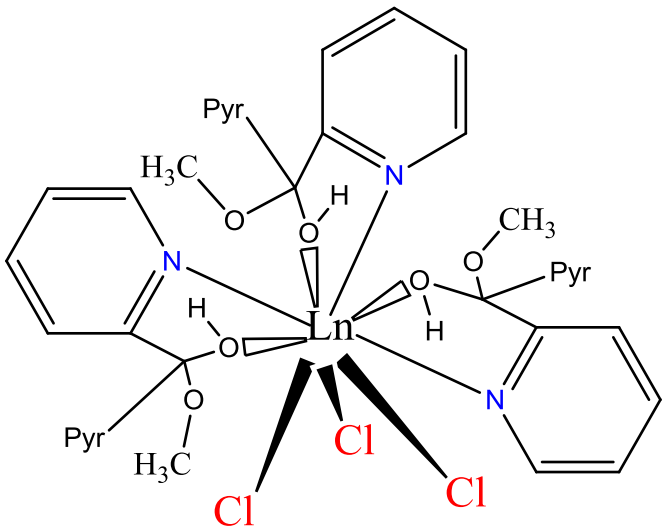

Pyridine = Pyr Ln = Pr, Nd

(XIX, XX)

Scheme 4-8-1. Ln, Pr = **XIX** and Nd = **XX**

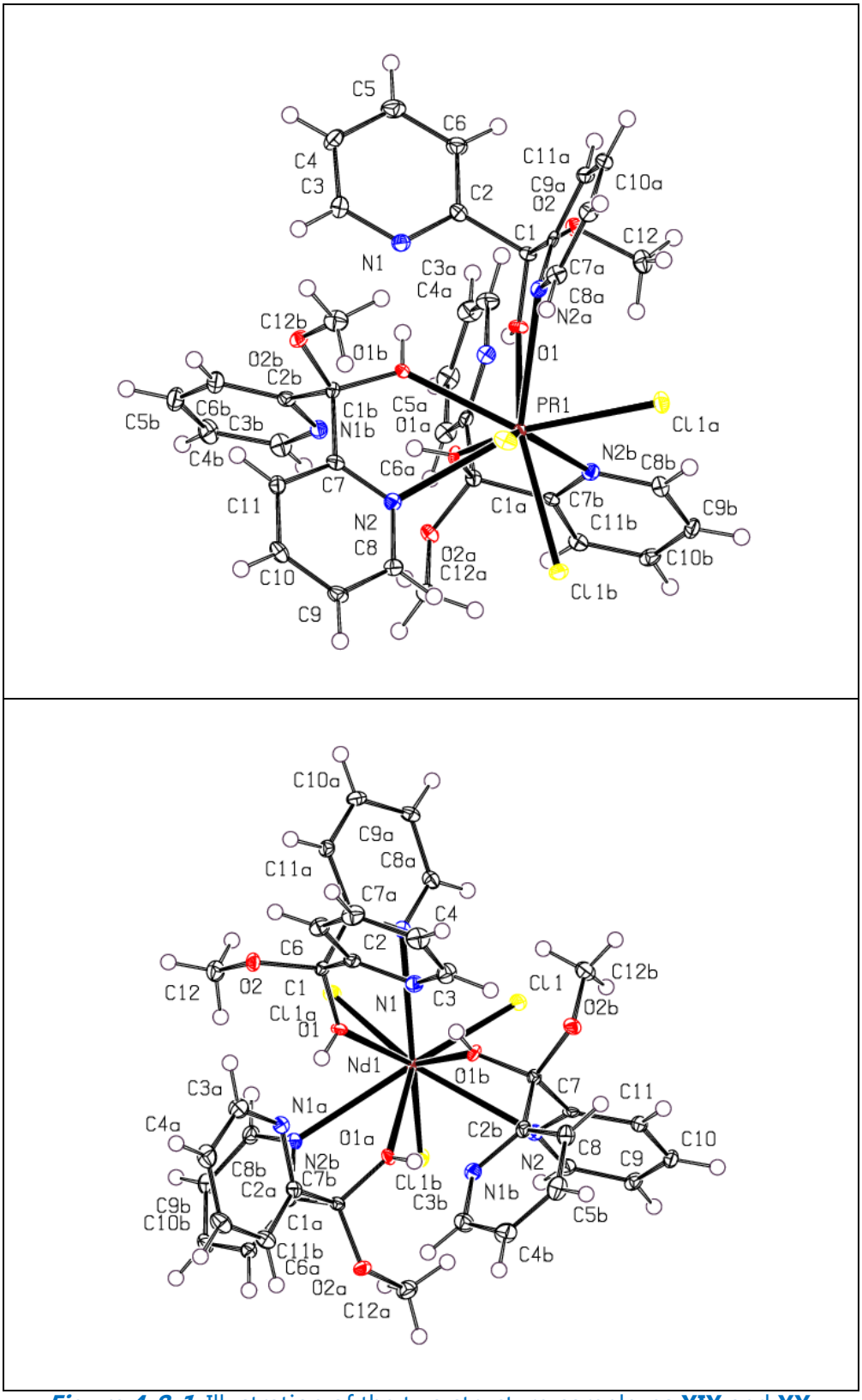

Figure 4-8-1. Illustration of the two structure complexes **XIX** and **XX**.

Table 4-8-1. Selected geometric parameters (Å, º) for complex of **XIX**

C1—O1	1.396 (3)	N2—Pr1	2.851 (2)
C1—O2	1.401 (3)	O1—Pr1	2.5148 (17)
Cl1—Pr1	2.7870 (7)		
O1—C1—O2	112.0 (2)	$O1^{ii}$—Pr1—Cl1	88.77 (4)
$O1^{i}$—Pr1—$O1^{ii}$	67.05 (6)	O1—Pr1—Cl1	131.77 (4)
$O1^{i}$—Pr1—Cl1	141.47 (4)		
O1—C1—C2—N1	38.9 (3)		

Symmetry codes: (i) *z, x, y,* (ii) *y, z, x.*

Table 4-8-2. Selected geometric parameters (Å, º) for complex of **XX**

C1—O1	1.400 (3)	N2—Nd1	2.846 (2)
C1—O2	1.403 (3)	O1—Nd1	2.4931 (17)
Cl1—Nd1	2.7724 (6)		
O1—C1—O2	111.86 (19)	$O1^{i}$—Nd1—$Cl1^{i}$	132.04 (4)
O1—Nd1—$O1^{i}$	67.34 (6)	$O1^{ii}$—Nd1—$Cl1^{i}$	141.35 (4)
O1—Nd1—$Cl1^{i}$	88.74 (4)		
O1—C1—C2—N1	39.3 (3)		

Symmetry cod: (i) *z, x, y;* (ii) *y, z, x.*

A search of the CCD was carried out using the following fragments. The Ln-Cl bond length were harvested using 3d function and are displayed as histograms in *Figure 4-8-2.*

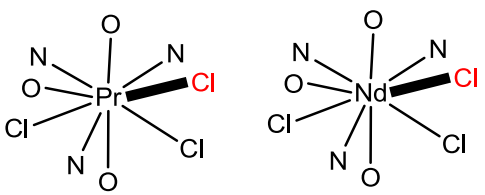

Referring to *Figure 4-8-2* for the Pr-Cl the range of bond distances are 1.925-3.115 Å with a mean of 2.828 Å, and for Nd-Cl are 1.928-3.152 Å and a mean of 2.804 Å. These show the Ln-Cl bond distances in complexes **XIX** and **XX** are shorter than the average bond distances from the CCD.

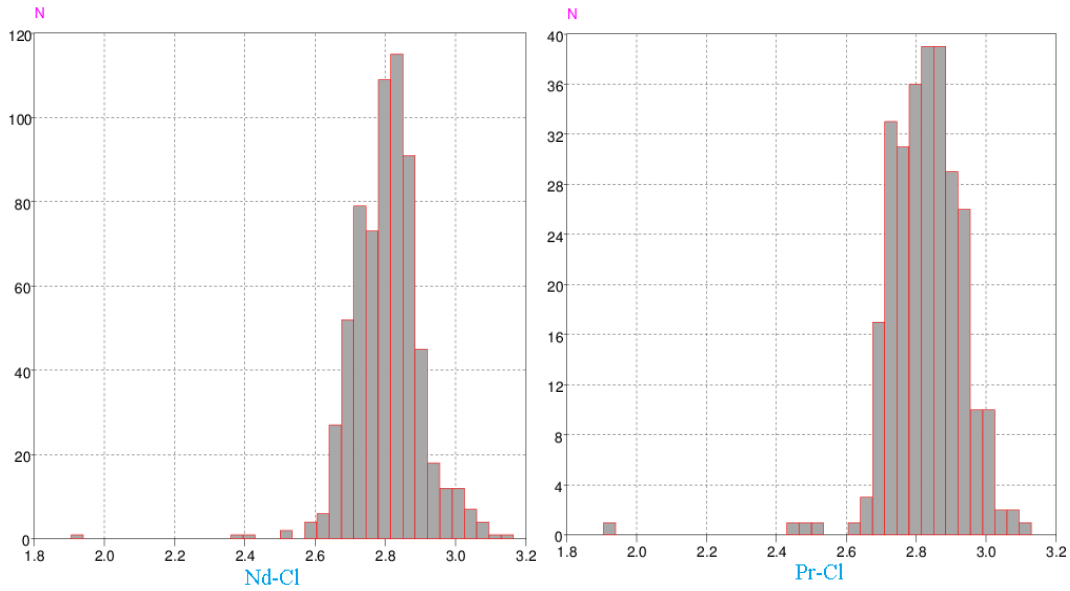

Figure 4-8-2. Few numbers of compounds from Cambridge Crystallographic Data base are hit, for measuring the bond distances of Pr-Cl and Nd-Cl. The fragment have been used were the same of configuration as complexes of **XIX** and **XX**

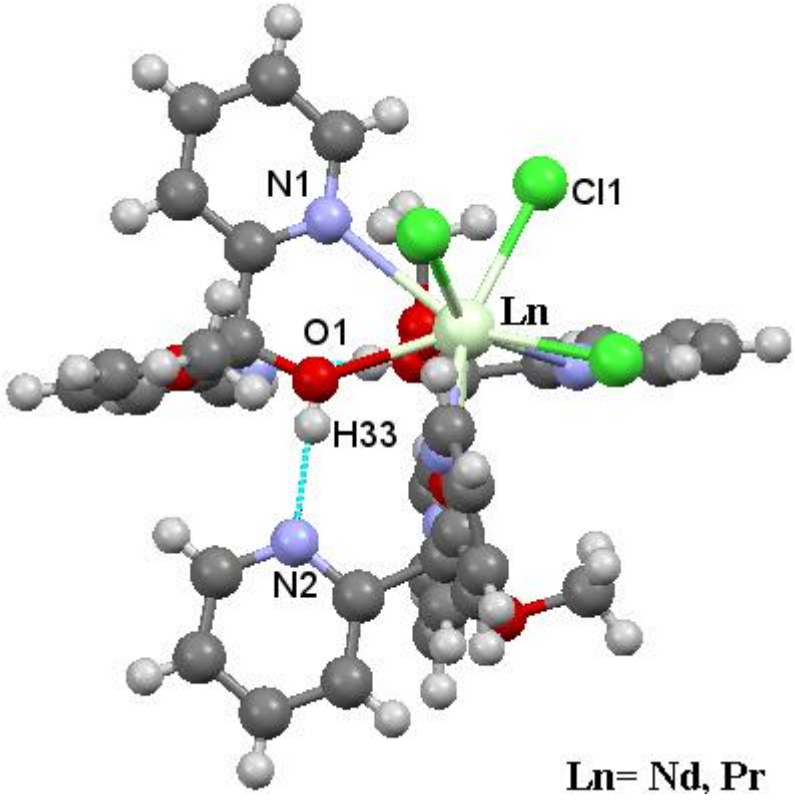

Figure 4-8-3. In complexes of **XIX** and **XX** the intermolecular hydrogen bonds between the H33 and N2

4-8-1. Synthesis

Complexes **XIX** and **XX** were obtained by the vapour diffusion method. In separate vials, 36.8mg of 2,2′-dipyridyl ketone in 1ml methanol (0.1M), and $PrCl_3.6H_2O$ (357mg, 0.1M in 1ml methanol) were mixed. Diethyl ether anti-solvent was used in the outer vial.

The procedure was repeated for Nd, using 360mg of $NdCl_3.6H_2O$ in 1ml of methanol (0.1M)

Table 4-8-2. Some crystallographic data for complexes **XIX** and **XX**.

	XIX	**XX**
Formula	$[C_{36}H_{36}N_6O_6Cl_3Pr]$	$[C_{36}H_{36}N_6O_6Cl_3Nd]$
M_w	923.91	917.31
Crystal syst	Cubic	Cubic
Space group	P a 3	P a -3
a/Å	19.4504 (2)	19.3550 (5)
b/Å	=	=
c/Å	=	=
α/deg	90	90
β/deg	=	=
γ/deg	=	=
V/Å^3	7358.44 (13)	7244.74 (19)
Z	8	8
R	3.10	2.5

4-9. *$[(C_{11}H_8N_2)\,OH\,(C_3H_3N_2)]_2\,Cl_2\,Fe\,(H_2O)_n$ (XXI)*

Attempts at synthesising **XXI** following the procedures used by Abrahams et al (2006) for the Ni analogue failed in this case and, indeed, in the cases of all the 3d transition metals. A different approach was therefore used based on our success at synthesising triangular lanthanide complexes containing the required ligand. As 3d metals have a stronger affinity for 2,2′-dipyridyl based ligands, iron chloride was therefore added to an aqueous solution containing Gd_3 triangles. On standing red square shaped crystals formed and were subjected X-ray analysis to reveal the structure shown in *Figure 4-9-1* and *Scheme 4-9-1.*

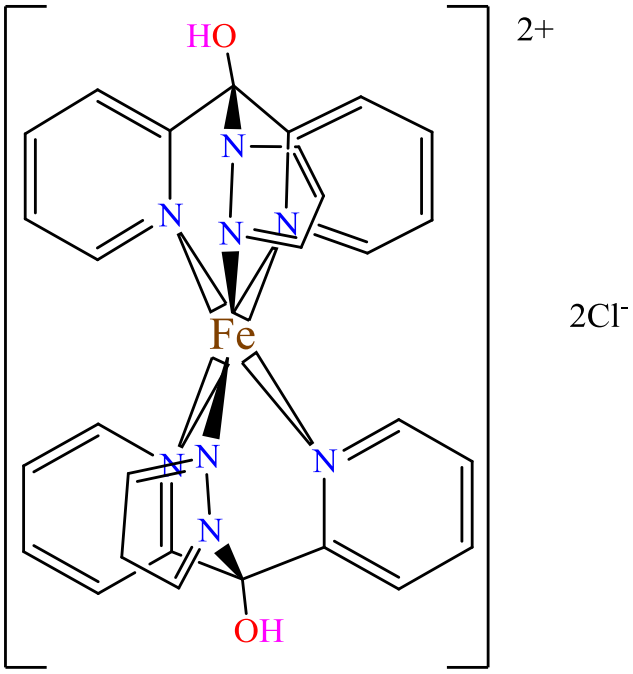

(XXI)

Scheme 4-9-1. Complex **XXI**

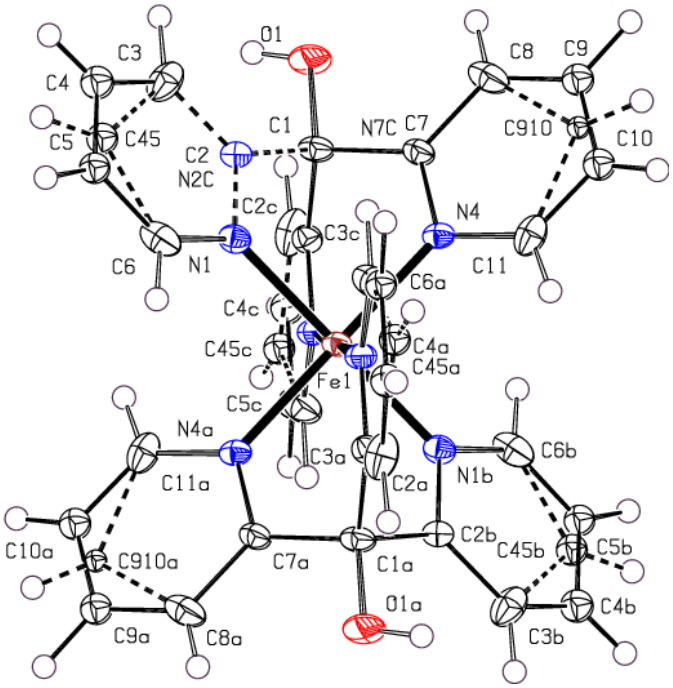

Figure 4-9-1. Illustration of the structure complex of **XXI**.

Crystallographic details are presented in *Table 4-9-2* and selected bond lengths and angles in *Table 4-9-1.*

Table 4-9-1. Selected geometric parameters (Å, º) for complex of **XXI**

Fe1—N1^{i}	1.967 (2)	Fe1—N4	1.979 (3)
N1^{i}—Fe1—N1	88.32 (13)	N1^{iii}—Fe1—N4	91.94 (9)
N1^{ii}—Fe1—N1	91.68 (13)	N1^{i}—Fe1—N4	88.06 (9)

Symmetry codes: (i) *x, -y, z,* (ii) *-x, y, -z*+1; (iii) *-x, -y, -z*+1.

As can be seen from *Table 4-9-1* and *Figure 4-9-1* the geometry around Fe is octahedral with crystallographic C_{2h} symmetry so that there are only at two unique Fe-N bonds of 1.967 (2) and 1.979 (2) Å. The N-Fe-N angles are all close 90º, ranging from 88.06 (9) to 91.94 (9)º.

The pyrazole shares disordered sites with the pyridine rings so that the overall molecular geometry is approximetly D_{3d}.

Adjacent molecules associate via hydrogen bonds, with involve the methanolic OH, water molecules and chloride conterions *(Figure 4-9-2).*

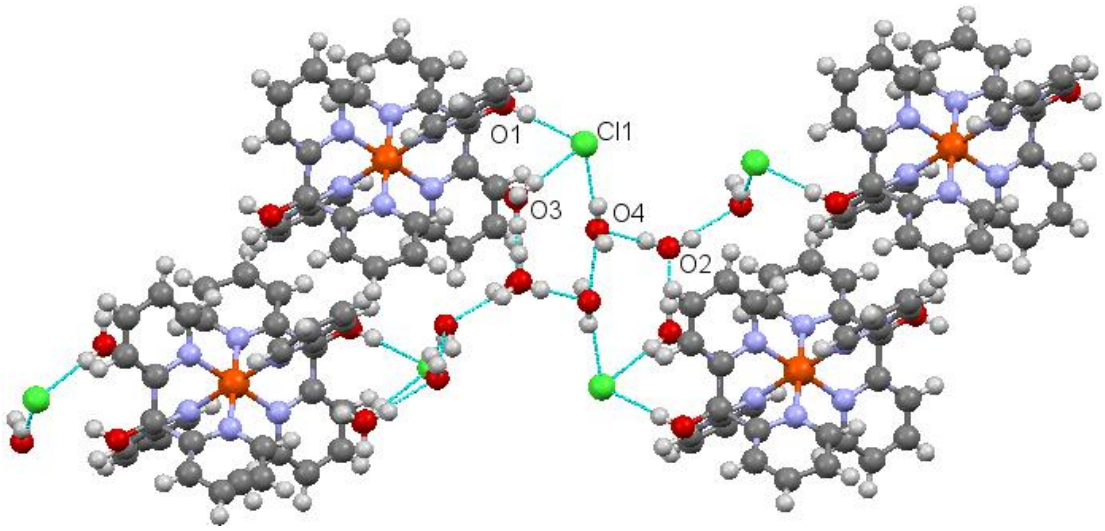

Figure 4-9-2. The chloride is surrounded by hydrogen bonds in complex **XXI**.

A search of the Cambridge Crystallographic Data base using Conquest and the illustrated fragment yielded more than 1000 hits *Figure 4-9-4*. A histogram of the distribution of Fe-N bond length in those fragments is illustrated in *Figure 4-9-3.*

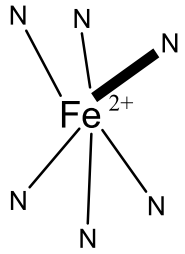

The range of Fe-N bond distances are 1.881-2.522 Å with a mean of 2.073 Å.

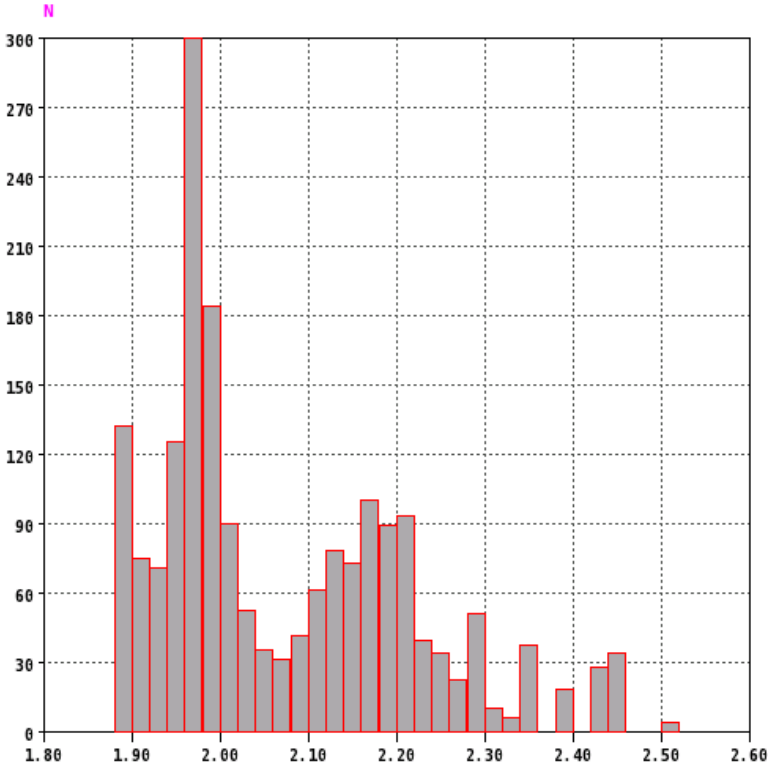

Figure 4-9-3. Distribution of Fe-N bond length in FeN_6 fragment

4-9-1. Synthesis

Stock solutions were prepared as follows, 0.528g of 2,2′-dipyridyl ketone in 10ml of water (0.3M), 0.128g of pyrazole in 10ml water (0.2M), 0.537g of $GdCl_3$ in 10ml water (0.2M) and 0.1625g of $FeCl_3$ in 10ml of water (0.1M).

One ml of each of the above solutions were mixed in Petri dishes to produce 3/2/2/1 molar ratios of the starting materials and left to stand at room temperature with a lid on. After a day reddish crystals of **XXI** started to form and were collected after a further two weeks.

Table 4-9-2. Some of the crystallography details are collected for complex **XIV**

Chemical formula	$C_{28}H_{40}Cl_2FeN_8O_{10}$
M_r	775.11
Crystal system, space group	Monoclinic, *C*2/*m*
Temperature (K)	100
a, *b*, *c* (Å)	12.2269 (7), 13.3360 (9), 10.7899 (7)
α (°)	101.431 (7)
V (Å^3)	1724.48 (19)
Z	2
Radiation type	Mo *K*α
μ (mm^{-1})	0.66
Crystal size (mm)	0.15 × 0.12 × 0.05
Diffractometer	Xcalibur, Sapphire2, large Be window diffractometer
Absorption correction	Multi-scan *CrysAlis PRO*, Agilent Technologies, Version 1.171.36.28a (release 18-03-2013 CrysAlis171 .NET) (compiled Mar 18 2013,11:47:30) Empirical absorption correction using spherical harmonics, implemented in SCALE3 ABSPACK scaling algorithm.
T_{min}, T_{max}	0.894, 1
No. of measured, independent and observed [$I > 2s(I)$] reflections	3192, 1805, 1411
R_{int}	0.041
$(\sin \Theta/\lambda)_{max}$ (Å^{-1})	0.628
$R[F^2 > 2\sigma(F^2)]$, $wR(F^2)$, S	0.047, 0.104, 1.04
No. of reflections	1805
No. of parameters	171
No. of restraints	5
H-atom treatment	H atoms treated by a mixture of independent and constrained refinement
$\Delta\rho_{max}$, $\Delta\rho_{min}$ (e Å^{-3})	0.47, -0.57

4-10. Conclusion

2,2′-dipyridyl ketone was chosen as a ligand because of its potential to act as a light antenna and an electron sink for photo-excited metal centres. Also the synthetic methods describe by Abrahams (2006) are ideal for a crystallographer with limited synthetic skills.

Abraham's original $M(py_2C(OH)SO_3)_2$ series, spanning the latter part of the first row divalent transition metals, has been completed and an Fe analogue of his $[Ni(py_2(C_3H_3N_2)C(OH))]Cl_2$ structure has been synthesised, albeit by devising a novel synthetic route involving $CeCl_3$.

Attempts at reacting 2,2′-dipyridyl ketone directly with $CuCl_2$ in the same manner that was used for $NiCl_2$ failed but some novel pyrazolate bridged Cu dimers were produced.

Attempting similar reactions with $LnCl_3$ proved to be much more successful and led to the novel series of Ln_3 triangular clusters described in Chapter 5. It also clearly established the lanthanides' ability to act as a template for the nucleophilic addition of pyrazole to 2,2′-dipyridyl ketone.

Some interesting lanthanide monomers were also produced, $[LnCl_2L_2]Cl$ and $[LnClL_3]Cl_2$, in which the ligand is $py_2C(OH)OMe$. In these cases the reaction medium was methanol and, despite

being present, pyrazole did not react, suggesting that water has an important role to play in the pyrazole reaction.

Two novel Pr coordination polymers were produced by reacting $Pr(NO_3)_3$ with 2,2′-dipyridyl ketone and sodium sulfite. Two type of crystals were generated, both contained $py_2C(OH)SO_3$ bridged dimers but linking the dimers into coordination polymers was achived via NO_3^- bridges in the case of one structure and SO_4^{2-} in the other.

Despite setting off on this project with the intention of limiting the synthetic requirements it is felt that a good understanding of the reactivity of 2,2′-dipyridyl ketone has been achieved and that a good base has been laid to develop the range and type of crystalline products even further.

4-11. References

Abrahams , B. F., Hudson, T. A., Robson, R., 2006, *Chem.-Eur. J.,* **12**, 7095.

Allen, F. H. (2002). *Acta Cryst*. **B58**, 380–388.

Altomare, A., Cascarano, G., Giacovazzo, C., Guagliardi, A., Burla, M. C.,Polidori, G. & Camalli, M. (1994). J. *Appl*. *Cryst*. **27**, 435.

Basu. A., Kasar. T. G., and Sapre. N. Y., (1988), *Inorg. Chem.*, **27**, 4539-4542

Beagley, B., Eriksson, A., Lindgren, J., Persson, I., Pettersson, L. G. M.,Sandstromr, M., Wahlgrenll, U. & White, E. W. (1989). J. *Phys*. *Condens.Mat*. 2395–2408.

Blessing, R. H. (1995). *Acta Cryst*. **A51**, 33–38.

Bock. H., Dienelt. R., Schödel. H., Van. T. H., *structural chemistry*, (1998), 9, No. **4**, 279-288.

Efthymiou. C. G., Papatriantafyllopoulou. C., Aromi. G., Teat. S. J., Christou. G, Perlepes. S. P., (2011), *Polyhedron,* **30**, 3022–3025

Falvello, L. R. (1997). *J. Chem. Soc. Dalton Trans*. 4463–4475.

Farrugia, L. J. (1997). J. *Appl*. *Cryst*. **30**, 565-568.

Farrugia, L. J. (1999). J. *Appl*. *Cryst*. **32**, 837–838.

Fletcher, D. A., McMeeking, R. F. & Parkin, D. (1996). J. *Chem*. *Inf*. *Comput.Sci*. **36**, 746–749.

Klinman, J. P., Li. R., Mathews, F. S., (1998). *Structure*, **6**, 294–307.

Kozlevca r, B., Gamez, P., de Gelder, R., Driessen, W. L. & Reedijk, J. (2003). *Eur. J. Inorg. Chem*. 47–50.

.Li, R., Klinman, J. P. & Mathews, F. S. (1998). *Structure*, **6**, 294–307.

Nonius (1998),. Nonius BV, Delft, The Netherlands.
Otwinowski, Z. & Minor, W. (1997). *Methods in Enzymology*, Vol. 276, Macromolecular Crystallography, Part A, edited by C. W. Carter Jr & R. M. Sweet,. 307–326. New York: Academic Press.

Sarkar. S., Sarkar. B., Chanda. N., Kar. S., Mobin. S. M., Fiedler. J., Kaim. W., and Lahiri. G.K., (2005), *Inorg. Chem.*, **44**, 6092-6099

Sheldrick, G. M. (2008). *Acta Cryst*. **A64**, 112–122.

Steel. P., Sumby. C., (2003), *Dalton Trans*, 4505-4510

Westrip, S. P. (2010). *J. Appl. Cryst*. **43**, 920–925

Chapter 5: The synthesis and structural characterisation of an isostructural series of triangular lanthanide clusters, including the measurements and modelling of magnetic behaviour in selected members of the series

5-1. Introduction

The research presented in this chapter was triggered by the chance discovery of the triangular praseodymium cluster and potential single molecule magnet mentioned in Chapter 4. The triangular cluster formed spontaneously by reacting $PrCl_3$, 2,2′-dipyridyl ketone and pyrazole in aqueous solution, as outlined in the following scheme in *Figure 5-1-1*.

Magnetic measurement were carried out by Dr Floriana Tuna of the University of Manchester and computation of magnetic vectors were perform by Prof. L. F. Chibotaru from the University of Leuven, Belgium.

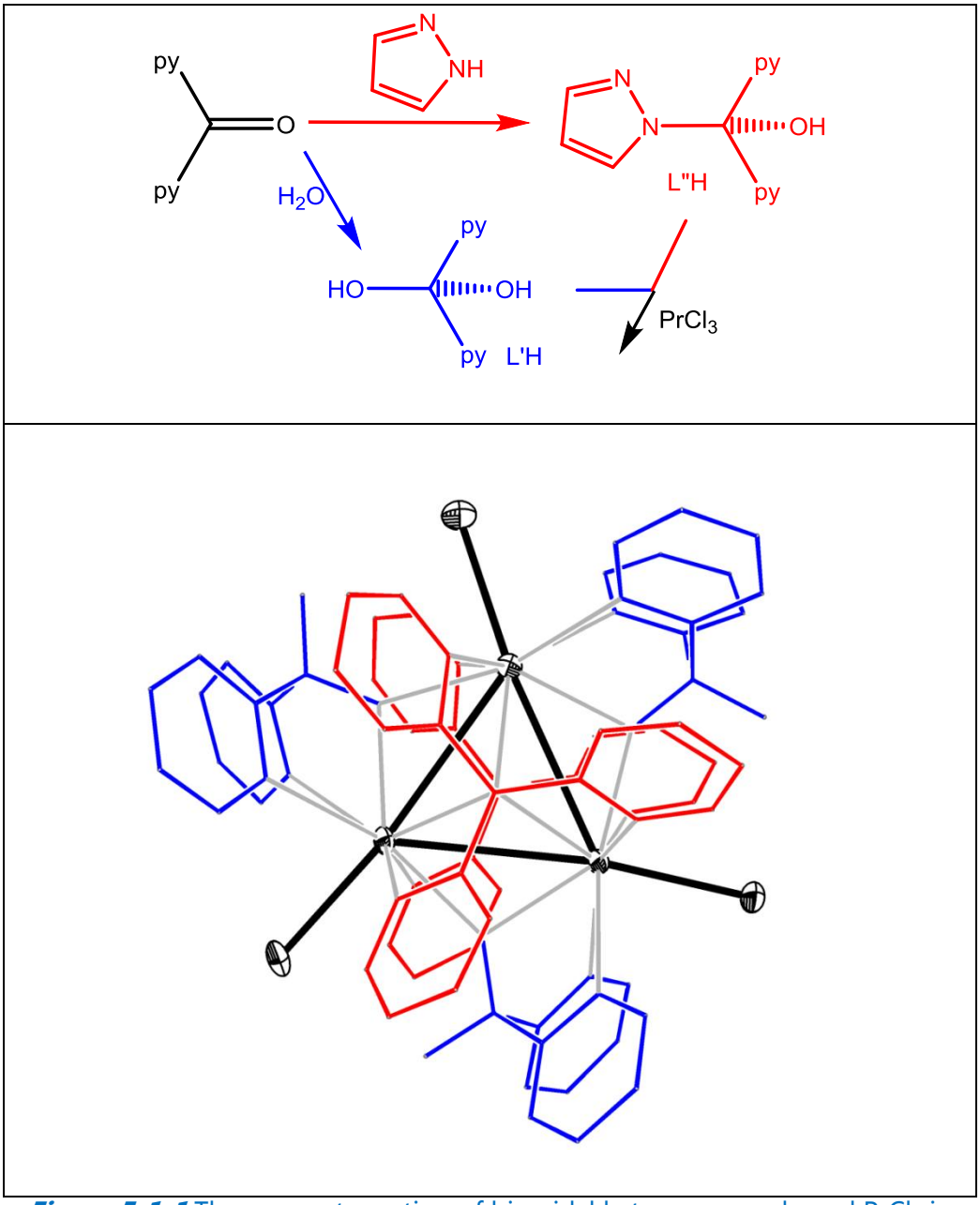

Figure 5-1-1 The one-pot reaction of bipyridyl ketone, pyrazole and $PrCl_3$ in aqueous solution to form the triangular cation, $[Pr_3Cl_3L'_3L''_2]^+$, L' = $Cpy_2(OH)O^-$ and L'' = $Cpy_2(C_3H_3N_2)O^-$. For the latter ligand the pyridine and pyrazole rings occupy mixed sites, which have not been portrayed in the figure for clarity.

Single Molecule Magnets (SMMs) usually consist of transition or lanthanide metal clusters and are of interest because of their large ground state spin and slow magnetic relaxation, making them ideal candidates for very high density data storage. Lanthanide

complexes are of particular interest because of their high potential number of unpaired f-electrons. Unlike the d-block metals, there is a significant orbital contribution in the f elements. Nevertheless, the ground state magnetic moment for the tri-positive lanthanum cations are still calculated using the Russell-Saunders scheme and are given in *Table 5-1* below (Orchard, 2003; Kaltsoyannis & Scott, 1999), showing good agreement between the theoretical and measured values. These are the values of $\boldsymbol{\mu}_{eff}$ that would be anticipated for the lanthanide clusters at room temperature.

						$\boldsymbol{\mu}_{eff}$ (Bohr Magnetons)		
Ln^{3+}	No. of 4***f*** electrons	ground state L	S	J	$\boldsymbol{g}_J$	Theoretical (A)	(B)	Observed
Ce	1	3	1/2	5/2	6/7	2.54	2.56	2.3-2.5
Pr	2	5	1	4	4/5	3.58	3.62	3.4-3.6
Nd	3	6	3/2	9/2	8/11	3.62	3.68	3.5-3.6
Pm	4	6	2	4	3/5	2.68	2.86	-
Sm	5	5	5/2	5/2	2/7	0.85	[~ 1.60]#	1.4-1.7
Eu	6	3	3	0	-	0	[~ 3.45]#	3.3-3.5
Gd	7	0	7/2	7/2	2	7.94	7.94	7.9-8.0
Tb	8	3	3	6	3/2	9.72	9.72	9.5-9.8
Dy	9	5	5/2	15/2	4/3	10.63	10.63	10.4-10.6
Ho	10	6	2	8	5/4	10.60	10.60	10.4-10.7
Er	11	6	3/2	15/2	6/5	9.57	9.57	9.4-9.6
Tm	12	5	1	6	7/6	7.63	7.63	7.1-7.5
Yb	13	3	1/2	7/2	8/7	4.50	4.50	4.3-4.9
Lu	14	0	0	0	-	0	0	0

Table 5-1-1 Ground states of the Ln^{+3} ions and their predicted and measured $\boldsymbol{\mu}_{eff}$ values at 300 K. For (A) $\boldsymbol{\mu}_{eff} = g_J [\boldsymbol{J}(\boldsymbol{J} + 1)]^{\boldsymbol{1/2}}$ and for (B) $\boldsymbol{\mu}_{eff}$ (J) $=[g_j^{\boldsymbol{2}}\boldsymbol{J}(\boldsymbol{J} + 1) + kT\alpha`_J]^{\boldsymbol{1/2}}$ $g_j$ is the Lande g-factor, given by $g_j = 1 + (g_e - 1)\,[J(J + 1) + S(S + 1) - L(L + 1)/\, 2J(J + 1)]$, where $g_e$ is a constant, 2.002319, known as the electron spin g-factor. $\alpha`_J = \alpha_J/\mu_B$ (for an isolated multiplet, the only one populated, $\alpha$is identifiable with the magnetizability).

Recent work by Tanget al (2006) and Lin et al (2012) revealed an

intriguing possibility when the lanthanides are in the form of a triangular cluster. As the temperature drops the spin vector on the three lanthanide exhibit cooperative behaviour, which becomes complete as the temperature approaches absolute zero. The resulting magnetic moment displayed by each triangle depends on whether their magnetic vectors are directed in the plane of the triangle or perpendicular to the plane. If the vectors are in the plane of the triangle they can completely cancel out and the material becomes diamagnetic. In contrast, three vectors that are directed perpendicular to the triangle's plane can never cancel each other out and remain paramagnetic as the three vectors experience spin-frustration.

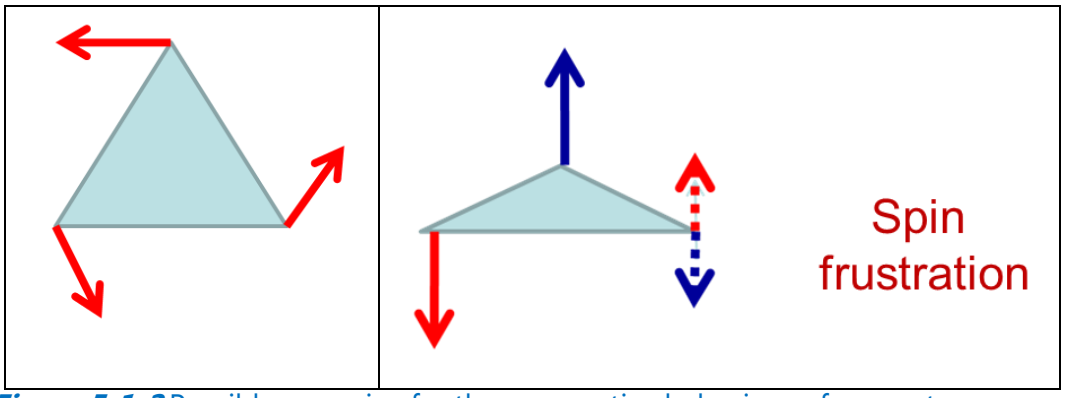

Figure 5-1-2 Possible scenarios for the cooperative behaviour of magnets arranged in a triangle.

This behaviour varies from lanthanide to lanthanide but can be modelled provided an accurate crystal structure is available. The resulting variation of magnetic moment with temperature can then be compared with experimental measurements to verify the accuracy of the model and fine-tune the computational

parameters.

Key to this process is the production of crystals that are of suitable quality for X-ray crystallography but in sufficient quantity and purity for magnetic measurements. The initial synthesis of Pr_3 triangle crystals, mentioned in the previous chapter, was not only of extremely low yield but also generated copious quantities of a viscous gel, which made it almost impossible to extract a crystal for X-ray measurements. The crystals were certainly not produced in sufficient quantity or purity for magnetic measurements. For this reason the focus of the initial part of this chapter will be to describe the development of a synthetic/crystallisation route. Once this has been done, detailed descriptions of the triangle X-ray crystal structures will be provided. Modelling the disordered chloride counterion and various guest molecules in the unit cell proved challenging. A general crystal structure modelling scheme was eventually developed and has already been applied to the structures required for magnetic measurements and modelling but the other structures, although they have been refined, await incorporation to the standardised model for completion. The main synthetic route adopted to make material for magnetic measurements consistently produced a rhombohedral structures, however it was possible to produce different polymorphs by changing the synthesis/crystallisation method and these will also be reported briefly.

5-2. Synthesis

Method 1

The initial method was based directly on Abraham's simple synthesis of $[Ni\{py_2(C_3H_3N_2)COH\}_2]^{2+}$ i.e. 0.1 M aqueous stock solutions of each reagent were prepared (2,2'-dipyridyl ketone, pyrazole and lanthanide trichloride). These were mixed together in volume, and hence molar ratios, of 2:2:1 and allowed to stand in a large capped sample vial. Unlike the 1st row transition metal reactions, crystals did not appear, even after weeks of standing, so the containers were opened and some of the water allowed to evaporate. The resulting gel contained a few, miniscule crystals, which were laboriously separated from the gel by manipulation under Fomblin fluorinated oil. The crystals were examined on the single crystal X–ray diffractometer, to reveal our first Pr_3 triangle. X–ray powder diffraction measurements made on the gel before and after it dried to a glassy solid failed to detect any diffraction pattern i.e. the gel is X–ray amorphous

Method 2

Once the molecular composition was known the ratios of solutions used in method 1 were modified to 5:2:3 (2,2'-dipyridyl ketone: pyrazole: lanthanide trichloride). This did not improve the

outcome so two further modifications were made.

(a) Lidded glass Petrie dishes were used instead of the large sample vials. This made it easier to view any crystals forming in the solution and to remove and replace the lid in order to control evaporation without disturbing the crystallising solution.

(b) The organic components, 2,2′-dipyridyl ketone and pyrazole, were dissolved in dichloromethane rather than water. These were mixed together in a ratio of 5:2. This dichloromethane solution was layered on the aqueous lanthanide trichloride already in the Petrie dish. Because of the small solution volumes involved, the Petrie dish was tilted slightly so that the two solutions made good contact. The Petrie dish was then covered and allowed to stand for a week. After approximately 24 hours the dichloromethane had evaporated to leave an aqueous solution of the reagents to react.

This method produced large (1 mm) rhombohedral crystals of Ce_3, Sm_3 Pr_3 and Nd_3 triangles but initial crystal formation of miniscule crystals in the Sm and Eu solutions was stifled by gel formation and only gel was observed in the solutions containing Gd, Tb, Dy, Ho, Er, Yb and Lu. The decline in crystal formation mirrors the fall in the rate of the dissociative reactions of hydrated Ln^{3+} cations e.g. the rate

constants for the formation of 1:1 Ln^{3+}/oxalate complexes presented in *Figure 2* (Kaltsoyannis & Scott, 1999)

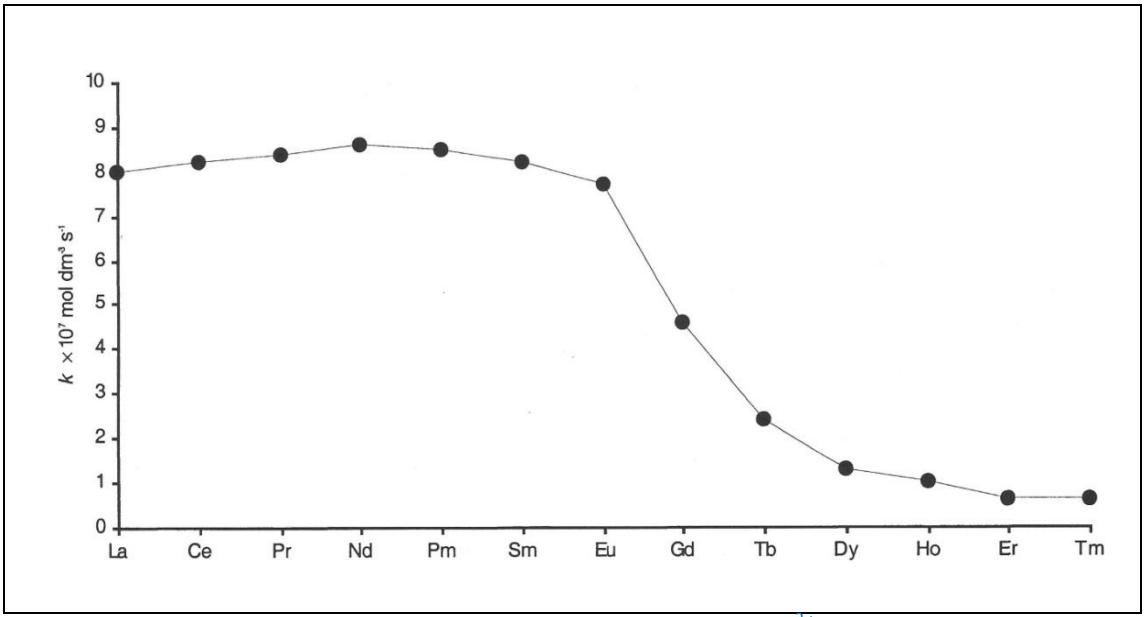

Figure 5-2-1 Rate constants for the formation of 1:1 Ln^{3+}/oxalate complexes at 25° C (Kaltsoyannis & Scott, 1999)

A series of experiments were therefore carried out in an attempt to identify conditions which would limit gel formation.

- The initial solution concentrations were adjusted but had no beneficial effect.
- Alternatives to dichloromethane were tested, including methanol, ethanol, acetone, toluene or diethylether but produced no reduction in gel formation.
- The crystallising solution's pH was adjusted by adding HCl or NH_4OH but had no effect.

As none of the above variations reduced gel formation it was decided to try and control the extent of water loss at the point of crystallisation/gel formation by adjusting the relative humidity above the solution.

Method 3

Initially the Petrie dishes were set up as for Method 2 but if gel formation was observed the Petrie dish with its lid in place was positioned over water in a desiccator (100% RH), which was then placed in a constant temperature chamber at 30° C. This caused the gel to re-dissolve in 24-48h. At this point the Petrie dish with its lid still in place was removed from the desiccator and allowed to stand in the constant temperature chamber. It was then checked daily for crystal formation and to ensure that the solution remained gel free. If gel formed the dish was returned to the 100% RH desiccator for a period. Once sufficient crystals had formed the solution was filtered and the crystals washed twice with a small amount of cold methanol before being placed in a sample container.

This method did not require the organic reagents to be dissolved in dichloromethane so aqueous solutions were used after the initial experiment.

Also it was found that limiting the RH to 75% by using saturated

NaCl solutions and removing the Petrie dish lid offered more control when re-dissolving the gel.

Using this method it proved possible to produce good crystals of the Gd, Tb, Dy, Ho and Er triangles.

5-3. Crystal structures

All the lanthanide triangle structures synthesised by method 3 are isomorphous. They all belong to rhombohedral space group R -3 and have similar cell dimensions, which are presented in *Table 5-3-1* along with other crystallographic details. An Ortep view of the dysprosium triangle is shown in *Figure 5-3-1*. It has an identical structure to the other lanthanide triangles and an identical labelling scheme to the six fully refined triangles in *Table 5-3-1A*. Selected bond lengths and angles for all nine lanthanide triangles are presented in *Table 5-3-2*.

Table 5-3-1A Crystal and refinement details for Ln triangles that have been refined with optimum constraints.

Lanthanide	Nd	Gd	Dy	Er	Pr	Eu
Asymmetric Unit	$C_{67.3}H_{64.1}Cl_4$ $N_{15.5}Nd_3O_{13.6}$	$C_{67.3}H_{61}Cl_4$ $Gd_3N_{15.5}O_{12}$	$C_{66.5}H_{59.5}Cl_4$ $Dy_3N_{15}O_{11.78}$	$C_{67}H_{62}Cl_4$ $Er_3N_{16}O_{12}$	$C_{60}H_{60}Cl_6$ $N_{12}O_{12}Pr_3$	$C_{60}H_{60}Cl_3$ $Eu_3N_{12}O_{12}$
M_r	1881.06	1892.2	1886.54	1927.35	1830.96	1864.11
Space group	$R\bar{3}$	$R\bar{3}$	$R\bar{3}$	$R\bar{3}$	$R\bar{3}$	$R\bar{3}$
a (Å)	38.0721 (19)	37.8220 (6)	38.0648 (15)	37.666 (2)	38.1424 (5)	37.5837 (9)
c (Å)	31.2010 (15)	30.7919 (5)	31.1975 (14)	30.8251 (12)	31.1267 (4)	30.8019 (8)
V (Å^3)	39166 (3)	38146.6 (11)	39147 (3)	37874 (3)	39217.5 (9)	37679.7 (16)
Z	*18*	*18*	*18*	18	18	18
T *(K)*	*150*	*100*	*150*	100	150	150
$F(000)$	*16788*	16725	16627	16993	16273	16489
ρ (Mg m^{-3})	1.436	1.483	1.440	1.521	1.395	1.479
μ (mm^{-1})	15.09	16.63	15.19	6.66	14.30	17.57
measured refs	55130	40966	39870	38758	81808	77083
Ind refs	16315	16278	14018	15099	17107	14239
R_{int}	0.042	0.088	0.166	0.170	0.078	0.114
Parameters	988	952	950	956	989	984
$wR(F^2)$	0.133	0.194	0.28	0.169	0.137	0.167
S	1.03	1.02	0.98	1.02	1.03	1.01
$R[F^2 > 2\sigma(F^2)]$	0.046	0.066	0.083	0.090	0.047	0.055
refs $I > 2\sigma(I)$	14367	10714	5827	6501	14060	10773

Table 5-3-1B Crystal and refinement details for lanthanide triangles that require further refinement

Lanthanide	Ce	Sm	Tb
Formula	$C_{60}H_{60}Ce_3Cl_3N_{12}O_{16}$	$C_{60}H_{60}Cl_4N_{12}O_{16}Sm_3$	$C_{60}H_{60}Cl_3N_{12}O_{16}Tb_3$
M_r	1731.91	1798.05	1788.31
Space group	$R\bar{3}$	$R\bar{3}$	$R\bar{3}$
a (Å)	38.0326 (3)	37.8863 (6)	37.7468 (5)
b (Å)	38.0327 (3)	37.8862 (6)	37.7468 (5)
c (Å)	31.1308 (3)	30.9946 (6)	30.8776 (5)
V (Å^3)	38997.2 (6)	38528.3 (11)	38100.8 (9)
T (K)	100	100	100
measured reflections	34077	35371	33362
independent reflections	18889	18589	17609
R_{int}	0.055	0.175	0.123
Parameters	949	503	552
$wR(F^2)$	0.197	0.273	0.287
S	1.06	1.06	1.01
$R[F^2 > 2\sigma(F^2)]$	0.063	0.099	0.082
reflections with $I > 2\sigma(I)$	11966	9217	8841

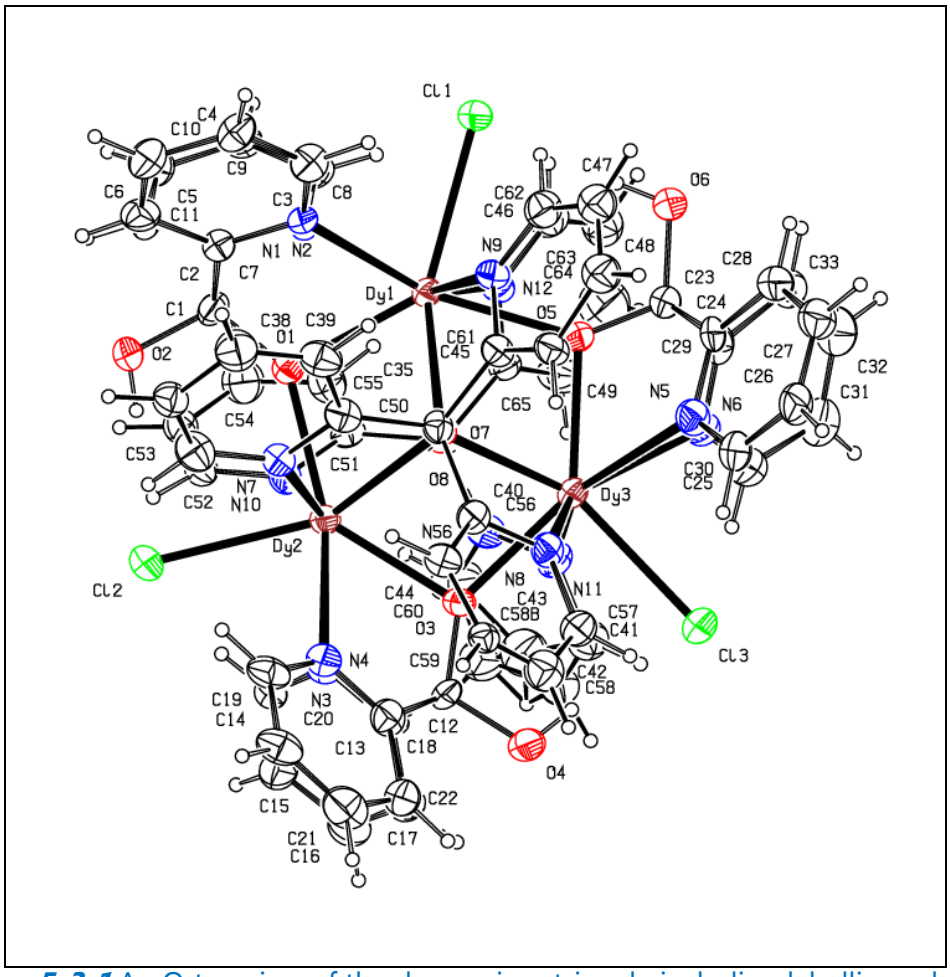

Figure 5-3-1 An Ortep view of the dysprosium triangle including labelling scheme. The chloride counterion and various solvate molecules have been omitted for clarity.

All nine lanthanide triangle cations studied in the current work display C_{3h} symmetry, as illustrated in *Figure 5-3-1*. This is because the pyrazole and pyridine rings of the tetrapodal capping ligand are disordered, with each site containing a superposition of pyrazole and pyridine rings. Refinement of the three pyrazole occupancies on each ligand was subject to the constraint that disordered fragments sum up to a pyrazole and two pyridine groups per ligand. Pyrazole site occupancy shows considerable variation e.g. Nd 0.29(2)-0.39(2), Gd 0.01(2)-0.70(2), Dy 0.17(4)-

0.50(4)) with no site containing 100% pyrazole and 2/3 of the occupancies falling in the range 0.33+- 0.07. No clear picture has emerged as to whether or not the pyrazole substituents prefer an eclipsed conformation or otherwise. With a proviso for the above disorder, each lanthanide sits in the centre of identical 9-coordinate tri-capped trigonal prisms *(Figure. 5-3-2)*.

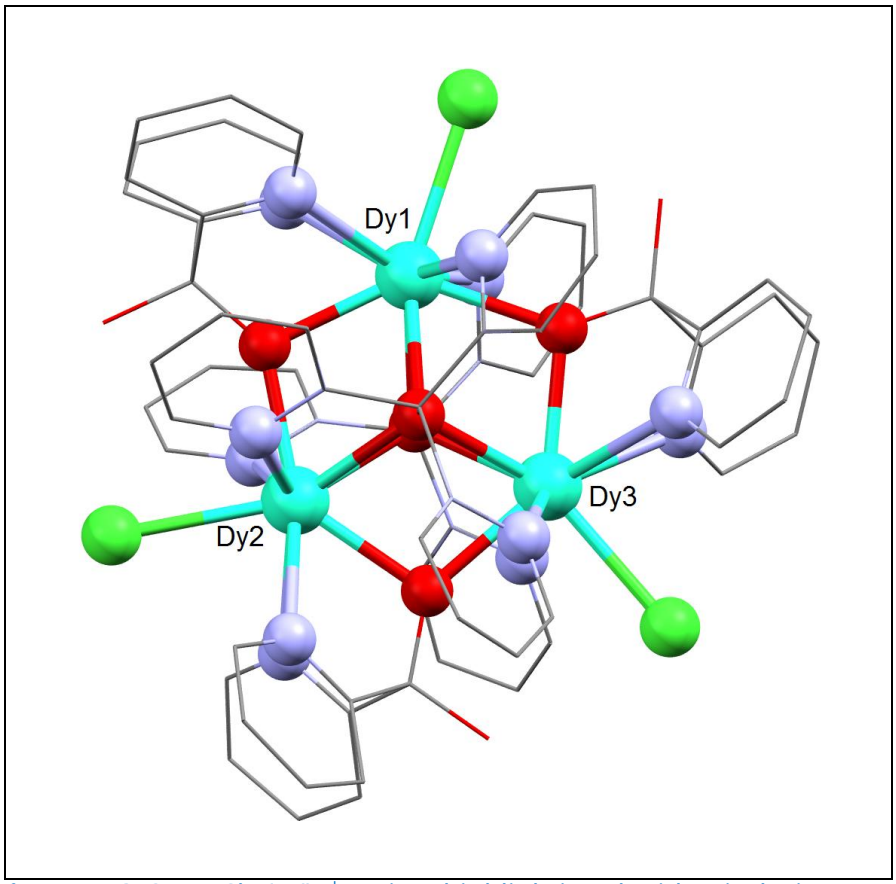

Figure 5-3-2 $[Dy_3Cl_3L'_3L''_2]^+$ cation, highlighting the identical tri-capped trigonaprism coordination around each Dy atom. All nine structures are identical.

Three oxygen bridges between each Ln maintain them as a regular equilateral triangle with all Ln..Ln..Ln angles falling in the range 59.755 (14) to 60.237 (2) ° (Table 5-3-2). Also the Ln….Ln

distances vary linearly with published Ln^{3+} ionic radii *(Figure 5-3-3)*, supporting the picture of a rigid structure, which is not unexpected, given the number of pyridine struts that support the oxygen bridges.

	Ce	Pr	Nd	Sm	Eu	Gd	Tb	Dy	Er
Ln1—Ln3	3.8137 (6)	3.7815 (1)	3.7826 (4)	3.7259 (9)	3.7061 (2)	3.6811 (7)	3.6729 (10)	3.6586 (14)	3.6326 (10)
Ln1—Ln2	3.8171 (6)	3.7982 (1)	3.7952 (4)	3.7290 (8)	3.7160 (2)	3.6937 (7)	3.6818 (10)	3.6687 (14)	3.6402 (12)
Ln2—Ln3	3.8255 (6)	3.7878 (1)	3.7844 (4)	3.7204 (8)	3.7127 (2)	3.6959 (7)	3.6825 (9)	3.6687 (14)	3.6395 (12)
Ln1—Cl1	2.823 (2)	2.7964 (4)	2.7942 (12)	2.755 (3)	2.7363 (5)	2.723 (2)	2.724 (4)	2.702 (4)	2.687 (4)
Ln2—Cl2	2.824 (2)	2.8079 (4)	2.8053 (12)	2.756 (3)	2.7544 (5)	2.732 (2)	2.713 (4)	2.712 (5)	2.691 (4)
Ln3—Cl3	2.809 (2)	2.8047 (5)	2.8020 (14)	2.745 (3)	2.7529 (6)	2.728 (3)	2.738 (4)	2.707 (5)	2.681 (4)
Ln3-Ln1-Ln2	60.176 (11)	59.964 (2)	59.920 (7)	59.875 (16)	60.030 (3)	60.152 (14)	60.092 (19)	60.09 (3)	60.06 (2)
Ln1-Ln2-Ln3	59.867 (11)	59.799 (2)	59.875 (7)	60.104 (16)	59.853 (3)	59.755 (14)	60.073 (19)	59.82 (3)	59.87 (2)
Ln1-Ln3-Ln2	59.957 (11)	60.237 (2)	60.205 (7)	60.021 (16)	60.118 (3)	60.093 (14)	59.835 (19)	60.09 (3)	60.07 (2)

Table 5-3-2 Selected geometric parameters (°, Å) for the lanthanide triangle cations, $[Ln_3Cl_3L'_3L''_2]^+$, where L′ = $py_2C(OH)O^-$ and L″ = $py_2(C_3H_3N_2)CO^-$

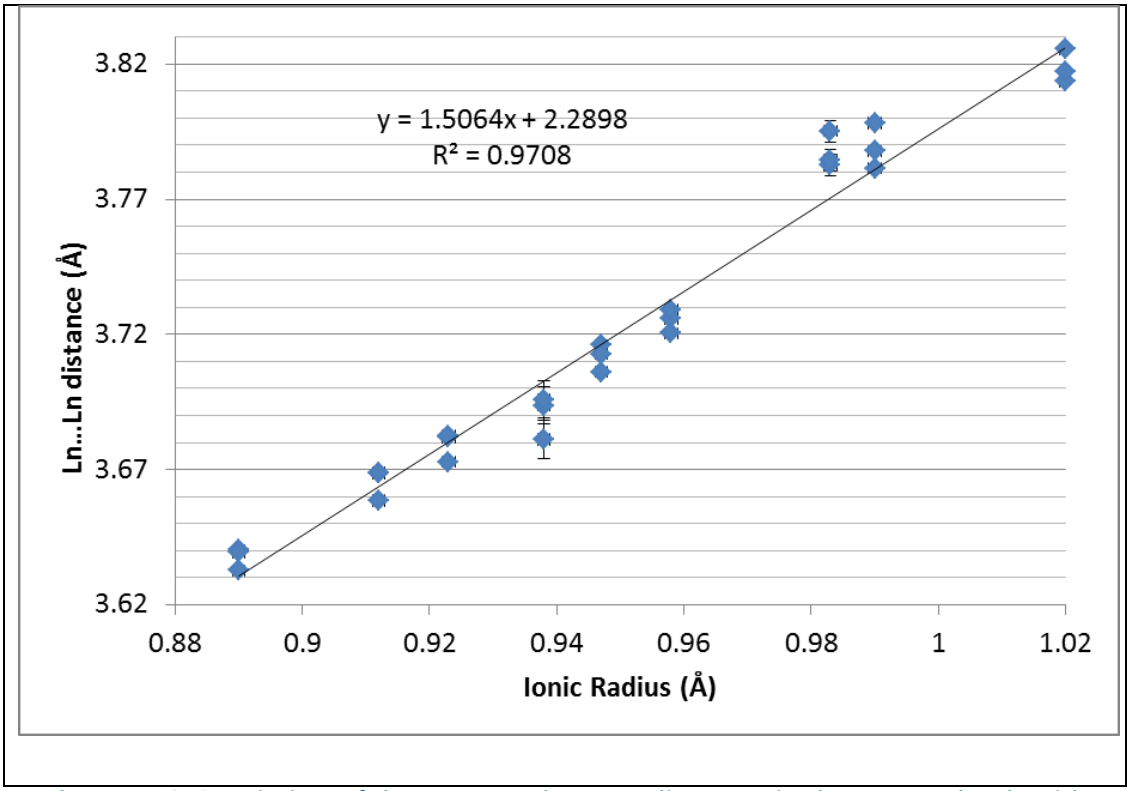

Figure 5-3-3 Variation of the measured Ln...Ln distances in the current lanthanide

triangles with published Ln^{3+} ionic radii (Å) (Greenwood &Earnshaw; 1997).

Crystal packing in the current structures is dominated by large channels extending along the 0 0 1 direction *(Figure 5-3-4).* These channels are formed from the large cations and disordered 2,2′-dipyridyl ketone (and a small amount of pyrazole in most cases) and house chloride counter ions and water molecules. Partial occupancy of the anion and water sites coupled with unfilled voids point to the channel contents being zeolitic in nature. This is supported by water loss occurring at ambient conditions (TGA measurements) without significant changes to the X-ray powder diffraction pattern, however heating to c.a. 50° C to remove all the water leads to the sample becoming X-ray amorphous. The closest approach of Dy atoms between triangles is 8.88 Å, which will be similar in all the current cases, suggesting that magnetic interaction between lanthanide triangles will be minimal *(Figure 5-3-5)*.

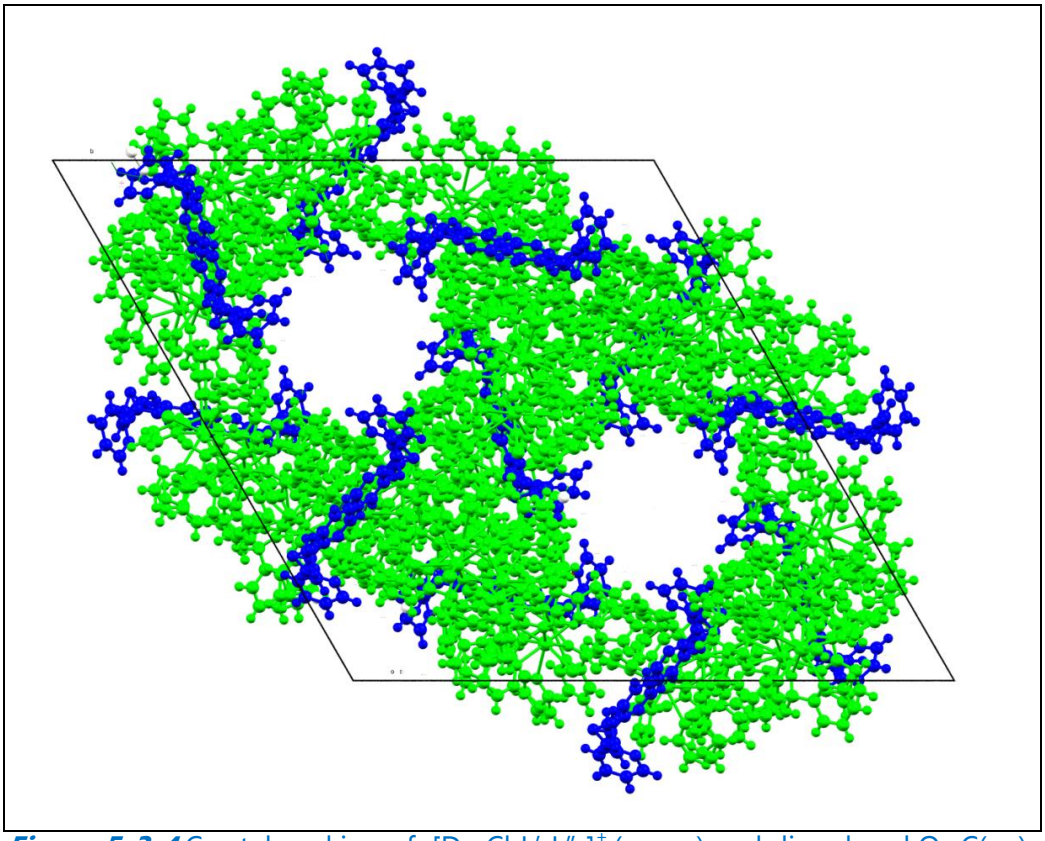

Figure 5-3-4 Crystal packing of $[Dy_3\underline{C}l_3L'_3L''_2]^+$ (green) and disordered $O{=}C(py)_2$ (blue) viewed down 0 0 1, showing the large channels that house Cl^- and H_2O extending through the structure.

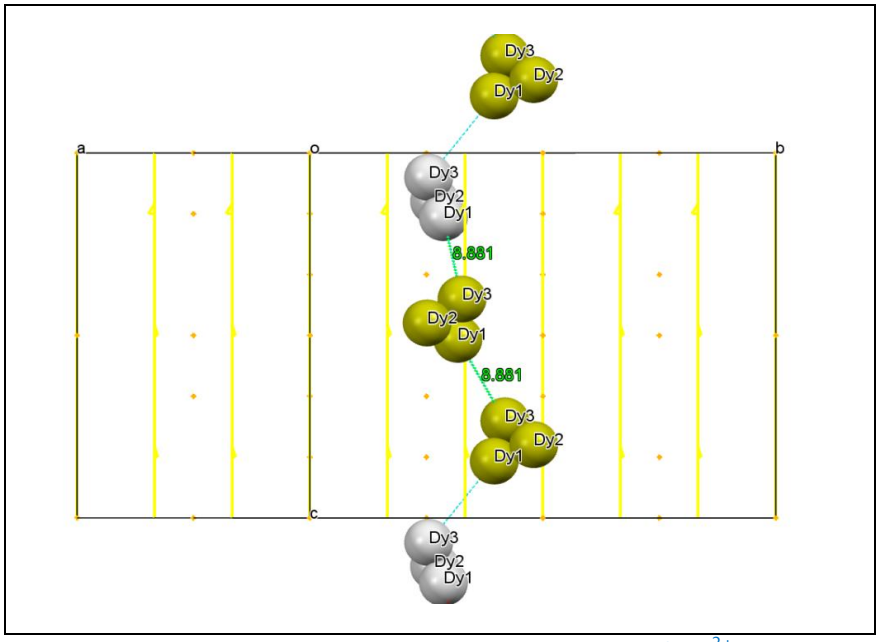

Figure 5-3-5. Closest inter-triangle approach of Dy^{3+} cations

5-4. Experimental

5-4-1. Instruments and Software

X-ray measurements (a). Data for the first six structures was collected on a Bruker Prospector diffractometer employing graphite monochromated Cu Kα radiation. The following software was used.

Abstract goniometer imported SAXI diffractometer images: Saxi-CrysAlisPRO (Agilent Technologies, 2012); Absorption correction: multi-scan *CrysAlis PRO* (Agilent Technologies, 2012); Empirical absorption correction using spherical harmonics, implemented in SCALE3 ABSPACK scaling algorithm; Cell refinement: *CrysAlis PRO* (Agilent Technologies, 2012); Data reduction: *CrysAlis PRO* (Agilent Technologies, 2012)

X-ray measurements (b). Data for the remaining three structures was collected on a Bruker-Nonius Kappa CCD employing graphite monochromated MoKα radiation. Data collection: Collect (Nonius BV, 1997-2000); cell refinement: *HKL SCALEPACK* (Otwinowski & Minor 1997); data reduction: *HKL DENZO* and *SCALEPACK* (Otwinowski & Minor 1997);

5-4-2. Structure Refinement

All the nine structures were subjected to full matrix least squares refinement using SHELXS (Sheldrick, 2008). Most non-hydrogen atoms were subjected to anisotropic refinement – the exceptions being disordered atoms in overlapping pyridine/pyrazole rings, which had to remain isotropic.

Each of the rings in the two capping tetrapodal ligands were refined as a mixture of pyridine and pyrazole. Occupancy constraint were applied to give a total of 2 pyridine and 1 pyrazole rings per ligand.

Hydrogen atoms were constrained to chemically reasonable positions. The lattice partial 2,2′-dipyridyl ketone and pyrazole were subjected to DFIX constraints.

Program(s) used to solve structure: *SIR92* (Giacovazzo *et al.*, 1993); program(s) used to refine structure: *SHELXL97* (Sheldrick, 1997); molecular graphics: *ORTEP-3 for Windows* (Farrugia, 1997); software used to prepare material for publication: *WinGX* publication routines (Farrugia, 1999).

5-5. Magnetic Measurements

AbInitio Calculations with MOLCAS 7.0 based on the above structures showed that the local magnetic axes on Dy centers lie in the plane of the Dy_3 triangle. This leads to a non-magnetic ground state at low temperature. In fact there are two possible ground states in which the magnetic vectors are related by mirrors.

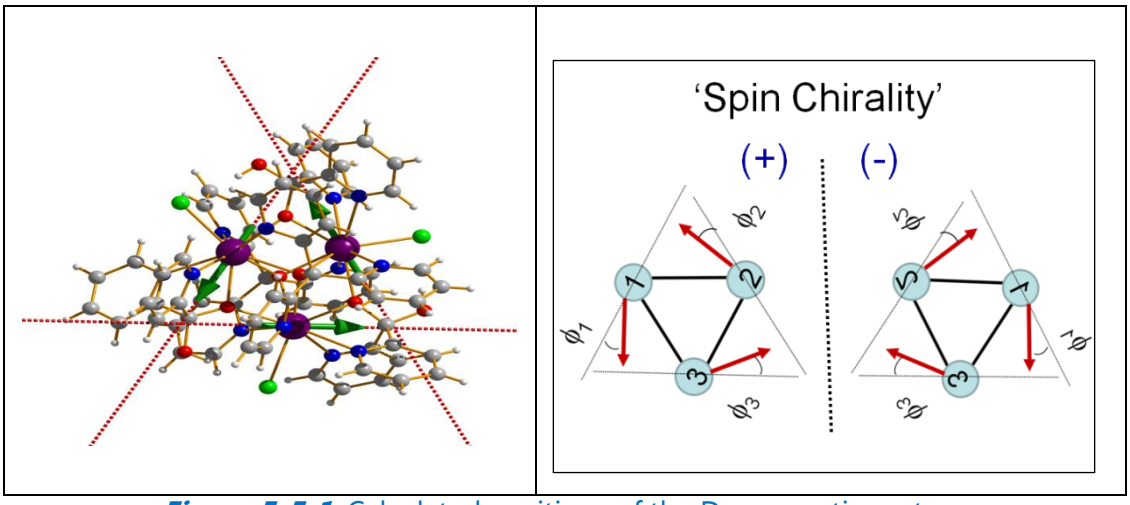

Figure 5-5-1. Calculated positions of the Dy magnetic vectors.

The arrangement of the vectors is very regular and shows considerably less variation than the equivalent values in the previously reported Dy_3 triangular cluster of Powell et al (2006) *(Fig. 5-5-2).* This is in agreement with the linear variation of Ln…Ln distances with Ln^{3+} ionic radii in the current structure *(Fig. 5-3-3)*, which suggests that the structure is relatively inflexible.

KD	Dy(1)	Dy(2)	Dy(3)
	Energies (cm^{-1})		
1	0.0	0.0	0.0
2	98.7	127.8	115.7
3	131.9	178.0	170.1
4	184.7	223.8	219.8
5	202.5	271.2	257.8
6	249.5	288.3	276.9
7	305.7	363.6	338.8
8	400.7	467.1	442.3
	Main values of the *g* tensor		
	0.026	0.009	0.012
1	0.058	0.0230	0.026
	19.582	19.769	19.753
	Angle of anisotropy axis with Dy_3 plane		
	2.4°	0.2°	2.4°
A. Powell triangle	-4.3°	8.8°	-2.4°
Angle of anisotropy axis with tangential direction, ϕ_i			
	3.7°	5.5°	4.0°
A. Powell triangle	-8.9°	9.5°	8.7°

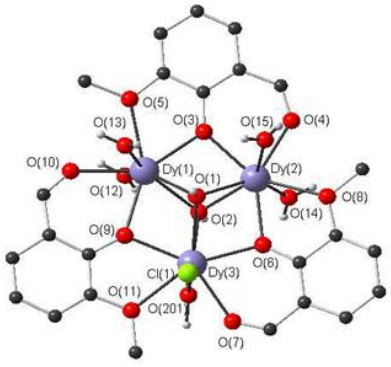

Figure 5-5-2. Calculated magnetic vector directions for the current Dy_3 complex compared to the analogous values for the previously reported Dy_3 triangle (Bottom left, Chibotaru et al., *New. J. Chem.* 2009, *33*, 1157; Powell *et al. Angew. Chem. Int. Ed.* 2006, *45*, 1729.

As predicted from the arrangement of magnetic vectors, complete cancellation is possible and is observed at the lowest temperature (Fig. 5-3-3).

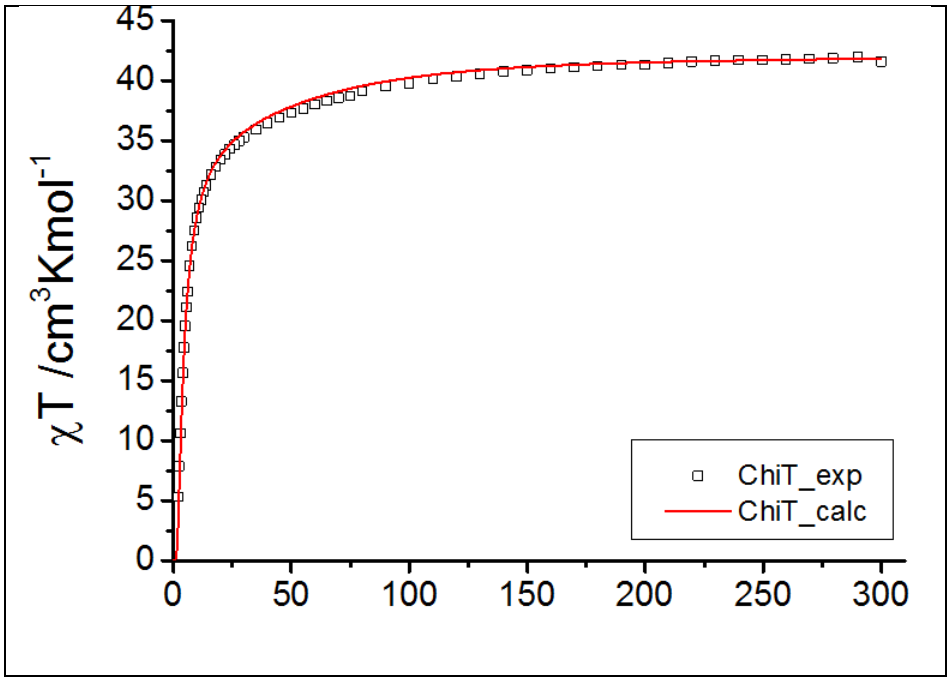

Figure 5-3-3. Calculated and observed molar magnetic susceptibility vs temperature curves for the current Dy_3 cluster, showing good agreement. Decline of magnetic susceptibility to zero with decreasing temperature indicates that complete cancellation of the magnetic moment of the three Dy atoms has occurred.

A particularly interesting feature of lanthanide triangles is observed on application of an external magnetic field parallel to the triangle plane. In the current Dy_3 structure a progressive reorientation of the magnetic vectors occurs until the mirror image of the original magnetic triangle is obtained *(Fig. 5-3-4).* This is observed as change of slope in the magnetisation vs external field plot.

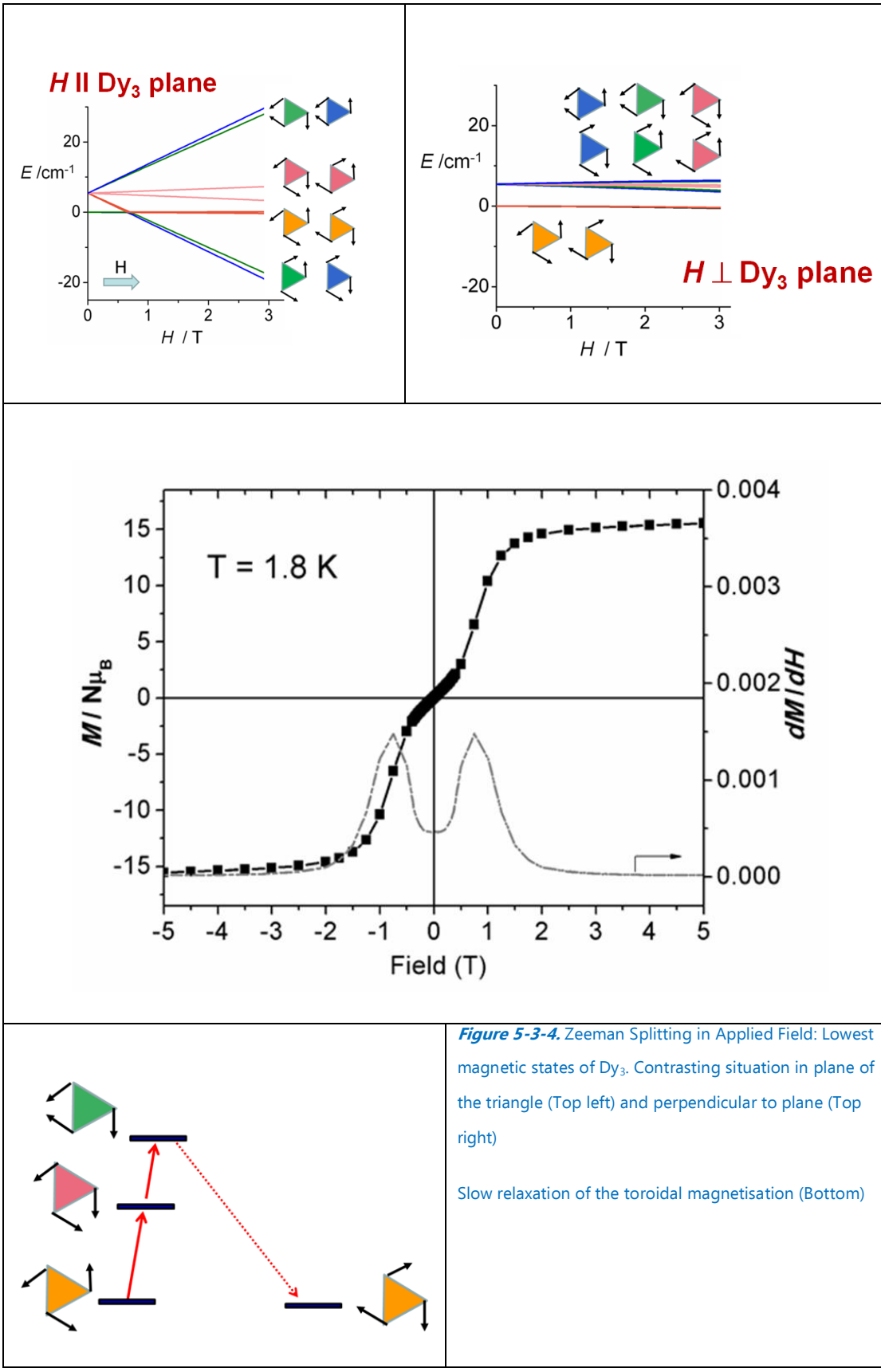

Figure 5-3-4. Zeeman Splitting in Applied Field: Lowest magnetic states of Dy_3. Contrasting situation in plane of the triangle (Top left) and perpendicular to plane (Top right)

Slow relaxation of the toroidal magnetisation (Bottom)

In order to refine the computational parameters, structural and magnetic data from a contrasting lanthanide triangle in which the magnetic vectors do not lie in the Ln_3 plane was required. Computation indicated that in the analogous Er_3 cluster the vectors are directed almost perpendicular to the triangle plane.

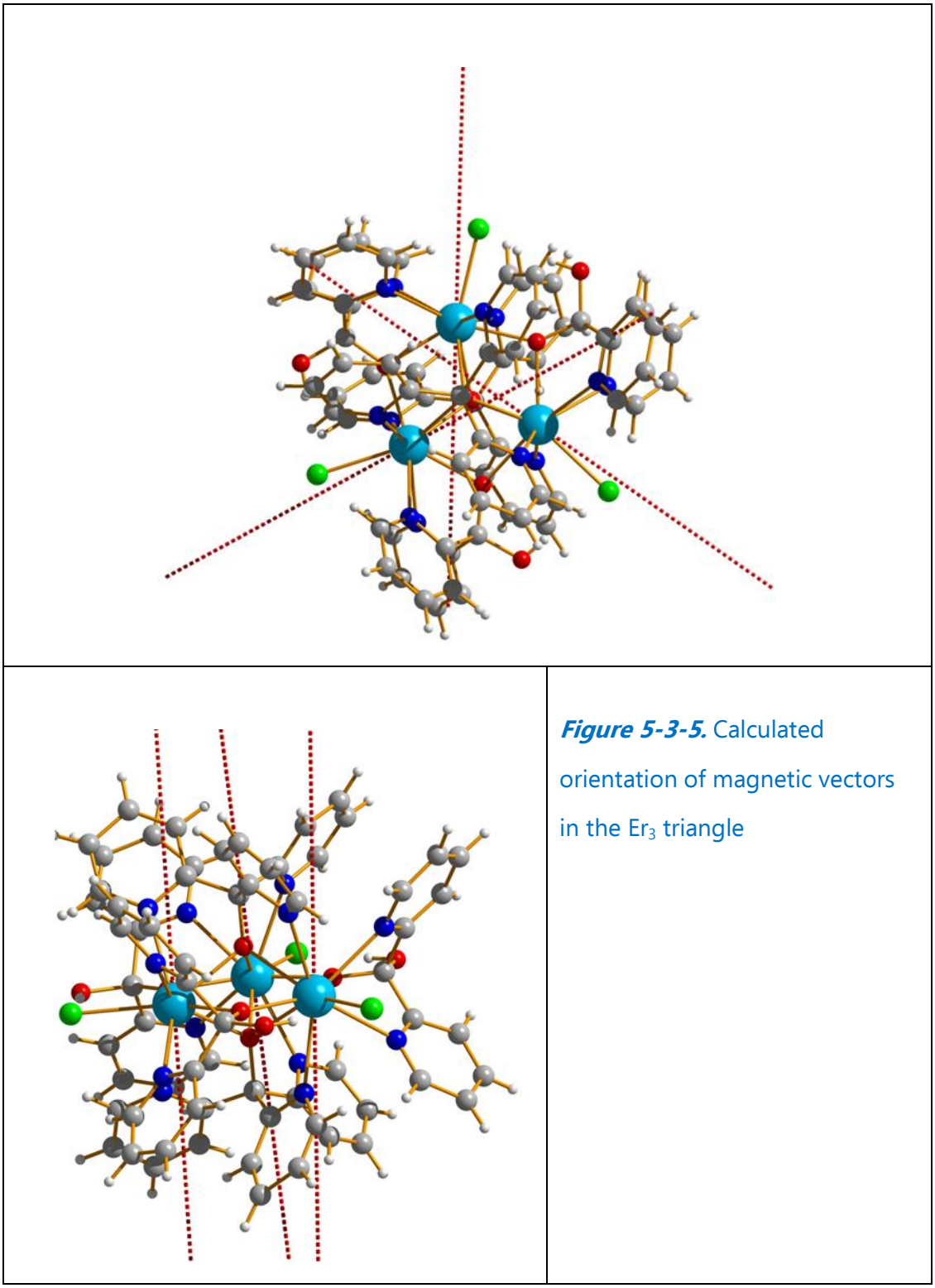

Figure 5-3-5. Calculated orientation of magnetic vectors in the Er_3 triangle

The calculated magnetic susceptibility resulting from the above arrangement of magnetic vectors is show in Fig. 5-3-6 and clearly

shows the effect of spin-frustration as a residual magnetic field at the lowest temperature. The measured susceptibility also shows this effect but further computation is required to produce the final results.

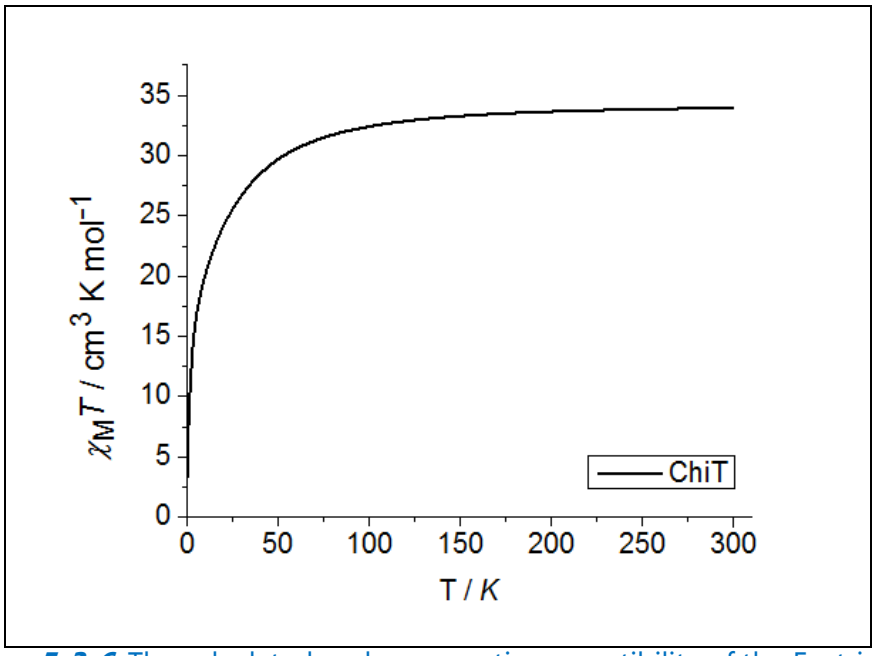

Figure 5-3-6. The calculated molar magnetic susceptibility of the Er_3 triangle

5-6. Conclusion

The complexes form spontaneously when bipyridylketone, pyrazole and a lanthanide trichloride are mixed in molar ratios 5:2:3 in aqueous solutions. Hydrolysis of the bipyridyl ketone occurs uncatalysed but addition of pyrazole to the ketone relies on coordination of the precursor molecules to a metal template (Abraham, 2006). It is possible that, once formed, the triarylazo ligands acts as a template for assembly of the triangular cations, however only dimers were reported when py_3CO^- was reacted

with Eu^{3+} and Tb^{3+} (Watanabe, 2003), implying that triangle formation is a more complex process, reliant on the concerted interplay of both types of ligand with hydrated lanthanide cations. A factor, which may have favoured triangle assembly in the current case is the relative positions of the Cl and OH groups, which facilitate intramolecular hydrogen bonding in the plane of the triangle.

The lanthanide triangles formed in the current case have a regular D_{3h} shape, which vary linearly with Ln^{3+} ionic radii. The uniformity of the structure is reflected in the regular arrangement of calculated magnetic vectors in the Dy_3 triangle, which lie very close to the triangle plane. This contrasts to the magnetic behaviour of the analogous Er_3 structure, which retains a residual magnetic susceptibility at the lowest temperatures due to spin-frustration.

5-7. References

Abrahams, B. F., Hudson, T. A. & Robson, R. (2006). *Chem. Eur. J.* **12**, 7095–7102.

Agilent Technologies, *CrysAlis PRO*, Version 1.171.36.20 (release 27-06-2012 CrysAlis171 .NET) (compiled Jul 11 2012,15:38:31)

Altomare, A., Cascarano, G., Giacovazzo, C., Guagliardi, A., Burla, M. C., Polidori, G. and Camalli, M. (1994). *J. Appl. Cryst.* **27**, 435.

Blessing, R. H. (1995). *Acta Cryst.* **A51**, 33–38.

Farrugia, L. J. (1997). *J. Appl. Cryst.* **30**, 565.

Farrugia, L. J. (1999). *J. Appl. Cryst.* **32**, 837–838.

Greenwood, N. and Earnshaw, A., (1974), Chemistry of the Elements, 2nd Ed., Butterworth-Heinemann, p 1233.

Kaltsoyannis, N. and Scott, P., (1999), The f elements, Oxford Chemistry Primers, Oxford University Press.

Lin, S-Y., Wernsdorfer, W., Ungur, L., Powell, A.K., Guo, Y-N., Tang, J., Zhao, L., Chibotaru, L.F. and Zhang, H-J., (2012), *Angew. Chem. Int. Ed.*, **51**, 12767 –12771.

Nonius (1998). COLLECT. Nonius BV, Delft, The Netherlands.

Otwinowski, Z. & Minor, W. (1997). Methods in Enzymology, Vol. 276, Macromolecular Crystallography, Part A, edited by C. W.Carter Jr & R.M.Sweet, 307–326. New York: Academic Press.

Orchard, A.F., (2003), Magnetochemistry, Oxford Chemistry Primers, Oxford University Press.

Sheldrick, G. M. (2008). *Acta Cryst*. **A64**, 112–122.

Tang,J., Hewitt, I., Madhu, N.T.,Chastanet, G., Wernsdorfer, W., Anson, C.E., Benelli, C., Sessoli, R. and Powell, A.K., (2006) *Angew. Chem. Int. Ed.*, **45**, 1729 –1733

Watanabe, M.,T.Nankawa, T.Yamada, T.Kimura, K.Namiki, M.Murata, H.Nishihara, S., (2003), *Tachimori Inorg.Chem.*, **42**, 6977